ABSTRACT

Title of Dissertation: STUDIES OF NEAR-FIELD NONLINEAR OPTICAL IMAGING OF THIN FILMS AND TRANSIENT PHOTOCONDUCTIVITY IN CONJUGATED POLYMERS

Hongye Liang, Doctor of Philosophy, 2005

Directed By: Professor Chi Hsiang Lee
Professor Christopher Davis
Department of Electrical and Computer Engineering

The dissertation is composed of two parts: 1) near-field nonlinear optical studies of ferroelectric and polymeric thin films and 2) transient phenomena in polymers.

Ferroelectric thin films are imaged with both topology and surface optical second harmonic (SH) distribution. The lateral resolution is determined to be 80nm. The relation between local optical second harmonic intensity and polarization of the ferroelectric domains is explored both experimentally and theoretically. A polydomain ferroelectric film with grid domain structures is used as a standard sample to check the validity of this relationship. Second order nonlinear properties of nonlinear optical (NLO) polymers are studied both in the far-field and near-field.

Transient photoconductivity in conjugated polymers is studied systematically. Picosecond electric pulses generated in a photoconductive switch fabricated on polymer

are used to derive the photoconductance of the device. The pulse width of electric pulse is measured by photoconductive sampling to be around 1-2ps, which is the best result in polymers up to now. Transient photoconductivity and mobility are calculated, the transient mobility in MEH-HPPV (poly[2-methoxy-5-(28-ethylhexyloxy)-1,4-phenylenevinylene]) is estimated to be ~800 cm^2/Vs. A new method of photoconductive sampling is proposed using only one photoconductive switch, and transient reflectivity change of the polymer is also observed.

Optical rectification in poled nonlinear optical (NLO) polymers has been used to generate and detect THz radiation. Relation between THz radiation power and incident laser spot size are studied for the first time in polymer materials; an optimized pump laser spot size of close to THz wavelength is obtained. Application of THz to study organic samples is presented.

STUDIES OF NEAR-FIELD NONLINEAR OPTICAL IMAGING OF THIN FILMS AND TRANSIENT PHOTOCONDUCTIVITY IN CONJUGATED POLYMERS

By

Hongye Liang

Dissertation submitted to the Faculty of the Graduate School of the
University of Maryland, College Park, in partial fulfillment
of the requirements for the degree of
Doctor of Philosophy
2005

Advisory Committee:
Professor Chi H. Lee, Chair/Advisor
Professor James R. Anderson
Professor Christopher C. Davis, co-Advisor
Professor Romel Gomez
Dr. Warren N. Herman

Dedication

To my family

Acknowledgements

I would like to express my sincere gratitude and appreciation to my advisor, Prof. Chi H. Lee, for giving me the opportunity to work in his group, for his expert guidance and mentorship, for his encouragement and support at all levels, and for his invaluable comments during the whole work with this dissertation. I would like to thank my advisor Prof. Christopher C. Davis for his guidance and support in the NSOM projects and for his warm encouragements.

I would like to thank Dr. Herman at LPS for providing me the opportunity to work on the polymer projects and for his advice and suggestions in many aspects of my thesis work. I would like to thank Dr. Weilou Cao for training me and helping me in my research. I would like to thank Dr. Igor Smolyaninov for training me on NSOM and the many helpful discussions and directions. I would like to thank Ms. Min Du and Dr. Junghwan Kim for teaching me and helping me on the clean room techniques.

I would like to thank my colleagues in both Prof. Lee and Prof. Davis' groups, including Dr. Jinjin Li, Dr. Rafael Rojas, Dr. Sukanya Tachatraiphop, Dr. Vildana Hodzic, Dr. Andre Schwartz, Dr. Linda Wasiczko, Yi-Hsing Peng, Alen Lo, Younggu Kim, Glenn Hutchinson, Dong Park.

I would like to thank Dr. Tong Zhao and Prof. Ramesh in the Material Research Science and Engineering Center who provided me with PZT films.

Finally, I would like to express my thanks to my parents and my wife, for their encouragement and support during my Ph.D studies, and to Kevin, who made every day of my life enjoyable.

Table of Contents

List of Tables

List of Figures

Chapter 1: General Introduction

Near-field optical microscopy (NSOM) is a significant extension to the capability of conventional lens-based microscopes [1] [2]. It works by raster scanning a tapered fiber probe close to a sample surface. Features on the nanometer scale can be resolved independent of the wavelength used. The main requirement for high resolution performance of NSOM is a tiny probe (generally on the order of 50nm) and an extremely small distance (much smaller than a wavelength, generally <10nm) between probe and sample. The close scanning of a small probe can convert high spatial frequency evanescent fields that are normally lost in conventional microscopy to propagating modes in the fiber. NSOM can be classified as scanning probe microscopy (SPM), similar to atomic force microscopy (AFM) [3] and scanning tunneling microscopy (STM) [4]. However, since NSOM detects both topography and optical information of the sample surface so more contrast mechanisms exist: intensity, polarization, color (frequency), etc.

In recent years, ferroelectric materials and thin films have attracted much attention and exhibited potential in many important applications such as dynamic random access memories (DRAMS) [5], non-volatile ferroelectric random access memories [6] [7] and infrared sensors [8]. At present, the ferroelectric materials suitable for these devices include the $Pb(Zr,Ti)O_3$ (PZT) systems, $SrBi_2Ta_2O_9$ (SBT) systems, $Bi_4Ti_3O_{12}$ (BIT) systems and $BaTiO_3$ (BT) systems, which have been studied with a great deal of interest [9]. Among these ferroelectric materials, the most widely studied and used is PZT, which has an extremely low coercive field, a high remanent polarization, better mechanical strength and small deviation in composition. PZT thin films are composed of

domains. The understanding and control of ferroelectric domains are essential for all currently pursued applications and may well be the key for future applications.

Force microscopy is a powerful tool to characterize ferroelectric domains in thin films, with a lateral resolution down to nanometers [10]. Optical second harmonic imaging can reveal the spontaneous dielectric polarization of the ferroelectric domains in the films of interests [11] and has the potential of doing time-resolved measurements. Near-field SH microscopy is a combination of these two techniques.

Optical second harmonic generation is a second order nonlinear process which is forbidden in centrosymmetric materials [12]. It is extremely sensitive to asymmetries such as surfaces, interfaces, and polar structures [13]. SHG has been used for nondestructive observation of periodically poled ferroelectric domains [14] [15] and domain structures in epitaxially grown magnetic garnet films [16]. But most of the imaging work has been implemented in the far field, i.e., the observations are based on a conventional microscopes with CCD (Charge-Couple Device) cameras illuminated by second harmonic waves that are generated in the sample. These techniques have a diffraction limited spatial resolution of the order of the wavelength and can hardly be used for detailed visualization of the transition regions between neighboring domains, i.e., domain walls, and the tens of nanometer sized domains structures in thin films. Recently, linear scanning near-field optical microscopy has been used to observe with sub-wavelength resolution domain walls in ferroelectric $LiTaO_3$ crystals via strain induced birefringence [17], and near-field SH imaging is reported on $LiNbO_3$ domain walls [18]. SH imaging presented in [18] claims a resolution of $150nm$ on a piece of $200\mu m$ thick $LiNbO_3$ crystal, where the SH originates from the bulk. Currently more

interests are in the research on ferroelectric thin films. High resolution optical SH images of ferroelectric thin films are not as easy to obtain due to the weak surface SHG effects. In this dissertation, we employed the near-field scanning microscopy to image the SHG from ferroelectric thin films (200nm-500nm) to reveal the local domain polarizations. NSOM enables us to obtain both the morphology and local optical information simultaneously. Near-field SH mapping of the PZT films has been achieved with a lateral resolution of 80nm and the relation between the SH intensity and the polarization of domain has been described both theoretically and experimentally.

Nonlinear optical (NLO) polymers are important optical nonlinear material nowadays due to the potential applications in electro-optic and photonic devices [19]. Chromophores are the origin of nonlinearity in most NLO polymers. Because the nonlinear susceptibility increases with increasing polar order, imaging techniques can be useful for evaluating the spatial morphology of chromophore order. Near-field characterization of NLO polymers can provide useful information with a high spatial resolution. Only few papers have appeared on this topic, mainly on other organic material like organic crystals [20] [45]. More recently near-field studies on grating structures fabricated on poled NLO polymers was reported [21]. We observed continuous NLO polymer thin films using NSOM in both reflection and transmission modes. Both surface morphology and SH mapping of the polymer are presented. The resulting $\chi^{(2)}$ distribution on the film surface differs significantly from the topographical images. The extremely small SH photon counts (~10/second) made the imaging process very slow.

Conjugated polymers can be doped to change their conductivity to go from insulator to conductor [22]. They attract interest in a wide variety of optical, electronic,

optoelectronic, and sensor applications, including light emitting diodes, thin film transistors, photovoltaic cells, and plastic lasers, etc [23]. Carrier photo-generation in conjugated polymers has attracted researchers' attention for a long time with the aim to have a better understanding of physical mechanisms that may lead to many important applications. Considerable efforts have been devoted to unravel the generic aspects of transient photoconductivity in conducting polymers [24][25][26]. Carrier photogeneration and carrier mobility are among the topics of great interest. Steady state characterization of photo carrier properties has been reported by many groups [27][28]. For transient measurements, Heeger's group at UCSB has described important work on the photoconductivity of conjugated polymers [26][29]. But their work was based on sub-nanosecond measurement systems, hence not enough time resolution was provided for a study of ultrafast processes in polymers. In this thesis work we used different schemes of photoconductive sampling on PPV polymers and obtained time resolutions of 1ps, which is the fastest measurement on polymer photoconductivity to date. We also implemented a one-gap photoconductive sampling system, as an alternative to the conventional two-switch systems, leading to a better time resolution.

This dissertation is composed of two parts: 1. Studies of ferroelectric and NLO polymeric materials using near-field nonlinear optical microscopy; 2. Studies of ultrafast processes in organic polymers.

Chapter 2 is a brief overview of near field optics concepts and NSOM instrumentation.

Chapter 3 summarizes the near-field second harmonic imaging of ferroelectric thin films. Second harmonic (SH) mapping of ferroelectric films was obtained with a

resolution of 80nm. A single crystal $BaTiO_3$ was used to define the relation between the polarization and SHG intensity, which gave a reasonable explanation of the contrast and gray scale in the SH mapping image, leading to a connection between near-field SH mapping with domain structures in the ferroelectric films. At the same time, local field enhancement under the bare tapered fiber tip was analyzed with a simple electromagnetic model. According to our analysis, a factor of 20 can be expected for the field enhancement under the tip, which allowed us to have high resolution image with an apertureless fiber probe. As proof of the SHG and polarization relationships, we have investigated the dependence of the SHG intensity on polarization of light for the near- and far-field cases respectively, and at different locations on the ferroelectric film. Good agreement with theory was achieved. To sum up, in this chapter, local field enhancement by uncoated tapered fiber tip in SHG was introduced; high resolution SH mapping of ferroelectric film was implemented with 1/10 of illumination wavelength; relationship between ferroelectric polarization directions and SH intensity was established both experimentally and theoretically, demonstrating the ability of SH microscopy to reveal the domain structures in ferroelectric materials.

Chapter 4 presents near-field SH measurement on two types of NLO polymers: SPECH/PAA and C2CMA. Both transmission and reflection mode NSOM were used to study the near-field nonlinear optical properties of the polymers. Because of the extremely weak signal when collecting by a nano-size probe, a systematic study on the SHG was carried out to find optimum working conditions. Scanning by NSOM gave both topography and SH distribution on the polymer films. The results showed that $\chi^{(2)}$ distribution was quite different from the surface topology.

Chapter 5 deals with the photoexcitation in conjugated polymers. Photoconductivity in semiconducting polymers was observed a long time ago, while measurement of the photoconductivity was only on a nanosecond time scale in the past. We used frequency doubled light from a femtosecond Ti:sapphire laser to do photoconductive sampling on a specifically designed polymer device. A 2ps pulsewidth was measured by autocorrelation of electrical pulses from two separate polymer photoconductive switches. A transient photocarrier mobility of ~500cm^2/V was estimated. The use of femtosecond laser systems and carefully designed high speed devices is key elements in achieving high time resolution. But the electric signal from polymer switches is usually much smaller than from semiconductors. A systematic study of the factors affecting the measurements has greatly increased the S/N, allowing us to observe small electric pulses. Going one step further, we used a single gap to do the job of the two switches for photoconductive sampling. Due to the reduced capacitance, improved results with sub-picosecond resolution were obtained. This is the fastest electric pulse generated and measured on semiconducting polymer up to now, providing proof of high transient mobility in semiconducting polymers.

In Chapter 6 we used poled polymers to generate THz radiation by optical rectification, or differential frequency generation. THz performance was compared with a commercial $Zn_{0.95}Cd_{0.05}Te$ to roughly estimate the electro-optic (EO) coefficient of the polymer material. And finally THz power dependence on excitation laser spot size was implemented. Similar study was done on semiconductor emitter [30]. This is the first such study in polymer film. At a fixed incident laser power, the THz radiation power increases with the decreasing of laser spot on the polymer due to the increased laser

power density. But when the laser spot was smaller than the THz wavelength, reduction in the spot size leads to decreasing of THz power, owing to the diffraction effect. An optimized pump laser spot size exists. This provides us with guidance to extract higher THz radiation power with a finite pump power.

Chapter 2: Near-field Scanning Optical Microscopy

Conventional optical microscopy is one of the most straightforward, versatile techniques employed to produce magnified images of specimens, giving researchers the ability to see objects that are normally invisible. However, the use of lenses in image formation leads to diffraction and places a limit on the resolution on this type of microscopes (Abbé diffraction limit) [31]. The theoretical resolution is determined by the wavelength of the light used to generate the images. For general white light illumination, a resolution of $\lambda/2 = 250nm$ can be obtained in an optimum case. For a better resolved image, other forms of microscopy are employed. The most direct techniques use shorter wavelengths, such as x-rays or electron beams. As early as 1928, the idea of enhancing the image resolution by illuminating the sample through a minute hole at the apex of an otherwise opaque coated cone was proposed by Synge [32]. Due to some practical reasons, it was not until 1972 that the first near-field experiment was published by Ash and Nicholls [33]. They used 3cm radiations and obtained $\lambda/60$ resolution on a metal grating.

The first paper on the optical near-field scanning microscope was published in 1984 by Pohl et al. at IBM Zurich [34]. They used a metal coated quartz tip which was pressed against a surface to create an aperture. Betzig *et al*. at Cornell University improved the microscope by introducing a micropipette as the probe [35, 36]. In 1991, Betzig *et al*. at AT&T Bell Laboratories introduced the use of single-mode optical fibers as near-field optical probes [37], which at present is the most popular probe. One end of

the fiber is tapered to a tip size of approximately 50 nm and subsequently coated with aluminum to create a sub-wavelength aperture at the end.

2.1. Concepts of Near-field Optics

When a light wave of wavelength λ is incident on an object with features smaller than $\lambda/2$, it is practically converted into propagating and non-propagating field components [38]. The propagating fields can be detected by a lens-based microscope system. The non-propagating components are non-homogeneous waves closely related to the materials and spatial structure of the object surface [39].They can't exist in free space independent of matter and decay exponentially away from the sample surface. These non-propagating components are called evanescent waves and are confined to a region close to the sample surface, defined as the near-field region [40]. The following discussions present a simple analysis of the near-field imaging process.

Consider the geometry in Fig. 2.1. An object of limited size, with a transmittance of $f(x,y,0)$ at z=0. The scalar field $f(x,y,0)$ can be Fourier decomposed in the spatial frequency domain as:

$$F(u,v) = \iint_{\infty} f(x,y,0) e^{-j2\pi(ux+vy)} dxdy \qquad (2.1)$$

Fourier theory states that any signal, in our case spatial images, can be expressed as a sum of a series of sinusoids. In the case of imagery, these are sinusoidal variations in brightness across the image. These sinusoidal Fourier components are usually called spatial frequencies. They are used widely in imaging characterization. The spatial frequency components can be recombined as:

$$f(x,y,0)=\iint_{\infty} F(u,v)e^{j2\pi(ux+vy)}dudv \tag{2.2}$$

A plane wave *P* of amplitude *A* at a point r is represented mathematically as:

$$P(x,y,z)=Ae^{j(\vec{k}\cdot\vec{r})}=Ae^{j(k_x x+k_y y+k_z z)}=Ae^{j\frac{2\pi}{\lambda}(\cos\alpha x+\cos\beta y+\cos\gamma z)} \tag{2.3}$$

where $\vec{k}$ is the wave vector with magnitude $k=2\pi/\lambda$, λ is wavelength, and $\cos\alpha$, $\cos\beta$, $\cos\gamma$ are the direction cosines with *x, y*, and *z* axes respectively, as illustrated in Fig. 2.1. and $\cos\gamma=\sqrt{1-\cos^2\alpha-\cos^2\beta}$.

From Eq. (2.2) it can be seen that the original field at z=0 can be represented as a series of plane waves with amplitude *F(u,v)* and direction $\cos\alpha=\lambda u/2\pi$, $\cos\beta=\lambda v/2\pi$. Then Eq (2.1) can be written equivalently as:

$$F(\frac{2\pi\cos\alpha}{\lambda},\frac{2\pi\cos\beta}{\lambda})=\iint_{\infty} f(x,y,0)e^{-j2\pi(\frac{2\pi\cos\alpha}{\lambda}x+\frac{2\pi\cos\beta}{\lambda}y)}dxdy \tag{2.4}$$

The field at the object can thus be regarded as a superposition of plane waves propagating in the direction $\vec{k}=(k_x,k_y,k_z)=(\cos\alpha,\cos\beta,\cos\gamma)2\pi/\lambda$, with the direction cosines,

$$\cos\alpha=\lambda u,\qquad \cos\beta=\lambda v,\qquad \textit{and}\qquad \cos\gamma=\sqrt{1-\cos^2\alpha-\cos^2\beta} \tag{2.5}$$

Choosing the observation plane at distance *z=f1+f2*, the angular frequency spectrum can be written as,

$$F(\cos\alpha\cdot k/2\pi,\cos\beta\cdot k/2\pi,z)=F(\cos\alpha\cdot k/2\pi,\cos\beta\cdot k/2\pi)e^{j\frac{2\pi}{\lambda}z\sqrt{1-\cos^2\alpha-\cos^2\beta}} \tag{2.6}$$

This equation reveals that only a limited range of angular frequencies propagates in the z-direction. If the Fourier components of the initial field are:

$\cos^2\alpha + \cos^2\beta < 1$: the argument of the exponential function in eq. (2.6) is imaginary, then each spectral component of the initial field falling in this spectral range can be considered to propagate a distance z with an angle dependent phase shift.

$\cos^2\alpha + \cos^2\beta > 1$: Eq. (2.6) can be rewritten as

$$F(\cos\alpha \cdot k/2\pi, \cos\beta \cdot k/2\pi, z) = F(\cos\alpha \cdot k/2\pi, \cos\beta \cdot k/2\pi) e^{-kz\sqrt{\cos^2\alpha + \cos^2\beta - 1}} \quad (2.7)$$

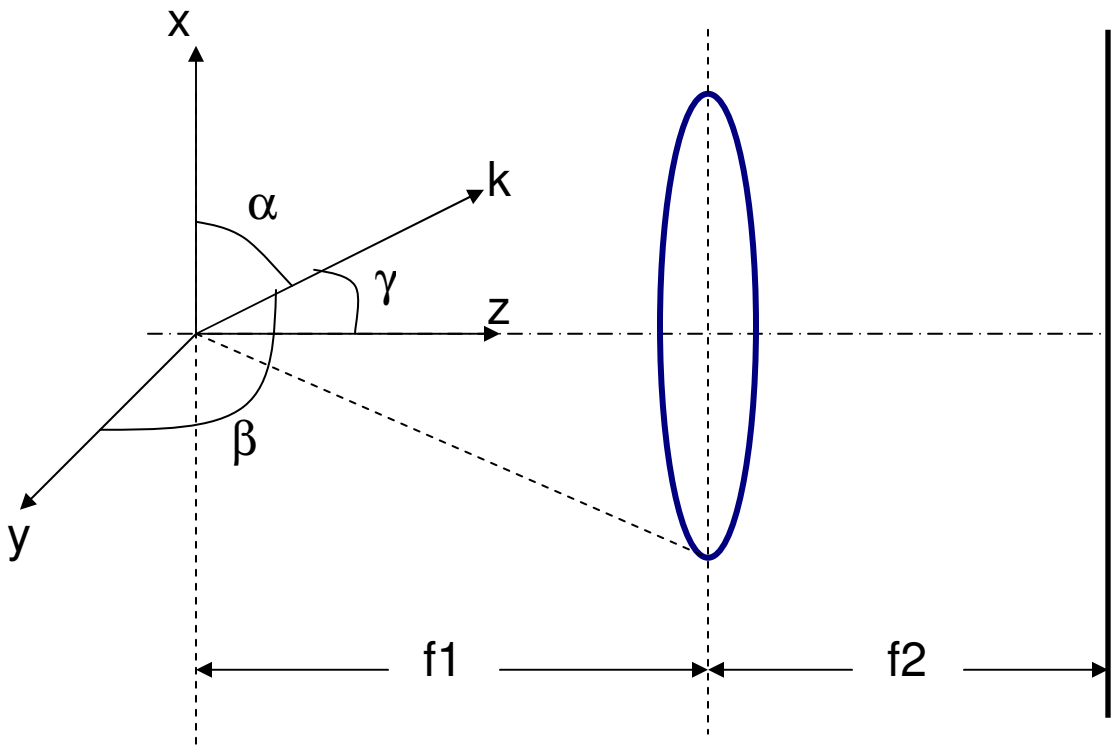

Figure 2.1: Optical image formation geometry

where the argument of the exponential function is real. As a consequence the amplitude of the wave decreases exponentially in the z-direction. Hence, these are called evanescent waves.

Since $\cos\alpha$ and $\cos\beta$ are proportional to the spatial frequencies *u* and *v*, it is seen that for low spatial frequencies and thus for low angular frequencies the waves propagate in the z-direction towards the observation plane. These components are the *far-field* components of the angular frequency spectrum. The high spatial frequency components are only present near the sample and decay exponentially in the z-direction. The region near the sample containing the high spatial frequency components is called the *near-field* zone.

Far-field: In conventional optical microscopy, lenses with a limited numerical aperture ($NA = sin(\theta)$), are placed in the far-field. Consequently, only waves with their k-vector within *NA* will reach the detector,

$$sin(z, k) < NA \tag{2.8}$$

$$\cos^2\alpha + \cos^2\beta < NA^2 \tag{2.9}$$

From Eq. (2.5), it can be seen that only spatial frequencies (*u*, *v*) which are smaller than NA/λ are detected, corresponding to lateral distances in $f(x, y, 0)$ larger than λ/NA. As a result, the maximum achievable resolution at the image plane is limited to λ/NA; the *diffraction limit* by Abbe [31].

Similarly, Rayleigh defined the diffraction limit as the distance between two objects for which the intensity maximum of the airy disc of one object falls on the first minimum in intensity airy disc of the second object. This resolution limit can be determined by looking at optical image formation as $0.61\cdot \lambda/NA$, which is the Rayleigh criterion.

Near-field Eq. (2.7) revealed that waves containing the high spatial frequency information of the object do not propagate but decay exponentially with the distance from

the object. Near-field scanning optical microscopy is able to detect these non-propagating evanescent waves in the near-field zone, in order to obtain the high spatial frequency information of the object. For this purpose a probe has to be brought into the near-field zone, close to the sample to either detect the near-field directly, by means of a nanometer-size detector, or to convert the evanescent waves into propagating waves and detect these in the far-field. As these methods detect the already present near-field this mode of operation is called the collection mode. Another method is to use the illumination mode in which high spatial frequency waves are introduced near the sample, by a sub-wavelength light source, and propagating waves, resulting from an interaction between the near-field and the sample, are detected in the far-field. The next section will discuss briefly the NSOM working principles and configurations.

2.2 NSOM configurations

Overview: Near-field scanning optical microscopes, referred to as NSOM (or SNOM in some publications), is a scanning probe microscope similar to STM or AFM, with an additional ability to collect optical information about the object [1-4].

The NSOM in our experiments uses an optical distance control scheme. The fiber tip is glued onto a piezo tube and dithers at resonance. The tip was brought to the proximity of the sample by a picomotor. When the fiber tip approaches the sample surface, the amplitude of vibration damps. By monitoring the amplitude change and using a feedback control circuit, the tip-sample distance can be controlled. The piezotube also works as an actuator to raster scan the tip across sample surface at a fixed, predetermined distance. At each point the local light intensity is collected to form a 2D image. Usually

a tapered fiber tip is used in NSOM as optical probe, which is the heart of an NSOM instrument. The microscope structure is given in Fig. 2.2:

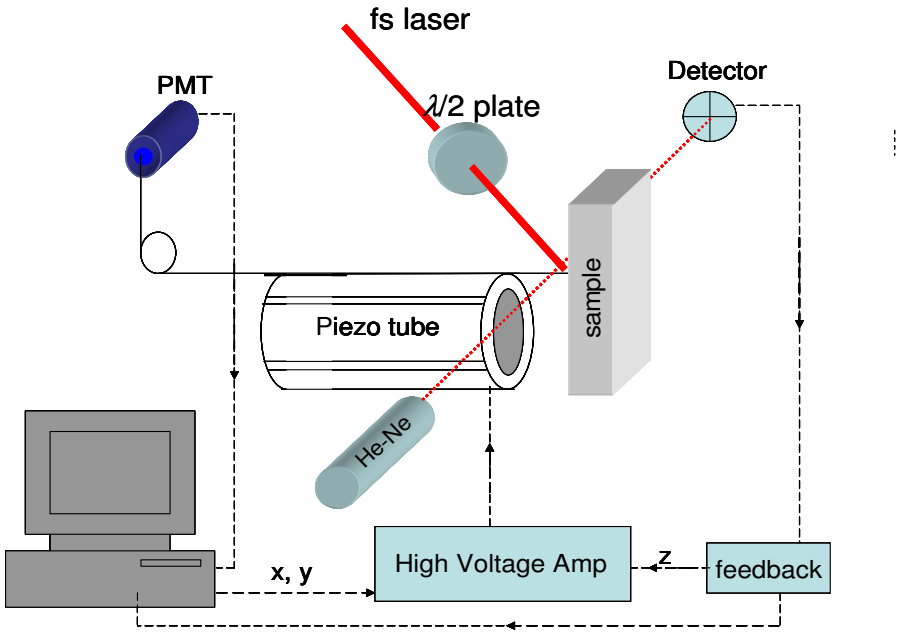

Figure 2.2 Schematic diagram of near-field scanning optical microscope

Distance control: Shear force detection is the most widely used method to regulate the tip-sample distance in NSOM. The technique was first implemented by Betzig et al [41] and Toledo-Crow et al [42]. In this method the tapered fiber tip is laterally vibrating via a piezo tube or tuning fork at its resonance frequency. For a resonance with sufficiently high Q, a very small shear force (nanonewtons) causes a reduction in the tip vibration amplitude. The amplitude of the vibration is optically monitored by illuminating the tip with an external laser focused on the fiber tip. By measuring the AC part of the light leaving the tip, the shear force change can be sensed, corresponding to the distance to the sample surface. Non-optical shear force sensing can be implemented by a quartz tuning fork, in which the tuning fork serves both as an actuator vibrating the tip and as the

sensor for the change of resonance frequency due to interaction with the sample surface [43].

Tapered fiber tips: The tapered fiber tip is used as the optical probe in NSOM. In most cases the fiber tip are coated, with a small opening at the apex to allow light pass through. This aperture can be as small as several tens of nanometers, which is the key to breaking the diffraction limit. When the tip is brought in close proximity to the sample, we can locally image the object's surface at dimensions on the order of the aperture size.

Our tapered fiber tips are fabricated using a micropipette puller (Sutter P-87) combined with a focused 50W CO2 laser (Synrad). By adjusting laser power, focal point size, and pulling force and velocity, the taper shape can be controlled. Another technique of making fiber tips is by chemical etching. Chemical etching produces smaller tips with sharper cone angles. The tip is like an appendix to the fiber with no tapered part, so leakage may occur at the transition point.

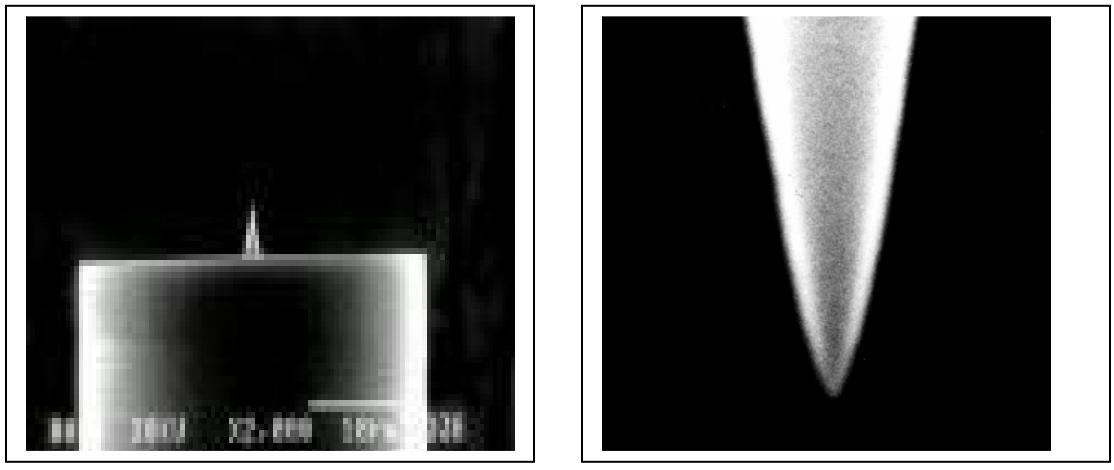

(a) (b)

Figure 2.3 Electron microscopy images of fiber tips (a) chemically etched and (b) mechanically pulled tip.

Scanning piezotube: Almost all scanning probe microscopes (SPM) utilized piezoelectric ceramics as the scanning mechanism. In a piezoelectric material an induced stress causes an internal electric field in the material. This effect is reversible, i.e., an applied electrical field will cause stress in the ceramic. The stress manifests itself in a deformation of the material.

Piezoelectric translators can take several geometries, including tube scanners, bimorphs, and stacks. Most NSOMs use a tube scanner, which is illustrated in Fig.2.4.

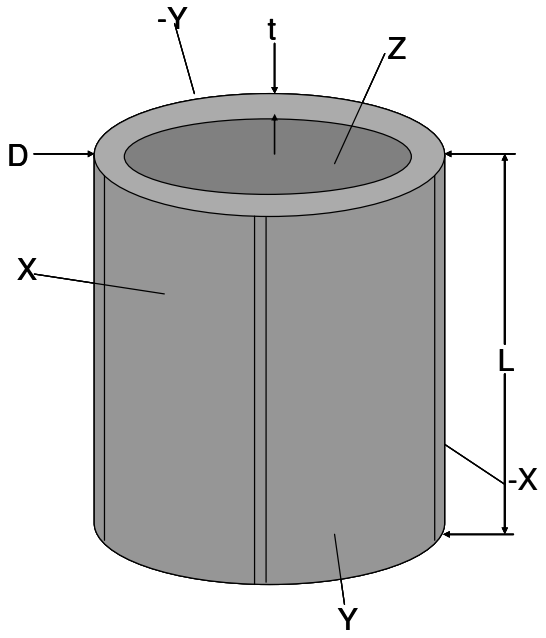

Figure 2.4 Schematic diagram of tube scanners used for actuators for scanning probe microscopes.

These tubes are in cylindrical form, with inside and outside walls coated with metallic electrodes. Voltage can be applied to the piezoelectric crystal through the electrodes. The outer electrode is sliced into four quadrants at 90 degrees, as shown in

Fig. 2.4. When applying –V to –X and +V to X, the tube will tilt along the X axis. The polarization tensor of the material will determine the direction of the translation for a given electric field polarity. Similar translation can be accomplished in the y direction. Applying the voltage in pairs can reduce the crosstalk between x and y directions.

The amount of deflection of the tube can be estimated. Consider a tube with length L, outside diameter D and wall thickness t as in graph. The lateral deflection of the scanner is given by [14]

$$\Delta x = \frac{2\sqrt{2}d_{31}VL^2}{\pi Dt} \tag{2.10}$$

where d_{31} is the piezoelectric coefficient of the material in the direction of translation and V is the applied voltage. Similar behavior exists for y direction. A typical value of d_{31}=-1.73nm/V for PZT, resulting in a 15μm range for 200V bias voltage.

The z translation is given by

$$\Delta z = \frac{2d_{31}VL}{t} \tag{2.11}$$

With a 200V bias, 1.7um range can be achieved. These numbers are only an estimate. In practice, calibration must be performed on a sample with well-defined features and known dimensions.

The NSOM instrumentation also requires a feedback control circuit which will keep the tip to sample distance fixed. The most commonly used is a PID controller. At the same time, high voltage power supply is required to make the tube scan. The detailed description can be found in [1].

Based on the same principle of collecting an optical signal in proximity to a sample, NSOM can take many forms. In this dissertation, we used a reflection mode

NSOM, which is illuminated by an external laser while collecting light using the near-field fiber probe. The shear force detection is via optical amplitude monitoring.

Chapter 3: Nonlinear Optical Imaging of Ferroelectric Thin Films Using NSOM

This chapter discusses the application of NSOM to the study of ferroelectric thin films, specifically, PZT and BST (Barium Strontium Titanate) thin films. Starting with a general introduction to ferroelectric materials and SHG microscopy, the results on PZT domain imaging and identification are presented and analyzed.

3.1 Introduction to Ferroelectric Materials

Ferroelectric materials have been commercially important in the electronics industry for more than 50 years, and in ceramic form have found applications ranging from infrared movement detectors to actuators [5-9]. Most encountered examples include lead zirconium titanate (PZT) ceramic, barium titanate (BaTiO3).

The defining feature of all ferroelectrics is the presence of two stable spontaneous polarization states, $+P_r$ and $-P_r$, in thermal equilibrium at a temperature below the Curie temperature (Tc). Spontaneous polarization in a ferroelectric originates from a non-centrosymmetric arrangement of ions in its unit cell, which produces an electric dipole moment. Adjacent unit cells tend to polarize in the same direction and form a region called a ferroelectric domain. Most ferroelectrics have the ABO_3 perovskite structure shown in Fig 3.1.

Above the Curie temperature, ferroelectric materials have a centrosymmetric structure and therefore are non-polar, which is referred as paraelectric phase. As the temperature drops below T_c, a phase transition takes place from the paraelectric phase to

the ferroelectric phase, as illustrated in case (1), (2) of Fig. 3.1. During this transformation,

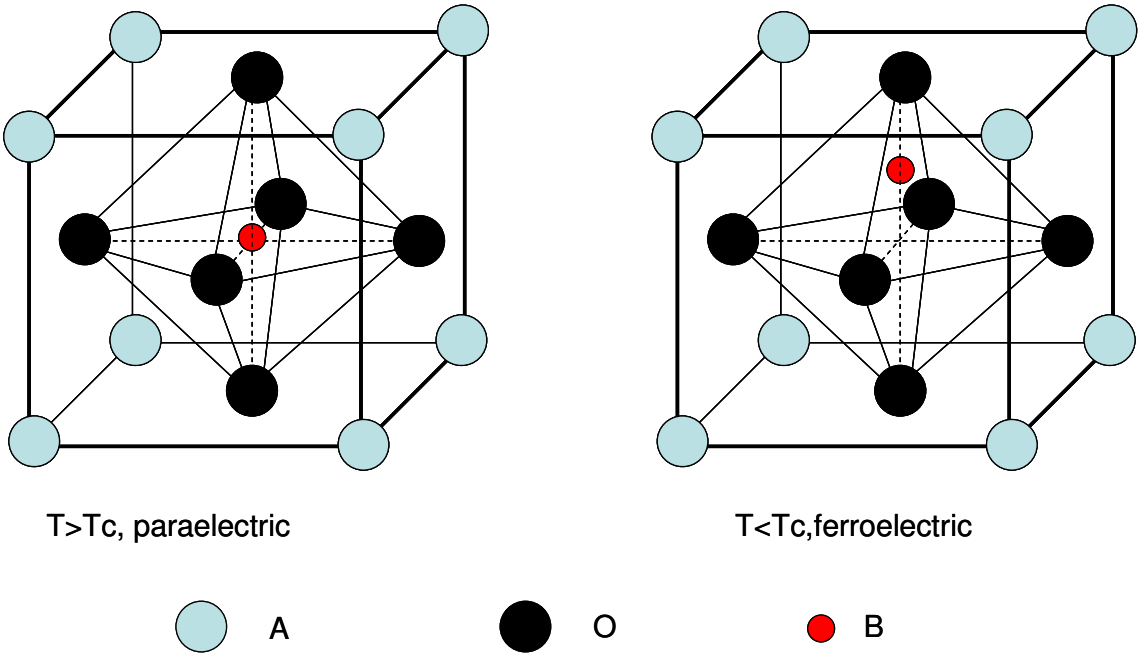

Figure 3.1 Unit cell of ABO_3 type perovskite structured material (1) paraelectric (2) ferroelectric phase.

the unit cell of the ferroelectric varies correspondingly. For example, the most studied ferroelectric PZT has a body centered cubic structure in its paraelectric phase with Zr^{4+} or Ti^{4+} at the center of the cube; however, in the ferroelectric phase the unit cell of PZT takes the non-symmetric structure with the Zr^{4+} or Ti^{4+} ion shifted up or down with respect to the oxygen octahedral. This displacement destroys the symmetry and causes a tetragonal distortion of the unit cell, leading to the two stable polarization states $+P_r$ and $-P_r$.

Different from linear dielectric materials, in which the relationship between the polarization and the electric field is linear, ferroelectric materials exhibit a non-linear, hysteresis loop field dependence for temperature below T_c, as shown in Fig. 3.2.

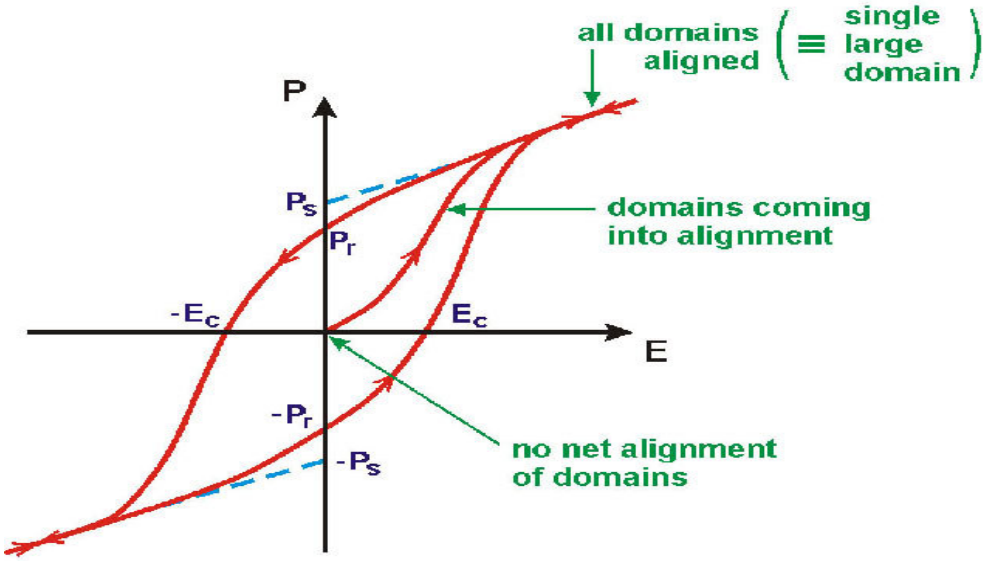

Figure 3.2 A schematic hysteresis loop of a ferroelectric material

In the initial stage, the ferroelectric domains that are oriented favorably with respect to the applied field direction grow at the expense of other domains. This continues until total domain growth and reorientation have occurred. At this stage, the material has reached its saturation polarization, P_s. If the electric field is then removed, some of the domains do not return to their random configurations and orientations. The polarization at this stage is called the remanent polarization, P_r. The strength of the electric field (voltage) required to return the polarization to zero is the coercive field

(voltage), E_c (V_c), which represents the minimum field (voltage) required to realize the polarization switching.

The physical significance of the spontaneous polarization is that it confers the largest relative permittivity of any type of capacitor dielectric, as well as a field-orientable polarization, which has been exploited in the manufacture of a range of piezoelectric and pyroelectric products. Although ferroelectric materials find applications in numerous fields, the primary impetus of recent research activity in this field is directed towards the development of nonvolatile random access memories [48].

As mentioned in the previous section, the two spontaneous polarization states in ferroelectrics can be reversed by an external electric field larger than the coercive field E_c (as in Fig. 3.2), and are considered to be able to encode the "1" and "0" of Boolean algebra that forms the basis of memory and logic circuitry in computers. The remanent polarization states can maintain themselves even if the electric field is absent, so memory based on ferroelectric materials has the ability to retain its data without the presence of electric field, which is usually denoted as non-volatile memory. Compared to conventional DRAMs, ferroelectric RAM (FeRAM) has several advantages: (i) low voltage operation (1.0V) (ii) small size (iii) high speed (iv) non-volatile [49].

When fabricated into memory devices, some practical problems limit the performance and application of ferroelectric materials, among them the most prominent being fatigue, retention and imprint. Fatigue is the decrease of the switched polarization in a ferroelectric material with an increase in the number of switching cycles. It describes the endurance of the device. Retention reflects the aging of the device. A ferroelectric memory cell won't keep the information forever without being refreshed. It loses

polarization slowly with time. If the polarization stored in the memory cell becomes so small or even reversed that it can not be read correctly by a sense circuit, we say the stored information is lost due to 'loss of retention'. Imprint is the tendency for ferroelectric memory cells to have a preferred state such that the switching speed from one state to the other is faster than the reverse switching. In order to make ferroelectric memory devices commercially available, all these problems have to be solved.

An ideal ferroelectric material for FeRAM purpose should have small dielectric constant, reasonable spontaneous polarization (~ 5 C/cm^2), and high Curie temperature (beyond the storage and operating temperature range of the device). Meanwhile, low voltage operation (< 5V) necessitates submicron layer thickness with low coercive field and adequate dielectric breakdown. Inherent switching speed should be in the nanosecond range or faster, and the ferroelectric memory cell should have good retention and endurance. The films must have very uniform composition and thickness over the surface of the integrated circuit so that the capacitance associated with each memory cell is the same. Also, the processing required to produce the ferroelectric thin film must not have a detrimental effect on the underlying circuitry.

The performance of ferroelectric memory devices depends on the spatio-temporal properties of individual ferroelectric domains. A better understanding of these properties requires experiments performed with nanometer spatial and sub-nanosecond temporal resolution.

Several methods exist to observe ferroelectric polarization. X-ray topography can be used due to variations in the Bragg angle from one domain to the next [50], Nematic liquid crystals in a layer on top of the crystal will align with the polarization, allowing

viewing of the domain structure with crossed polarizers. A pyroelectric probe involves locally heating the sample with a laser and detecting the sign of the pyroelectric current [51]. Electrostatic force microscopy can be used to image domains by measuring the local sign of the piezoelectric coefficient [52]. And AFM can be used to measure the surface topography of ferroelectric film so as to identify 90^o and 180^o domains[53].

If only topography information is needed, some other scanning microscopy techniques (e.g. SEM and AFM) may be better choices than NSOM, but NSOM has the advantages in that it has the possibility of making time-resolved measurements, and substantially smaller perturbation of the sample under investigation caused by the optical probe.

As a result, many attempts have been made [14-16] to implement different near-field optical techniques for second harmonic (SH) imaging. The main experimental problem in near-field SH imaging is low optical signal, since SHG is generally a weak effect, and it is extremely difficult to collect from a sub-wavelength area. In order to get enough SH photon collection, we have introduced an apertureless near-field optical technique for second harmonic imaging using a bare tapered optical fiber tip externally illuminated with femtosecond laser pulses. Our experiments showed that high spatial resolution is possible using this technique (on the order of 80 nm), and the SHG is sensitive to local crystal symmetry.

3.2 Near-field Second Harmonic Optical Imaging

To date most near-field work has been carried out in the linear, static region, because generally speaking the nonlinear effects are weak, and photon collection may not be easy with a nanometer aperture. However, surface nonlinear processes do have unique advantages in many cases. The most often used surface nonlinear process is second harmonic generation (SHG), which is a powerful tool for characterizing symmetry in surfaces and interfaces of samples [12].

When high intensity laser light interacts with materials, new optical frequencies could be generated by various intriguing nonlinear optical processes [12]. The basis for most theories in nonlinear optics is a Taylor expansion of the material polarization P in powers of the electric field E, which in a scalar version looks like

$$P = \varepsilon_0(\chi^{(1)}E + \chi^{(2)}E^2 + \chi^{(3)}E^3 + \cdots), \tag{3.1}$$

where $\chi^{(1)}$ is the well-known linear susceptibility ($n^2 = \varepsilon_r = 1 + \chi^{(1)}$), whereas $\chi^{(n)}$ is the coefficient for the n-th order nonlinear process. The higher order terms are termed nonlinear polarization

$$P^{NL} = \varepsilon_0(\chi^{(2)}E^2 + \chi^{(3)}E^3 + \cdots), \tag{3.2}$$

An important symmetry aspect of the above Taylor expansion is that all even-order coefficients must disappear for media with inversion symmetry. The explanation can be simply stated: the operation $\vec{r} \to -\vec{r}$ leaves the inversion-symmetric media unaffected, but adds minus signs to both P and E. This is only possible when $\chi^{(n)} = 0$ for even n.

The relative weight of the nonlinear terms is determined by the strength of the incident electro-magnetic field as compared to the atomic field, i.e.

$\chi^{(n)}/\chi^{(1)} \propto (E_{light}/E_{atom})^{n-1}$. For weak to moderate incident fields the material response is linear to a very good approximation. Actually, linear optics can be regarded as a special case of nonlinear optics at low optical intensity. At larger fields higher-order terms in the Taylor expansion become noticeable as the response of the charged particles inside the atoms becomes nonlinear.

When only second order nonlinear processes are considered, the nonlinear polarization in (3.2) can be truncated after the first term, i.e.,

$$P^{NL} = P^{(2)} = \chi^{(2)} E^2, \tag{3.3}$$

Optical second harmonic generation (SHG) is a second order nonlinear optical process which was first demonstrated in 1961 in crystalline quartz irradiated by a ruby laser [54]. The process of optical second harmonic generation is described in Fig. 3.3. A single pump wave, the fundamental, at frequency ω, is incident on a nonlinear medium and generate a wave at the second harmonic frequency 2ω.

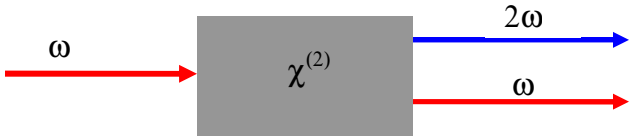

Figure 3.3 Schematic illustration of the optical second harmonic generation process

The technological significance of the SHG process was at first primarily in the area of generating coherent radiation at new frequencies that are not usually available with lasers. Another importance application of SHG is the characterization of surfaces and polar structures due to the fact that in centro-symmetric materials there is no SHG in

the bulk under dipole approximations [13]. Optical SHG is suitable to imaging surfaces, interfaces and other media without inversion symmetry (such as polar structures and chiral structures).

SHG signals have well defined polarizations. SH intensity and polarization depend on the orientation, polarization, and local symmetry properties of polar structures. Therefore, it is useful for extracting information about the organization of asymmetries in materials.

SHG microscopy has already been used in the characterization of semiconductor surfaces [13], ferromagnetic and ferroelectric materials [14-16] and biological samples [55]. Our concern in the current chapter is the imaging of domain structures in ferroelectric thin films. Optical imaging of ferroelectrics has been pursued for a long time. SHG imaging gives better contrast due to the relation between SH signal and domain polarization, which is not obvious in linear case. Far field SH imaging of ferroelectrics yields only micrometer resolution [56]. The combination of NSOM and SHG provides a powerful tool for surface and thin film characterization. With near-field SH microscopy, it is possible to image ferromagnetic and ferroelectric domains and domain walls. And since the technique uses light as probe, it is possible to carry out local fast time-resolved measurements, which have great potential for optical probing and characterization of materials, surfaces, and thin films on the nanoscale, both spatially and temporally.

3.3 Experimental Setup

$Pb(ZrTi)O_3$ (PZT) is the most commonly studied and commercially used ferroelectric material in thin film form. It is grown on silicon wafers by pulsed laser deposition (PLD) with a thickness between 200nm to 500nm in our experiments. In this section we use NSOM to observe the local distribution of SHG on the PZT film surface and explain the mechanism between the SHG and material polarization.

The experimental setup is shown in Fig.3.4. Weakly focused light (illuminated spot diameter on the order of 50 μm) from a Ti:sapphire laser system consisting of an oscillator and a regenerative amplifier operating at 810 nm (COHERENT Mira 900 and RegA 9000, repetition rate up to 250 kHz, 150-fs pulse duration, and up to 10 μJ pulse energy) was directed at an angle of incidence around 50^o onto the PZT sample surface. Excitation power at the sample surface was kept well below the ablation threshold. The local SHG was collected using an uncoated adiabatically tapered fiber tip, which is drawn at the end of a single mode fiber by the standard heating and pulling procedure using a commercial micropipette puller. Tip curvature was measured using a scanning electron microscope (SEM). The apex diameter of the probe tip was on the order of 30nm-50nm. The fiber tip was scanned over the sample surface with a constant tip-surface distance of 5-10 nanometers using shear force feedback control. Therefore, surface topography images were obtained while simultaneously recording the SH near-field images. A blue glass was used to cut off fundamental light and allow only SH at 400nm passed to the photomultiplier tube (PMT). Due to the low signal level of the SHG, a photon counter (SR400) was used to count the SH photons. A typical count rate for SH photons was around 100-200 photons/s for PZT thin films.

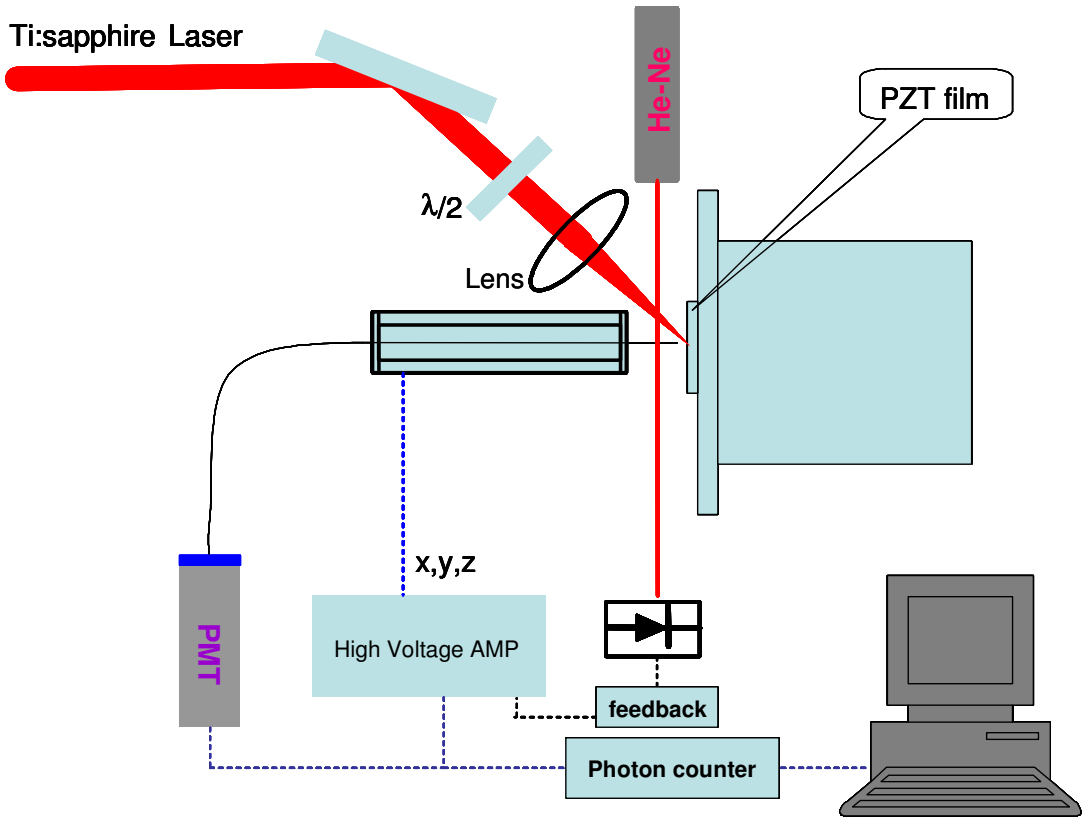

Figure 3.4. Schematic view of the near-field SH microscopy setup. Shear force detection was realized by monitoring the amplitude change of diffracted He-Ne laser light by the fiber tip. The sample is mounted on a solid mount, while the fiber tip is scanned using a piezo-tube actuator. Different polarization directions of the fundamental light can be achieved by rotating the half wavelength (λ/2) plate.

3.4 Exploration of the Relationship between Local SH Intensity and Polarization Direction of the Ferroelectrics

The nonlinear optical process of second-harmonic generation offers a high degree of intrinsic sensitivity for probing asymmetries in materials. This feature has lead to wide spread application of the method as a purely optical probe of polar structures in both inorganic and organic objects. The inherent mechanism of the technique derives from the symmetry constraint mentioned in the introduction: the second-order nonlinear optical processes are symmetry forbidden in the bulk of materials with inversion symmetry. The consequence of this constraint is that the contrast in SH image of non-centrosymmetrical samples is enhanced compared to linear optical imaging.

When imaging the ferroelectric thin film with surface SHG technique, we expect to observe the dependence of the SH intensities on the polarization direction of ferroelectric materials. The following section describes our effort in defining this relation both experimentally and theoretically. This will provide a basis for understanding and analyzing the near-field optical SH images of ferroelectric materials.

3.4.1 Experimental Study of Local SH Signal Dependence on Incident Light Polarization States

A poled single crystal of $BaTiO_3$ was used to study the relation between local SH intensity and ferroelectric polarization directions. $BaTiO_3$ and PZT have similar perovskite structures and belong to the same tetragonal symmetry class. So the relation set up using $BaTiO_3$ will also work for PZT thin films. The difference in SH generated from thin films and bulk crystals can be eliminated due to the fact that phase-matched

SHG is prohibited in the bulk of $BaTiO_3$ because of its strong dispersion. As a result, the measured SH signal originates at the surface, which makes the experimental situation look very similar to the case of a thin film, with known polarization directions.

For memory devices the domains of main concern are those with polarization direction perpendicular to the sample surface (c-domain). C-domains can be switched easier and faster than in-plane ones (a-domain). So PZT thin films are usually engineered to have more c-domain components while a-domains only serve as domain walls to separate different c-domains, as in Fig. 3.5.

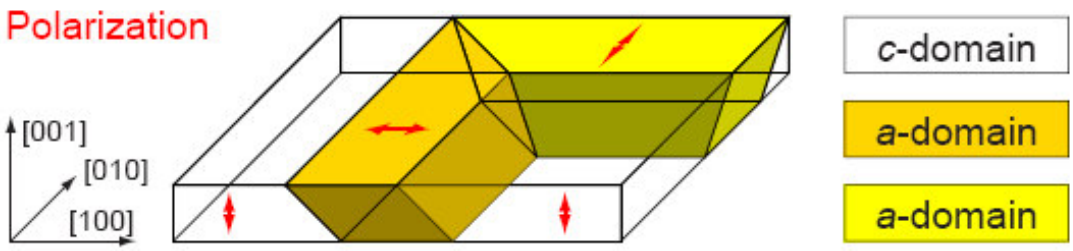

Figure 3.5 Illustration of domain structures in PZT thin films

Using single crystal $BaTiO_3$, the SH signal dependence on domain polarizations are studied in three different cases, corresponding to c-domain and a-domains, respectively. The experimental configurations are illustrated in Fig. 3.6. Fundamental light is incident on the crystal at an angle α, and the polarization of the light can be changed continuously with a half wavelength plate. In the graph, S and P polarizations of light are indicated. The Z-axis was chosen to be the optical axis of the crystal. Cases (a) and (b) correspond to a-domain while case (c) corresponds to c-domain. For each case,

the polarization of light is changed from 0 to 2π, and at each angle, the SH signal are locally collected using a tapered fiber probe.

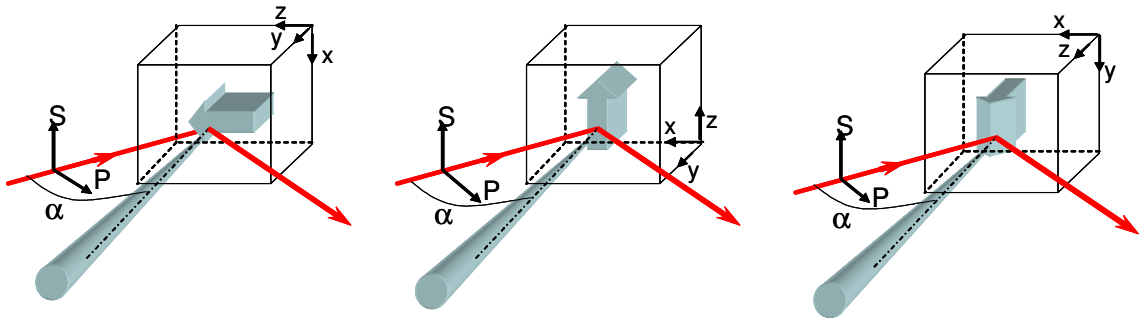

(a) (b) (c)

Figure 3.6. Orientation of the $BaTiO_3$ crystal with respect to the illuminating fundamental light. The arrow represents polarization direction of the crystal.

The near-field SH signal dependencies on the polarization of the fundamental light for the three cases are shown in Fig.3.7.

Case (a): poling (optical axis) direction located in the incidence plane of the fundamental light parallel to the crystal surface: The SH signal from near-field of the crystal exhibits approximate 4-fold symmetry with respect to polarization angle rotation of incident light in the 2π span.

Case (b): the optical axis of the crystal is perpendicular to the incidence plane of the fundamental light and parallel to the crystal surface: The symmetry of the fundamental light polarization dependence becomes 2-fold.

Case (c) the optical axis is perpendicular to the crystal surface: the SH signal is much weaker than in cases (a) and (b), while also showing a 2-fold symmetry.

Big differences between these dependencies indicate that the near-field SHG may be used to recover local poling direction in thin ferroelectric films. In order to do this, we must achieve some theoretical understanding of the reasons for such a difference.

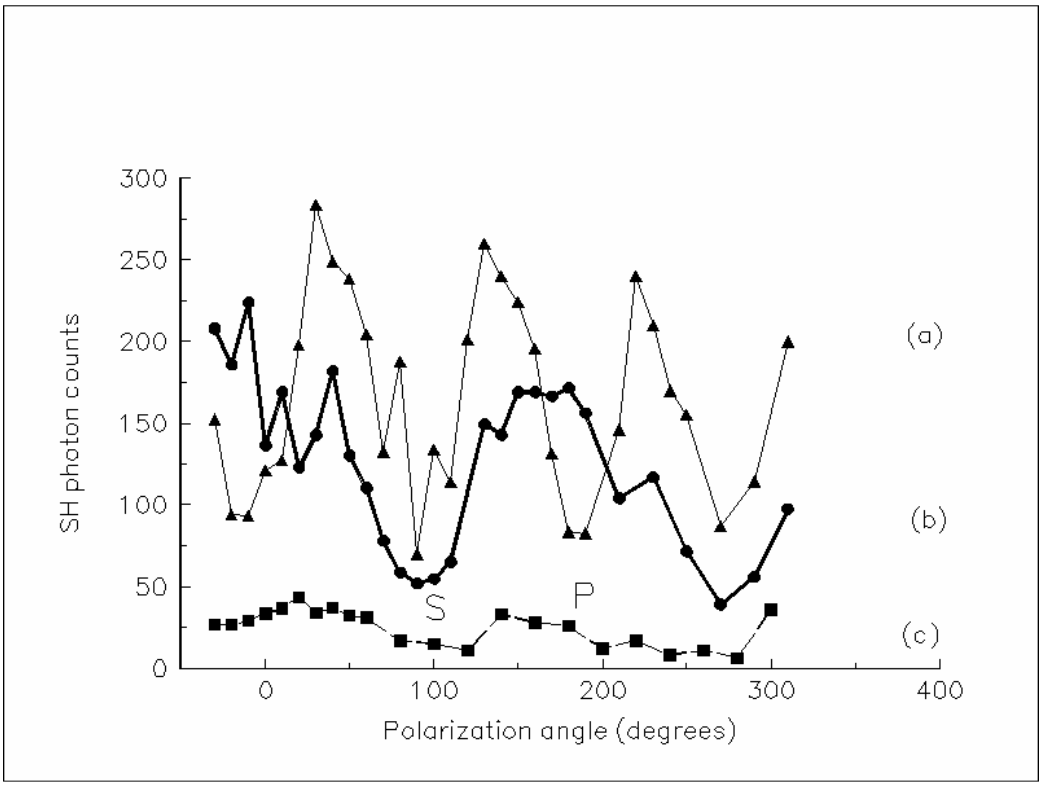

Figure 3.7 Near-field SH signal dependencies on the polarization of fundamental light for three different poling directions of $BaTiO_3$ crystal (shown by the arrows in Fig. 3.6) with respect to the incoming fundamental light (shown by the straight lines in Fig. 3.6). P- and S- polarization directions of the fundamental light are indicated.

3.4.2 Theoretical Explanation of the Local Second Harmonic Signal Dependence on Fundamental Light Polarization

Consider fundamental light illuminating the tip of the near-field microscope located near the $BaTiO_3$ crystal surface. Let us consider the fundamental optical field distribution in the tip-sample region at distances much smaller then the wavelength λ of the fundamental light. In this region the quasi-electrostatic approximation may be used. The tip shape may be approximated as an ellipsoid with a very high aspect ratio.

For P-polarized excitation light and y-component (the component perpendicular to the sample surface, as in Fig. 3.8) of the optical field the exact analytic solution of the Laplace equation [19] gives:

$$E_{local}(\omega)=\varepsilon E_{tip}(\omega)=\varepsilon E_{0y}(\omega) \qquad (3.4)$$

where ε is the dielectric constant of the tip, E_{0y} is the incoming field and E_{tip} is the y-component of the field inside the fiber tip and E_{local} is the electric field just below the tip apex.

As a result, for incidence angles α around $\pi/2$ the local SHG under the tip is enhanced by a factor of n^8 due to

$$I(2\omega)_{local}=E^2_{local}(2\omega)=E^4_{local}(\omega)=n^8E^4_{0y}(\omega) \qquad (3.5)$$

where n is the refractive index of the fiber tip. Assuming n=1.46 for SiO_2, the enhancement factor equals about 20. It may be even higher (of the order of $(2\varepsilon)^4$) in the vicinity of a sample surface with a high dielectric constant, such as a metal or a ferroelectric, due to the image potential. Exact tip enhancement factors in non-linear near-field microscopy were calculated by Y. Kawata *et al.* [57] for different tip-sample pairs. For example, in the case of a diamond/air/diamond tip-sample gap E^4_{tip} may be

enhanced by a factor of 600. However, in our discussion to follow, we will not consider any particular value of the field enhancement factor. Instead, we denote the fundamental field enhancement factor by γ.

In the following section we will consider the three cases separately, using the following non-zero components of the second harmonic susceptibility tensor for $BaTiO_3$:

$\chi^{(2)}_{yyz} = \chi^{(2)}_{xxz} = \chi^{(2)}_{yzy} = \chi^{(2)}_{xzx} = 17.7 \times 10^{-12}$ m/V,

$\chi^{(2)}_{zyy} = \chi^{(2)}_{zxx} = -18.8 \times 10^{-12}$ m/V, and

$\chi^{(2)}_{zzz} = -7.1 \times 10^{-12}$ m/V

where z is the ferroelectric polarization direction [58].

Case (a):

The fundamental optical field components under the tip apex at a polarization angle ϕ can be written approximately as:

$$E_x = E \sin\phi, \tag{3.6}$$

$$E_y = (\gamma/\varepsilon_b)\, E \cos\phi \sin\alpha, \tag{3.7}$$

$$E_z = E \cos\phi \cos\alpha \tag{3.8}$$

where ε_b is the dielectric constant of $BaTiO_3$, ϕ=0 and ϕ=90^o correspond to P-polarized and S-polarized excitation light respectively, as is illustrated in Fig. 3.8. The field components are written assuming no light is reflected from the tip-sample interface area or from the sample substrate. Taking into account the reflected field would modify to some extent the effective value of factor γ in (3.7), leaving polarization dependencies of SHG basically intact.

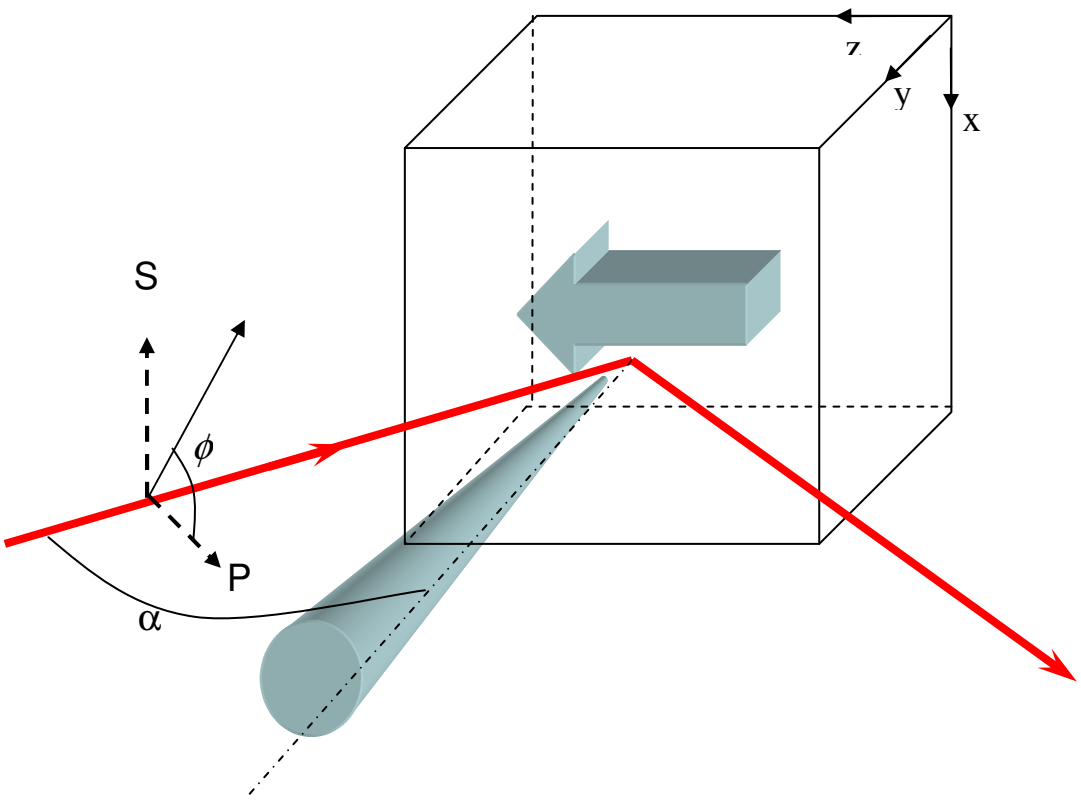

Figure 3.8 Illustrations of the parameters of the theoretical calculations

The second harmonic field components at the tip apex may be written as:

$$P^{(2)}_x = \chi^{(2)}_{xzx} E^2 \sin 2\phi \cos\alpha, \tag{3.9}$$

$$P^{(2)}_y = (\gamma/\varepsilon_b)\chi^{(2)}_{yzy} E^2 \cos^2\phi \sin 2\alpha, \tag{3.10}$$

$$P^{(2)}_z = (\gamma^2/\varepsilon_b{}^2)\chi^{(2)}_{zyy} E^2 \cos^2\phi \sin^2\alpha + \chi^{(2)}_{zxx} E^2 \sin^2\phi + \chi^{(2)}_{zzz} E^2 \cos^2\phi \cos^2\alpha \tag{3.11}$$

If we assume that the microscope tip collects only dipole radiation, the second harmonic optical signal will be proportional to

$$I^{(2)} = P^{(2)}_z{}^2 + P^{(2)}_x{}^2 \tag{3.12}$$

There is no y component because SH dipoles that oscillate along the y-direction do not radiate towards the tip. Similar calculations of the field at the tip apex are easy to perform for cases (b) and (c).

Case (b):

The fundamental light components:

$$E_x = E\cos\phi\cos\alpha, \tag{3.13}$$

$$E_y = (\gamma/\varepsilon_b)\, E\cos\phi\sin\alpha, \tag{3.14}$$

$$E_z = E\sin\phi, \tag{3.15}$$

The SH field components can be expressed as:

$$P^{(2)}_x = \chi^{(2)}_{xzx} E^2 \sin 2\phi\cos\alpha, \tag{3.16}$$

$$P^{(2)}_y = (\gamma/\varepsilon_b)\chi^{(2)}_{xzx} E^2 \sin 2\phi\sin\alpha, \tag{3.17}$$

$$P^{(2)}_z = (\gamma^2/\varepsilon_b^2)\chi^{(2)}_{zxx} E^2\cos^2\phi\sin^2\alpha + \chi^{(2)}_{zxx} E^2\cos^2\phi\cos^2\alpha + \chi^{(2)}_{zzz} E^2\sin^2\phi \tag{3.18}$$

So the collected SH signal is:

$$I^{(2)} = {P^{(2)}_z}^2 + {P^{(2)}_x}^2 \tag{3.19}$$

Case (c)

Fundamental field components can be written as:

$$E_x = E\cos\phi\cos\alpha, \tag{3.20}$$

$$E_y = E\sin\phi, \tag{3.21}$$

$$E_z = (\gamma/\varepsilon_b)\, E\cos\phi\sin\alpha, \tag{3.22}$$

Considering the 2nd order susceptibility tensor, the SH field components are equal to:

$$P^{(2)}_x = (\gamma/\varepsilon_b)\chi^{(2)}_{xzx} E^2\cos^2\phi\sin 2\alpha, \tag{3.23}$$

$$P^{(2)}_y = (\gamma/\varepsilon_b)\chi^{(2)}_{yzy} E^2\sin 2\phi\sin\alpha, \tag{3.24}$$

$$P^{(2)}_z = \chi^{(2)}_{zxx} E^2\cos^2\phi\cos^2\alpha + \chi^{(2)}_{zyy} E^2\sin^2\phi + (\gamma/\varepsilon_b)^2\chi^{(2)}_{zzz} E^2\cos^2\phi\sin^2\alpha \tag{3.25}$$

Thus the dipole radiation of SH to the tip is:

$$I^{(2)} = P^{(2)}{}_{y}{}^{2} + P^{(2)}{}_{x}{}^{2} \qquad (3.26)$$

The final results of our calculations are presented in Fig.3.9. The best agreement with experimentally measured symmetry properties of the near-field SH polarization curves was achieved in the $\gamma = 5$ -7 range for the field enhancement factor. This is reasonably close to the expected value of $\gamma = 2\varepsilon_{tip}$. A much smaller value of the SH signal in case (c) is a consequence of the fact that $I^{(2)}$ contains terms proportional to $<\gamma^4>$ in the cases (a) and (b), but in case (c) the SH signal $I^{(2)}$ is proportional to $<\gamma^2>$, as can be seen from equation (3.23-3.26).

One thing to mention is that within our model the angular dependencies of the field E for the points in space around the tip apex should be approximately the same as the above equations. Only the enhancement factor γ is different for these points (its value changes from a maximum just under the tip apex to γ=1 far from the apex). So, in the final result one must replace the factors γ^4 and γ^2 by the average values $<\gamma^4>$ and $<\gamma^2>$ taken over all the area around the tip apex where the SH signal is collected. The diameter of this area is approximately $\lambda_{2\omega}/3$ - $\lambda_{2\omega}/2$, which is the theoretical resolution limit of near-field optical microscopy in the collection mode performed with uncoated fiber tips [59].

Exact calculation of the near-field distribution of the excitation light in the tip-sample region must take into account all kinds of additional complications, such as tensor relations between local and excitation fields, retardation, real shape of the tip, sample roughness, etc.

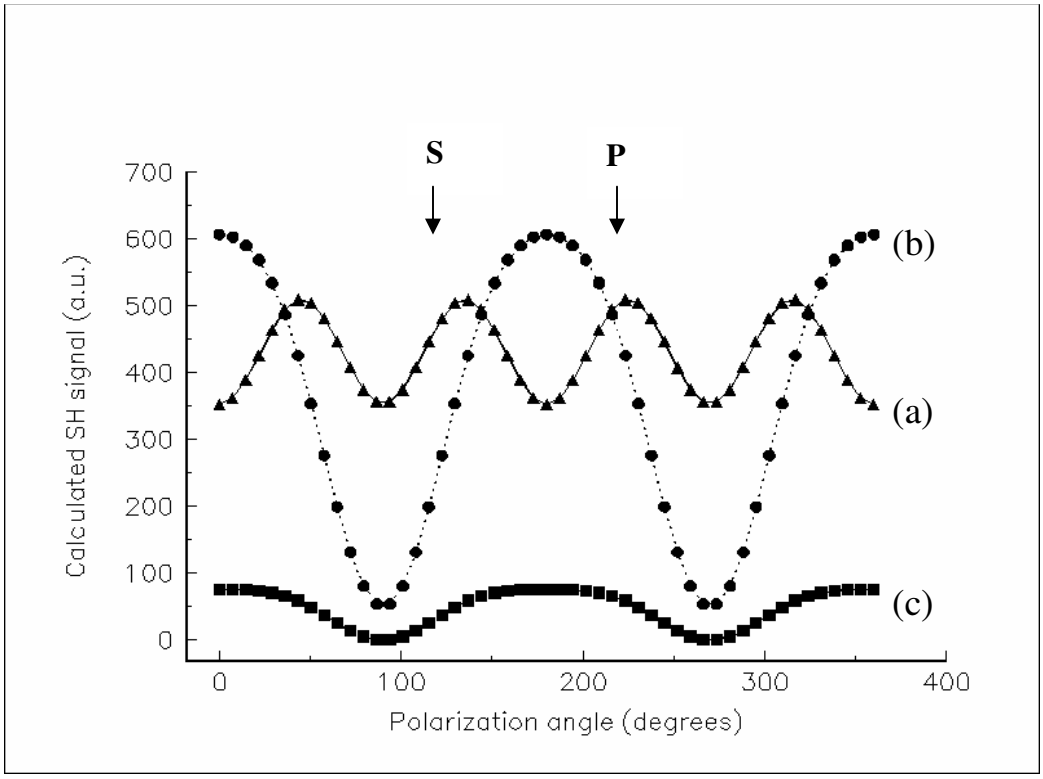

Figure 3.9 Theoretical near-field SH signal dependencies on the polarization angle of fundamental light obtained in the geometry (a), (b) and (c) from Fig.3.6 for the field enhancement factor $\gamma = 7$ and $\alpha = 45^{o}$. S-, P- marked the angle corresponding to S and P polarized incident light.

3.4.3 Check Validity of the Symmetry Behavior of Local SHG: Near-, Far-field Transition

The transition from near-field mode to far-field mode operation of the microscope (which corresponds to an increase in the tip-sample separation from 5-10 nanometers to a distance of a few wavelengths of light) can be described mathematically within our model as a transition from $\gamma = 5 - 7$ to $\gamma \cong 1$ (no field enhancement by the tip). Results of numerical calculations for such a transition performed using Eq. (3.19) are shown in Fig.3.10. Experimental data shown in the same figure are in good qualitative agreement with the calculations: both theoretical and experimental data have the same symmetry of the SH polarization dependencies in the near-field and far-field zones. This indicates that our simple model provides an adequate description of the essential physics involved in near-field observation of SHG from ferroelectric samples.

It should be pointed out that an exact theoretical consideration of the fundamental and second harmonic near-field distributions in the tip-sample region must take into account all kinds of additional complications, such as tensor relation between local and excitation fields, retardation, real shape of the tip, sample roughness, etc. Such a consideration is highly necessary. Nevertheless, the success of our scalar model in describing experimental results, and giving a value of the local enhancement factor γ of the order of $2\varepsilon_{tip}$ necessary for good agreement of theory and experiment, makes the model credible and of considerable value in qualitative understanding of the basic physics involved in near-field SHG.

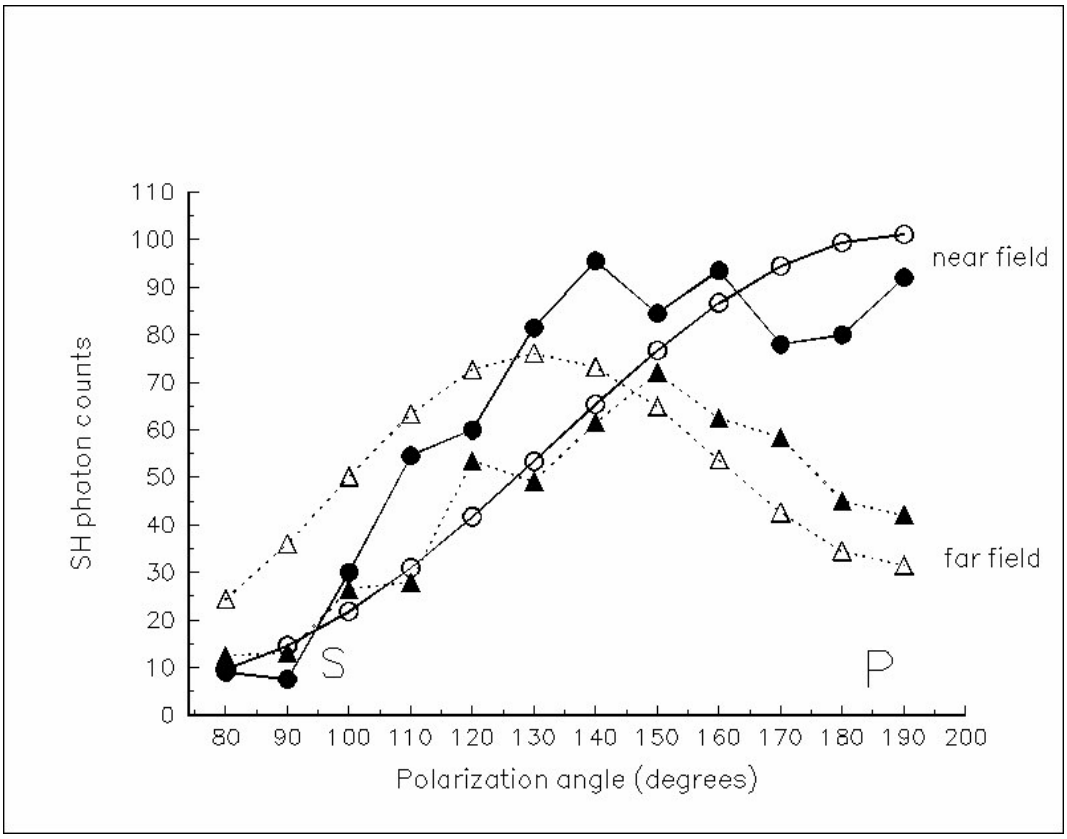

Figure 3.10 Theoretical (open circles and triangles) and experimentally measured (filled circles and triangles) data for the transition from the near-field to the far-field behavior of the SH signal polarization dependency for geometry (b) from Fig.3.6.

3.5 Near-field SH Microscopy of Polycrystalline PZT Thin Film

A typical set of topology and SH images of a 0.5μm thick pulsed laser deposited PZT film grown on a Si wafer substrate obtained under excitation with P- and S-polarized fundamental light is presented in Fig.3.11. The topographical image in Fig.3.11 (a) shows the grain structure of the film. Higher than usual noise in the image is caused by less stable behavior of the shear-force feedback control when the tip is illuminated with femtosecond laser pulses. The SH image in Fig.3.11 (b) obtained under illumination with P-polarized fundamental light clearly shows fine structure of SHG within individual grains. Fundamental light distribution was also measured and did not show any variations on this scale.

From Fig. 3.7 and Fig. 3.9 we can see that for P-polarized fundamental light illumination the contrast is better than S-polarized light illumination for different orientated ferroelectric domains, which is as we observed in experiments in Fig. 3.11 (b) and (c).

By measuring the smallest non-artifact features on the near-field SH image, the resolution of the microscope is estimated to be around 80nm.

Usually for uncoated fiber tips it is believed the resolution is around $\lambda_{2\omega}/2$~200nm. The rather high resolution in the experiments results from the local enhancement of the SH field under the tip.

From the theoretical discussion above and the experimental data shown in Fig.3.7 it is clear that the fundamental field component parallel to the microscope tip (and perpendicular to the sample surface) is enhanced by a factor γ of the order of $\gamma = 5 - 7$.

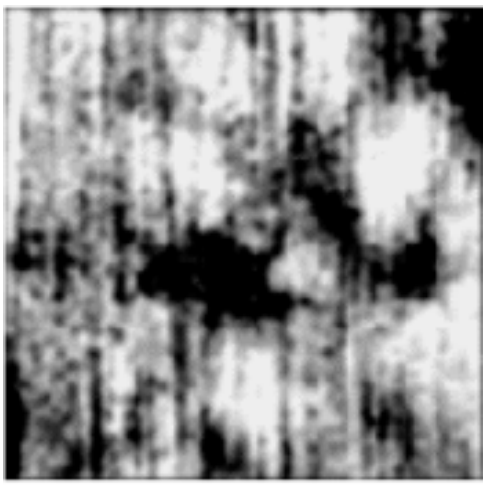

(a)

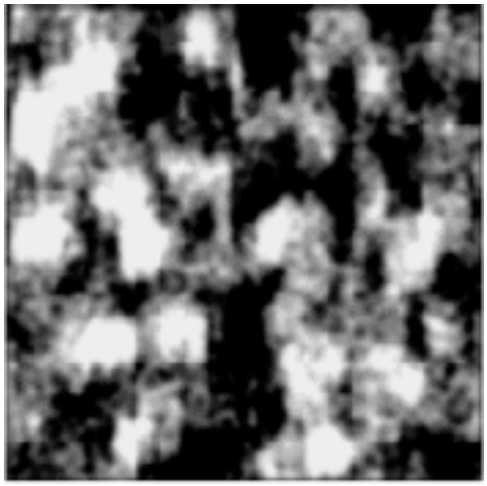

(b)

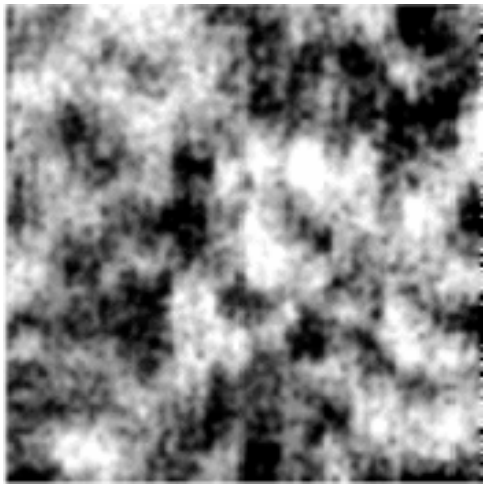

(c)

Figure 3.11 Simultaneously measured (a) shear-force topographical and (b), (c) SH near-field optical images of a 0.5um thick PZT film surface obtained with p- and s- polarized excitation light, respectively. The sizes of the images are 3x3um. Height variation within the topographical images is 82nm.

This leads to the local SH signal enhancement at the tip apex by a factor of up to γ^4 for P-polarized excitation light. The fiber tip of the microscope collects SHG from a sample area limited by a circle with a diameter on the order of $\lambda_{2\omega}/2$, where $\lambda_{2\omega}$ is the wavelength of SH light. But the sample area just below the tip dominates the resulting SH signal. As a result, the resolution of the microscope in the SH mode is determined by the fiber tip diameter d, which was on the order of 50 nm in our experiments. Even better resolution may be expected using thinner tips or tips with higher refractive indices. The tip contribution and the contribution from all the other sample surface become equal at a tip diameter determined by $\gamma^4 d^2=(\lambda_{2\omega}/2)^2$ or $d=\lambda_{2\omega}/(2\gamma^2)$ which may be as small as 10 - 30 nm. In fact, more severe limitations on the resolution of the microscope are caused by the small number of SH photons collected by the microscope tip. In our setup the SH signal was measured with a photomultiplier and a gated photon counter. The gate was open only for the duration of a single photon pulse from the photomultiplier in sync with the femtosecond pulses of the laser. The SH signal at every point of the image was averaged over 100-300 ms. The characteristic SH photon counting rate was on the order of one photon count per 100-300 laser pulses. Thus, the image acquisition time was on the order of 20-30 minutes. Further increase of the microscope resolution is limited by the time of measurement and hence the stability of the measuring system rather than by achievement of a better tip geometry.

Another factor limiting the resolution of the microscope is the depth of probing, which is determined by two main factors. The first one is the volume distribution of SHG. In the two cases discussed so far (the case of $BaTiO_3$ crystal, and the case of a thin film) this distribution may be considered to be quasi two-dimensional. There will not be

the case, though, for any kind of sample. In general, the coherence length of SHG in the sample should strongly affect the optical resolution, and must be seriously considered. The second factor is the depth of optical interaction of the tip and sample which defines the sample region where SH light is generated and collected. Based on the above discussion of the fundamental field enhancement by the microscope tip, this interaction depth should be at least of the order of the tip end diameter. This consideration is especially important in the domain imaging application, since in general the domain walls (such as 90 degree walls) are not perpendicular to the sample surface. The SHG response in the region of the domain wall is supposed to be a phase correlated signal from two domains within the depth probed.

3.6 Measurements of Local Poling Direction in Thin PZT Films

As an attempt to recover the polarization directions inside the ferroelectric thin film, we performed similar local polarization properties measurements in different areas of thin $BaTiO_3$ and $Pb(Zr_xTi_{1-x})O_3$ films. An example of such measurements is presented in Fig.3.13. The data obtained at points 1-3, 8-9 and 4-7 of Fig.3.12 (b) show close resemblance to the curves (a), (b) and (c) respectively in Fig.3.7. Optical properties of $Pb(Zr_xTi_{1-x})O_3$ and $BaTiO_3$ are similar to each other, with $Pb(Zr_xTi_{1-x})O_3$ (or PZT) having somewhat higher values of refractive index and nonlinear susceptibility: n_o=2.610 and n_e=2.611 at 800 nm; n_o=2.966 and n_e=2.967 at 400 nm; $\chi^{(2)}_{yyz} = \chi^{(2)}_{xxz} = \chi^{(2)}_{yzy} = \chi^{(2)}_{xzx}$ =37.9x10^{-12} m/V, $\chi^{(2)}_{zyy} = \chi^{(2)}_{zxx}$ = - 42.8x10^{-12} m/V, and $\chi^{(2)}_{zzz}$ = -8.5x10^{-12} m/V at 1060 nm [60],[61]. Thus, our theoretical analysis performed for $BaTiO_3$ should also be applicable to PZT films. As a result, the localized areas of dark and bright SHG in

Fig.3.12 (b) may be identified as regions with different domain orientations. High spatial resolution of the near-field SH measurements is evidenced by observation of sudden symmetry changes in SH polarization dependencies performed with 45 nm spatial steps. After obtaining the topographical and SH images in Fig.3.12 (a) and Fig.3.12 (b) respectively, we have performed point by point measurements of local SH polarization dependencies over the region which show clear change in SH contrast. These measurements were done by moving the tip in 45 nm steps from left to right through the points on the film surface indicated in both the topographical and SH images. The data obtained are shown in Fig.3.13, where the curves are numbered in succession. A clear transition from 4-fold symmetry (curves 1-3) to 2-fold symmetry (curves 8 and 9) has been observed with a narrow intermediate region (curves 4-7) which does not show any polarization dependence of SHG.

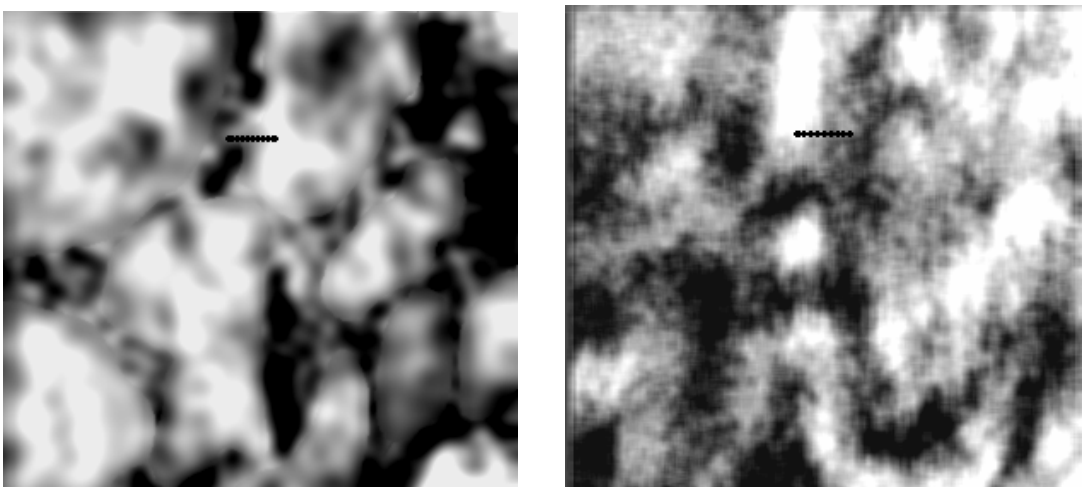

(a) (b)

Figure 3.12 Simultaneously measured (a) topographical and SH near-field optical image (b) of a PZT film. 3 μm by 3 μm images were obtained using P- polarized excitation light. Height variation within the topographical image is 75 nm.

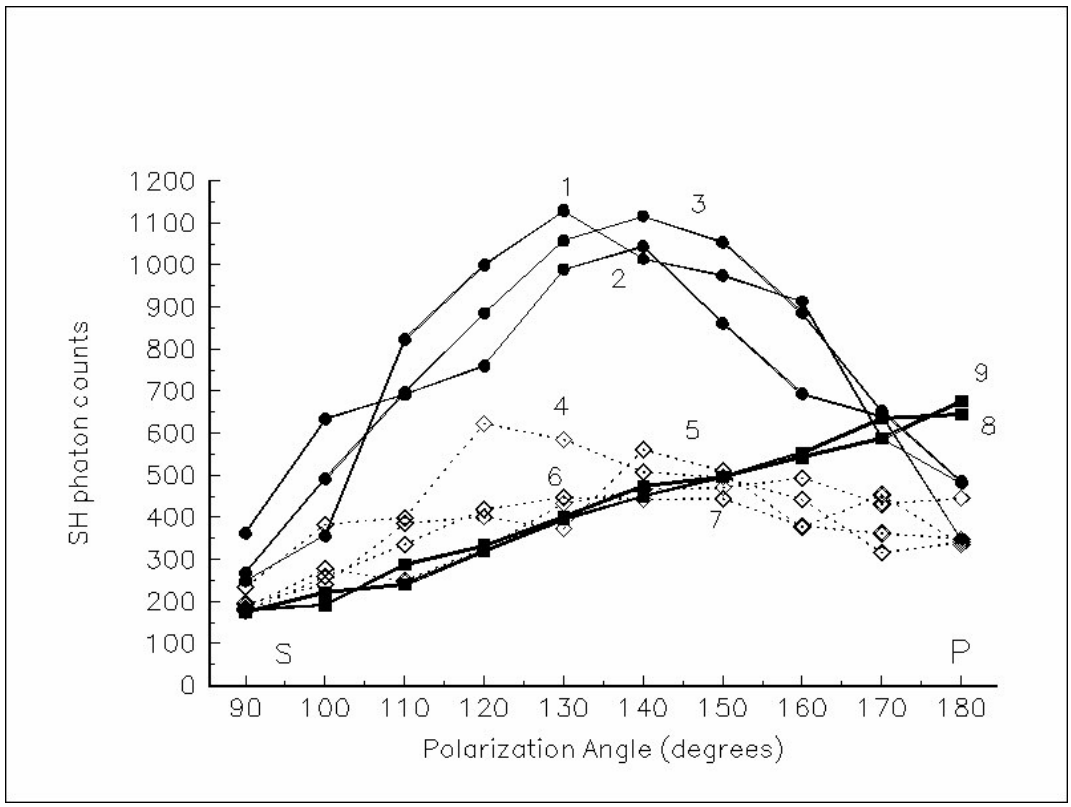

Figure 3.13 Symmetry transition in different areas of the SH image. Polarization curves are measured at each point as marked in Fig. 3.12. The spacing between the points is 45 nm. The points are numbered in succession from left to right.

3.7 SH Imaging of a/c/a/c Polydomain PZT Thin Films

Compared to polycrystalline films, polydomain PZT films have less randomness, however, give lower SH signal due to their thickness (usually around 200nm).

Polydomain c/a/c/a structures are commonly observed in thin epitaxial $PbZr_xTi_{1-x}O_3$ films in the $0<x<0.4$ range, and in many other ferroelectric films such as $BaTiO_3$, $PbTiO_3$, $KNbO_3$, etc. [62]. The domains in the film can be classified in two groups: a-domains (those with polarization in plane, with the c axis of the tetragonal film along either [100] or [010] directions of the substrate) and c-domains (those with polarization direction perpendicular to the surface). The a-, c- domains alternate in the film and form grid structures, as shown in Fig. 3.14 (c). Generally the c-domains have larger area, separated by a-domains of lateral thickness 20-50nm. This kind of film has a smoother surface. In the topography image we see no variations at all (Fig. 3.14 (a)). The SH image in Fig.3.14(b) obtained under illumination with P-polarized fundamental light clearly shows fine grid-like structure of SHG from the film surface consistent with the known arrangement of c- and a-domains in the film that is visible in the high vertical resolution AFM image of the film in Fig.3.14 (c) (not the same area as image (b)). Spatial distribution of fundamental light was also measured and did not show any similar variations on this scale.

Ideally the SH image will show a grid like structure resembling the AFM image of Fig 3.14 (c), as a result of the relation of SH to the direction of the tetragonal axis's of the domains. But what we actually observed using P-polarized fundamental light illumination was an SH distribution with larger features. The reason was that the resolution of the NSOM was on the order of 100nm for SH imaging in our experiments.

This forbid us to see the a-domains with enough resolution. What we got is a comprehensive effect with several domains contributing.

Considering (1) the resolution of the microscope; (2) contribution of SH signal by a-, c- domains; and (3) local field enhancement for different field components, we calculated the spatial distribution of local SHG from a typical $PbZr_xTi_{1-x}O_3$ film area showing c/a/c/a polydomain structure. The results of such calculations are presented in Fig.3.14 (d) for the case of P-polarized excitation light. The calculated image has the similar periodic bright and dark regions, qualitatively resembling the experimental images. As it is evident from Fig.3.7, SHG from c-domains forms a low background of the image. Much brighter SHG from 20-50 nm wide a-domains forms a grid-like structure that corresponds to the real geometry of domains (with some corrugations due to the 100 nm spatial resolution of the microscope). Thus, the bright grid-like features observed in Fig. 3.14(b) may be identified as contributions from a-domains of the $PbZr_xTi_{1-x}O_3$ film.

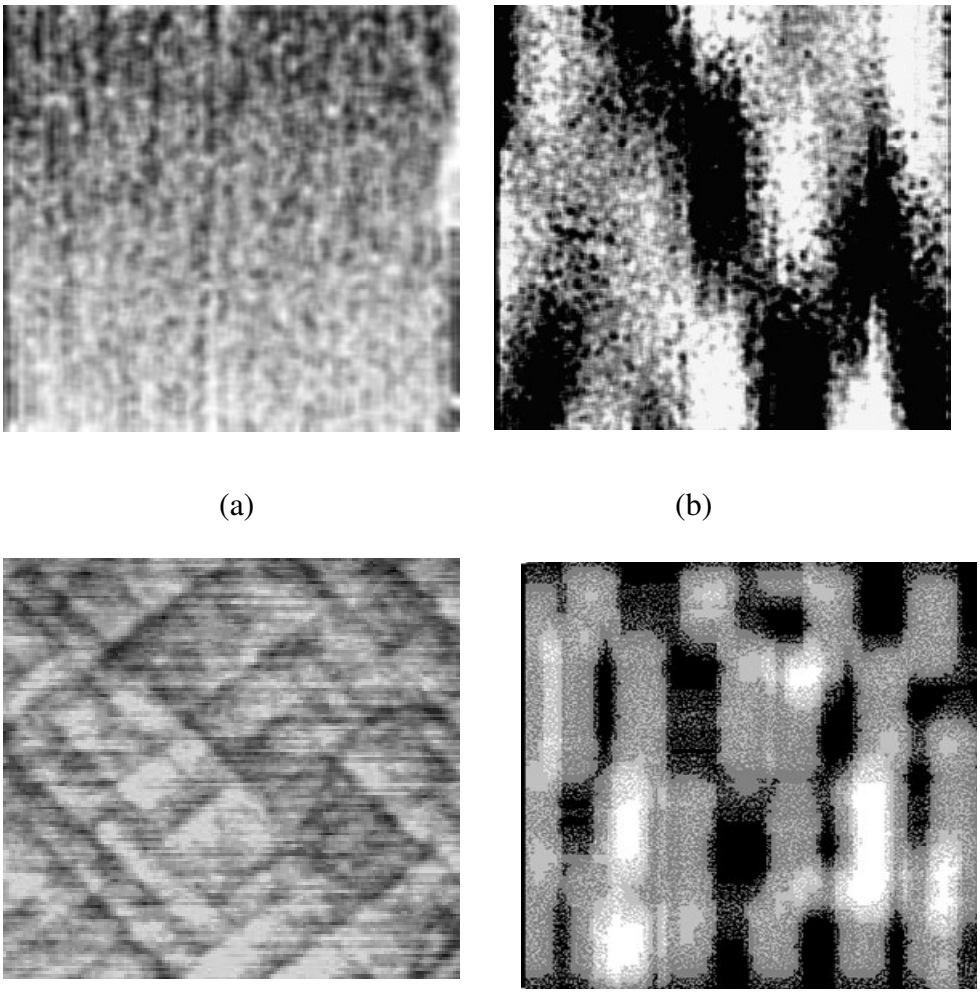

Figure 3.14. Simultaneously measured (a) topographical and SH near-field optical image (b) of a $PbZr_xTi_{1-x}O_3$ film. 1.5 μm by 1.5 μm images were obtained using P- polarized excitation light. Height variation within the topographical image is 30 nm. (c) 1.5 μm by 1.5 μm AFM image of the $PbZr_xTi_{1-x}O_3$ film. Height variation within the image is 5 nm. "Grid" structure corresponds to the boundaries of a-domains. (d) Calculated 1.5 μm by

1.5 μm image of SHG obtained assuming 100 nm spatial resolution of the microscope and experimentally measured (Fig.3.7) SH contrast between different poling directions

3.8 Strain Induced Near-field SHG in Thin $Ba_xSr_{1-x}TiO_3$ Films

SHG is a versatile tool in characterizing surfaces and thin films. The previous poling structures and in this section the strain induced effects are both objectives of study. We applied our near-field setup to visualize strain induced SHG in thin $Ba_xSr_{1-x}TiO_3$ (or BST) films grown on centrosymmetric $La_{0.5}Sr_{0.5}CoO_3$ (LSCO) substrates. At room temperature bulk BST has the centrosymmetric cubic m3m crystal symmetry, for which bulk SHG should be absent. The Curie temperature of BST for a phase transition into a ferroelectric state is about 240K. As has been shown recently [63], thin BST films may generate SH light because of strain due to the lattice mismatch. The nonlinear susceptibility values of these films measured in [63] are sufficiently different from those of $BaTiO_3$ and PZT: $\chi^{(2)}_{yyz} = \chi^{(2)}_{xxz} = \chi^{(2)}_{yzy} = \chi^{(2)}_{xzx} = 2.2\text{x}10^{-12}$ m/V, $\chi^{(2)}_{zyy} = \chi^{(2)}_{zxx} = -4.7\text{x}10^{-12}$ m/V, and $\chi^{(2)}_{zzz} = -11.0\text{x}10^{-12}$ m/V (where z is the strain direction). As a result, theoretical near-field SH signal polarization dependencies calculated for different strain directions and shown in Fig.3.15 differ substantially from the dependencies in Figs.3.7 and 3.9. For instance, curve (b) obtained for a strain direction perpendicular to the incidence plane of the fundamental light shows SH maxima for S-polarized excitation light. This behavior was never observed with $BaTiO_3$ and PZT samples, but it was routinely observed (see Fig.3.16(c)) in experiments conducted with BST films. Curve B in Fig.3.16(c) represents typical polarization behavior of the SH signal measured in different areas of the SH image in Fig.3.16 (b). After the sample had been rotated by 90^o,

the typical polarization behavior changed (curve A in Fig.3.16 (c)). Curves A and B look similar to theoretical curves in Fig.3.9 (a) and (b) respectively, which is another indication that our simple theoretical model provides an adequate description of near-field SH measurements.

Near-field SH signal observed from BST films was an order of magnitude weaker than the signal observed with PZT films, which required substantially longer image acquisition times. Nevertheless, SH imaging was possible and an example of such images obtained with a 0.4 μm thick BST film is presented in Fig.3.16 (a), (b). The SH image (Fig.3.16 (b)) is supposed to show the distribution of mechanical strain in the film. Features as small as 200 nm are clearly detectable in this image. They are probably caused by the terrace structure of the LSCO substrate, which was clearly visible and has the same spatial orientation as the orientation of stripes in the SH image.

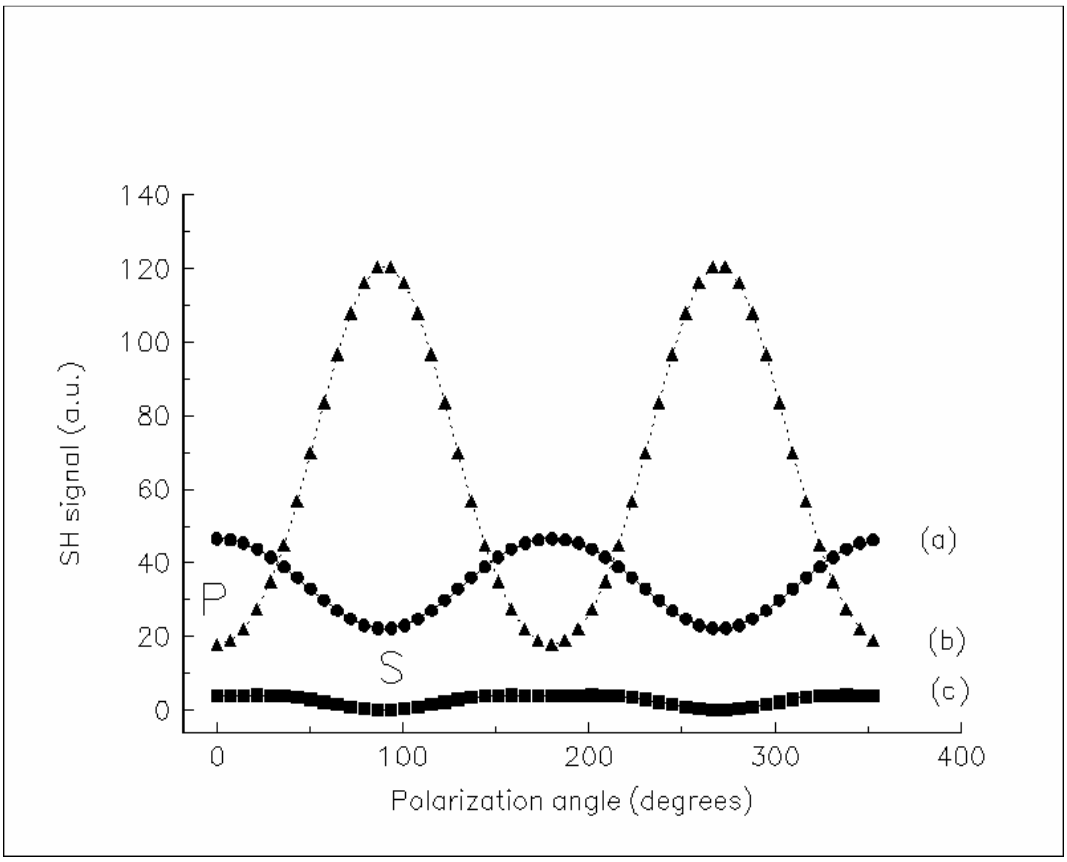

Figure 3.15 Theoretical near-field SH signal dependencies on the polarization angle of fundamental light obtained for strained BST films in the geometry similar to (a), (b) and (c) in Fig.3.6, where the arrows represent the direction of strain in the film. The field enhancement factor is assumed to be $\gamma = 4$ and the incidence angle $\alpha = 50^{o}$.

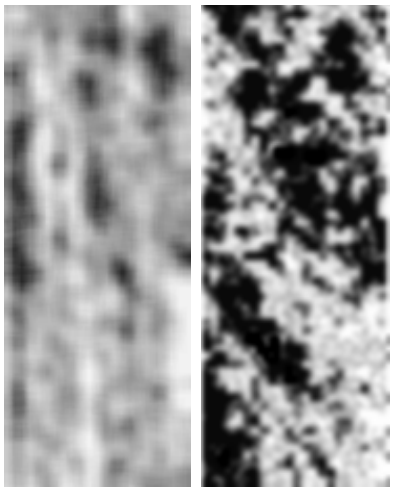

(a) (b)

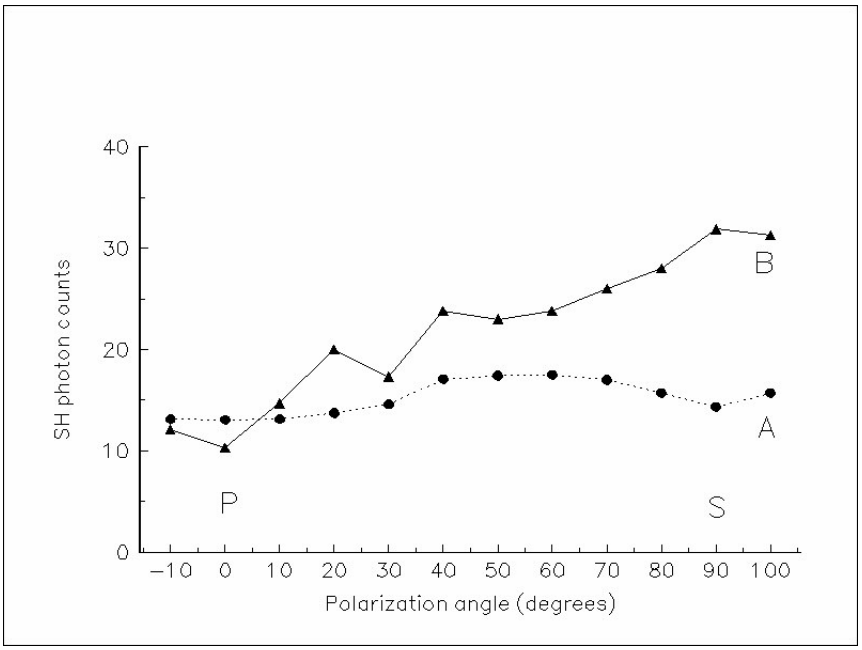

` (c)

Figure 3.16. Simultaneously measured (a) topographical and SH near-field optical image (b) of a BST film. 2.2 μm by 0.9 μm images were obtained using S- polarized excitation light. Height variation within the topographical image is 50 nm. (c) Typical near-field SH

signal dependencies on the polarization angle of the fundamental light measured over a thin BST film. Curve B was measured in the middle point of the SH image (b). Curve A was measured over the same area of the film after the sample had been rotated by 90^{o}.

3. 9 Conclusions for Current Imaging Work

In conclusion, an apertureless near-field optical technique for second harmonic imaging with optical resolution of the order of 80 nm has been developed. The information of topography and SH distribution on sample surface can be measured at the same time. Polarization properties of second harmonic generation from a poled single crystal of $BaTiO_3$ have been studied theoretically and experimentally in the near and far field zones for different orientations of optical axis orientations with respect to the tip and the incoming fundamental light. Good qualitative agreement between theory and experiment is demonstrated. The relation between local SH intensity and ferroelectric polarization direction has been investigated. Symmetry properties of the near-field SH signal allows us to recover local poling direction of individual ferroelectric domains in thin ferroelectric films with spatial resolution of the order of 80 nm. Imaging of different types of samples, including polydomain PZT, BST are studied and contrast mechanism can be explained using the conclusions from section 3.4.2.

Chapter 4: Nonlinear Optical Imaging of Polymer Thin Films Using Near-field Scanning Optical Microscopy

Organic nonlinear optical (NLO) polymers have attracted considerable interest for photonics applications due to their fast NLO response time, low cost, ease of fabrication, favorable material characteristics for high-speed modulation, and potentially large nonlinear second-order susceptibility, $\chi^{(2)}$ [64]. The active molecular groups responsible for the optical nonlinearity are chromophores.

Although these materials can easily be formed into thin films, the dipoles of the incorporated chromophores must not be macroscopically centrosymmetric in order to realize a nonzero $\chi^{(2)}$ [65]. Because the nonlinear susceptibility increases with increasing polar order, imaging techniques can be useful for evaluating the spatial morphology of chromophore order. These microscopy techniques involve linear or nonlinear optics in both the far-field and the near-field. In this chapter results of SH imaging of two types of NLO polymer thin films are presented. As an extension of our work on ferroelectric films, we studied polymer films with the same setup, with some modifications.

4.1 Brief Introduction of Polymers

Polymers are substances whose molecules are composed of a large number of repeating units (small molecules called monomers) that can be linked together to form long chains. A typical polymer may include tens of thousands of monomers. Because of their large size, polymers are classified as macromolecules. The concept of macromolecule was first developed by Hermann Staudinger during the 1920s [66], which

won him a Nobel Prize in Chemistry in 1953 for “his discoveries in the field of macromolecular chemistry”.

A polymer made entirely from molecules of one monomer is referred to as a “homopolymer”. Chains that contain two or more different repeating monomers are “copolymers”.

Configuration: The two types of polymer configurations are *cis* and *trans*. These structures can not be changed by physical means (e.g. rotation). The *cis* configuration arises when substituent groups are on the same side of a carbon-carbon double bond. *Trans* refers to the substituents on opposite sides of the double bond.

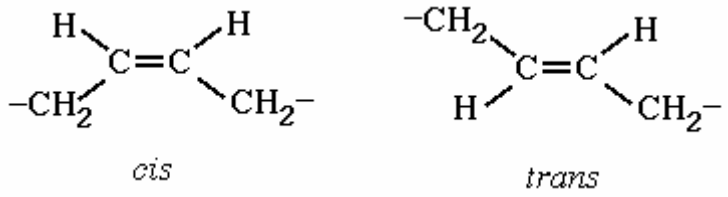

Figure 4.1 Illustration of *cis* and *trans* configurations

Conformation: If two atoms are joined by a single bond then rotation about that bond is possible since, unlike a double bond, it does not require breaking the bond. The ability of an atom to rotate this way relative to the atoms which it joins is known as an adjustment of the torsion angle. If the two atoms have other atoms or groups attached to them then configurations which vary in torsion angle are known as conformations. Since different conformations represent varying distances between the atoms or groups rotating about the bond, and these distances determine the amount and type of interaction between adjacent atoms or groups, different conformation may represent different potential energies of the

molecule. There are several possible generalized conformations: Anti (Trans), Eclipsed (Cis), and Gauche (+ or -).

Molecular Weight: The size of polymer molecules is usually expressed in terms of molecular weight, which is important in determine the polymer's properties. Since a polymeric material contains many chains with the same repeating units, but with different chain lengths, average molecular weight is generally adopted. In general, higher molecular weights lead to higher strength. But as polymer chains get bigger, their solutions, or melts, become more viscous and difficult to process.

Glass transition temperature: The temperature at which an amorphous polymer (or the amorphous regions in a partially crystalline polymer) changes from a hard and relatively brittle condition to a viscous or rubbery condition is called glass transition temperature (T_g). The higher the molecular weight is, the higher the glass transition temperature. The bulkier a segment of polymer is, the more energy it takes to move it, so its glass transition will be at a higher temperature. If there is the possibility of good intermolecular binding between the polymer chains, this effect will be more pronounced.

Synthetic polymers: People have taken advantage of the versatility of polymers for centuries in the form of oils, tars, resins, and gums. However, it was not until the early nineteenth century that the modern polymer industry began to develop. And the field of synthetic polymers is currently one of the fastest growing materials industries. The interest in engineering polymers is driven by their manufacturability, recyclability, mechanical properties, and lower cost as compared to many alloys and ceramics. Also the macromolecular structure of some synthetic polymers provides good biocompatibility and allows them to perform many biomimetic tasks that cannot be performed by other

synthetic materials, which include drug delivery, use as grafts for arteries and veins and use in artificial tendons, ligaments and joints.

There are two basic chemical processes for the creation of synthetic polymers from small molecules (1) condensation, or step-growth polymerization, and (2) addition, or chain-growth polymerization.

4.2 Nonlinear Optical Study of SPECH APD Polymer Films

4.2.1 SPECH/PAA APD Film

Alternating polyelectrolyte deposition (APD) is a technique for fabricating multilayer thin films at room temperature [67]. The substrate is alternately dipped in two different aqueous solutions—one containing a polycation and the other a polyanion, as shown in Fig. 4.2.

It has been demonstrated that the APD process can be used to make multilayer second-order nonlinear optical polymer films by incorporating chromophores in the polycation and/or polyanion [68, 69], In addition, an encouraging discovery is that these films exhibit a high degree of thermal robustness [70]. Chromophores are the origin of nonlinearity in NLO polymers. In order for the polymeric materials to exhibit bulk second-order optical nonlinearities, the non-centrosymmetric nonlinear chromophores must be arranged in the material in such a manner that the bulk material also does not have an effective center of symmetry. APD provides the possibility to align chromophores.

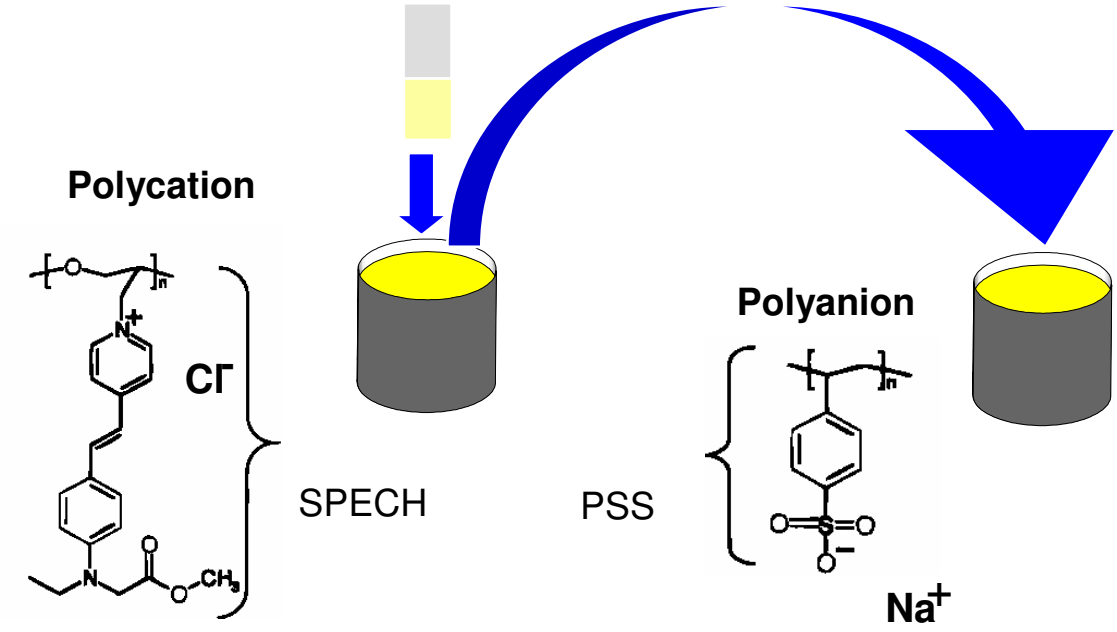

Figure 4.2 Fabrication of SPECH APD films

The side-chain cationic polymer used in the fabrication of the thin APD films investigated here contained the NLO chromophore responsible for the second-order NLO properties. The structure of this polymer, stilbazolium-substituted polyepichlorohydrin (SPECH), is shown in Figure 4.3 and its synthesis and fabrication into thin films is discussed elsewhere [71]. In the fabrication process, layers of this polymer were alternated with a polyacrylic acid (PAA) polyanion. This film was fabricated by M. J. Roberts at the China Lake Naval Weapons Center.

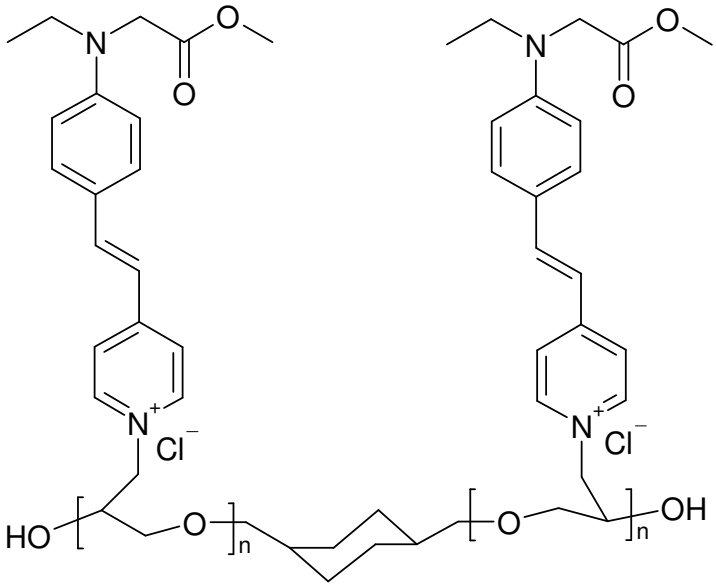

Figure 4.3 Structure of SPECH polycation

4.2.2 Far-field Optical Second Harmonic Measurements

Because the near-field SHG signal from the polymer film was low, far-field experiments were first carried out to find the optimum condition for near-field measurement. SHG from the polymer film was measured as a function of angle of incidence and polarization of the fundamental beam at the far field for this purpose. The experimental setup is illustrated in Fig. 4.4.

(a) SHG dependence on incident light polarization

Ti:sapphire laser amplifier was used to generate SH in the polymer in transmission mode. Since the polymer will be burnt away at high laser power level, the average power was kept well below 100mW for the far field measurement. A half-wavelength plate was used to rotate the polarization of incident light. SH photons were

collected by a photomultiplier after two blue filters in series and measured by a photon counter.

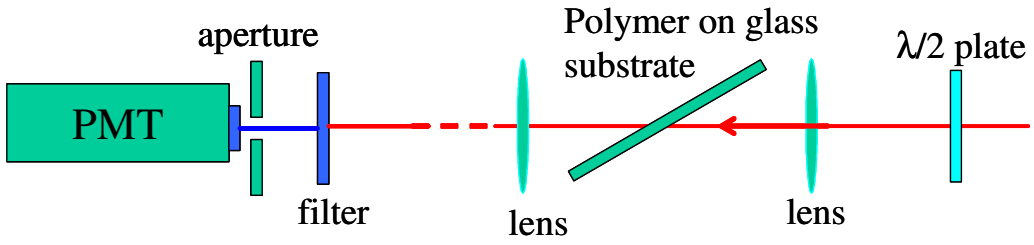

Figure 4.4 Experimental setup for far-field SHG measurement

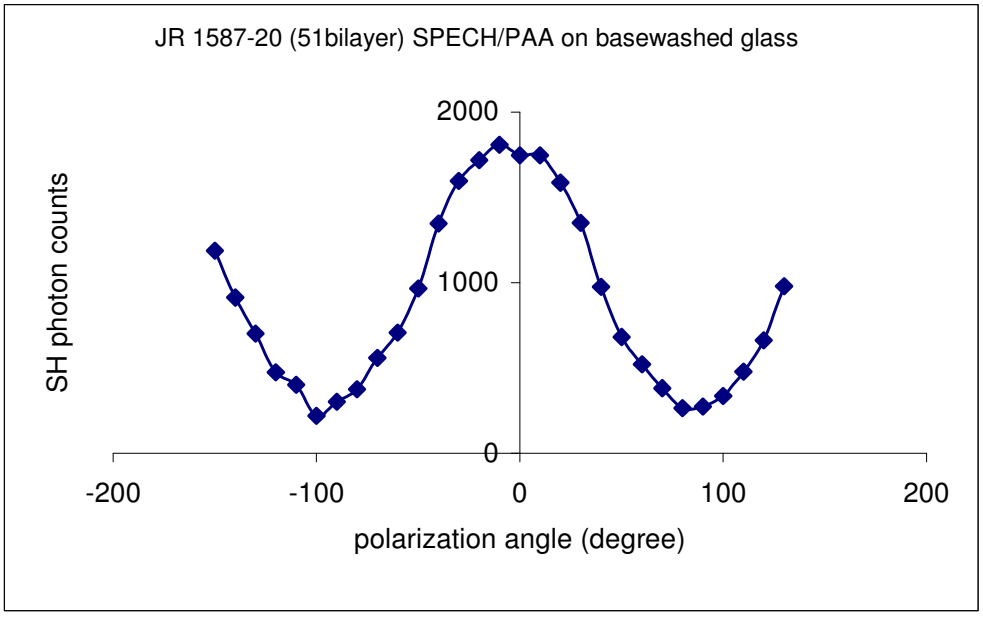

Figure 4.5 SH signal dependence on angle of incidence. 0^{o} corresponds to p-polarized fundamental light.

With a fixed sample, it was known that the polarization of incident light has a determining effect on the SH signal strength. As shown in Fig. 4.5, the maximum occurs for P-polarized incident light while for S-polarized light, the SH counts is minimum. The contrast ratio is close to 10:1.

(b) SHG Dependence on Incidence Angle

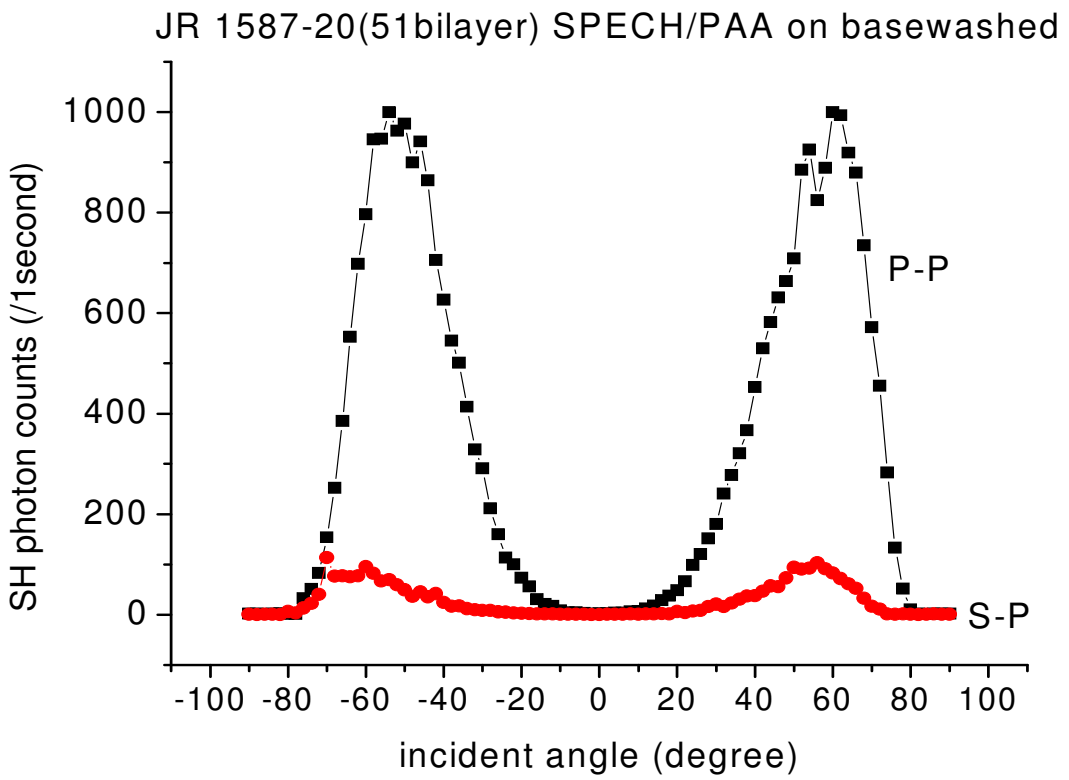

Figure 4.6 SH signal from SPECH/PAA dependence on incidence angle

The measurement of second harmonic power generated by a slab of material as a function of the angle of rotation (i.e., as a function of the angle of the incidence angle of

the fundamental beam), and comparison of this measurement to that of a standard, well characterized material to obtain the effective nonlinear coefficient (d_{eff}) of the sample is called the *Maker Fringe Method* [12]. Here the rotation of the incidence angle mainly serves as a guide to find SHG maxima. The result is shown in Fig. 4.6. Both P- and S-illumination result in SH maxima at a 60 degree of incidence angle.

This provides guidance for the setup of near-field experiments. It was observed that there was no detectable SH signal in reflection and the transmitted SH signal at normal incidence was zero. The above observations are typical of ∞mm point group structure, which poled polymers process.

These observations led us to the experimental configuration shown in Figure 4.7 (i.e., the sample film was oriented at 60° to the fundamental beam, while the fiber tip was oriented in the forward direction).

4.2.3 Near-field SHG Investigation of SPECH/PAA Films

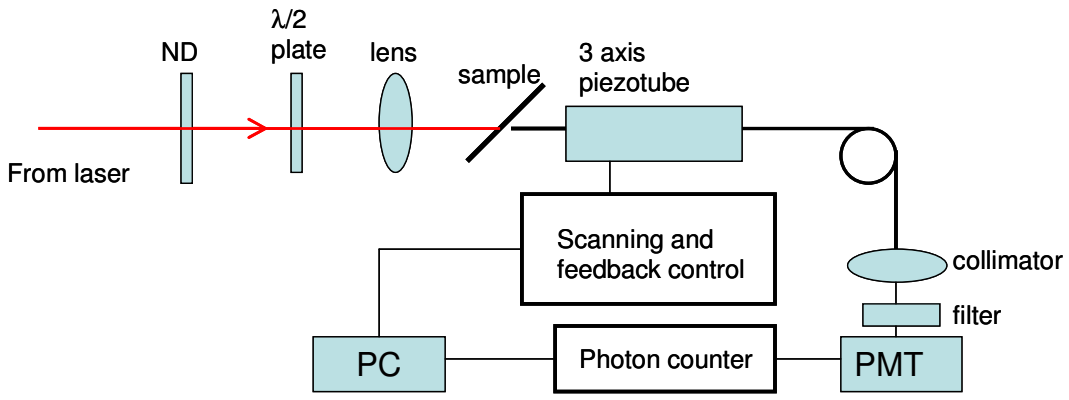

Figure 4.7 Near-field SH microscopy set-up for polymer imaging.

Illumination (spot diameter on the order of 50 μm) was provided by a Ti:sapphire laser system consisting of an oscillator and a regenerative amplifier operating at 810 *nm* (repetition rate up to 250 *k*Hz, 100-fs pulse duration, and up to 10 μJ pulse energy). An f = 25 cm lens was used to weakly focus the laser beam onto the sample. The illumination area was ~5000 μm^2. The power density was about 2 x 10^{11} W/cm^2, corresponding to an average power of 100 mW from the laser. To avoid sample ablation, the average incident power was kept under 100 mW. A neutral density filter was used to reduce the laser power. An uncoated, adiabatically tapered fiber tip with an end diameter of about 50 nm was used to collect the local SH signal at the other side of the sample, where the polymer is deposited. The tip was scanned over the sample surface with a constant tip-surface distance of 5-10 nanometers using shear force feedback control. This allows surface topography images to be obtained while simultaneously recording the SH near-field images using photoncounting.

In the far-field measurements the fiber tip was replaced by a collecting lens. For the near- field measurement, the SHG yield from SPECH/PAA was fairly low, only 1/6,000 of that from an X-cut quartz reference, as shown in Table 4.1. It amounted to only a few photo-electrons per second in the detection system even when the illuminating fundamental light was up to 100 mW, which is the maximum average power one should use to avoid damage to the film. As mentioned above, this average power corresponds to a high power density per pulse of 2 x 10^{11} W/cm^2, but the energy per pulse is only ~1 μJ due to the short 100 fs pulse duration. This short pulse duration typically results in higher damage thresholds than experienced, for example, by high power excimer laser systems at shorter wavelengths. Although metal coated tip will give better resolution, it collected

too few SH photons from the polymer to be of practical use (Table 4.1). Because the fundamental light was focused near the tip in order to have a reasonable count, it affected the shear force feedback control system. As a result, when the topography image was scanned the fundamental beam had to be turned off.

	Polymer	Quartz
Far field SHG	~500-600	~3,000,000
near field with uncoated tip	~5	~30,000
near field with coated tip	0	~5,000

Table 4.1 Comparison of SH generation in polymer and quartz in far-field and near field. The photon counter counting time was 0.5 second.

Figure 4.8 shows images from four consecutive scans. The reproducibility of the topography image was verified prior to scanning. Because of the large angle between tip and sample, we could only scan a 1 μm x 0.8 μm area, limited by the range of the piezotube along the tip direction. The figure reveals that at an average power of 100 mW, corresponding to a peak power density of 2 x 10^{11} W/cm^2, the fundamental beam alters the landscape of the film surface. The SHG is clearly reduced after the first scan. A trench was created after two consecutive scans. It is important to note that it took about 2 hours to obtain one SH image. The observation that this long exposure time at high power altered the topography is consistent with the fact that the SH signal deviates from quadratic dependence on the fundamental power at about 50mW, corresponding to a peak power density of 10^{11} W/cm^2.

The reduction of SH signal in the second SH image may also be related to the change in molecular alignment and/or orientation due to laser irradiation. These images demonstrate clearly that the near-field SH images of the self-assembled film are uncorrelated with the topographical images. A similar result was found in [72] in the case of Langmuir-Blodgett films.

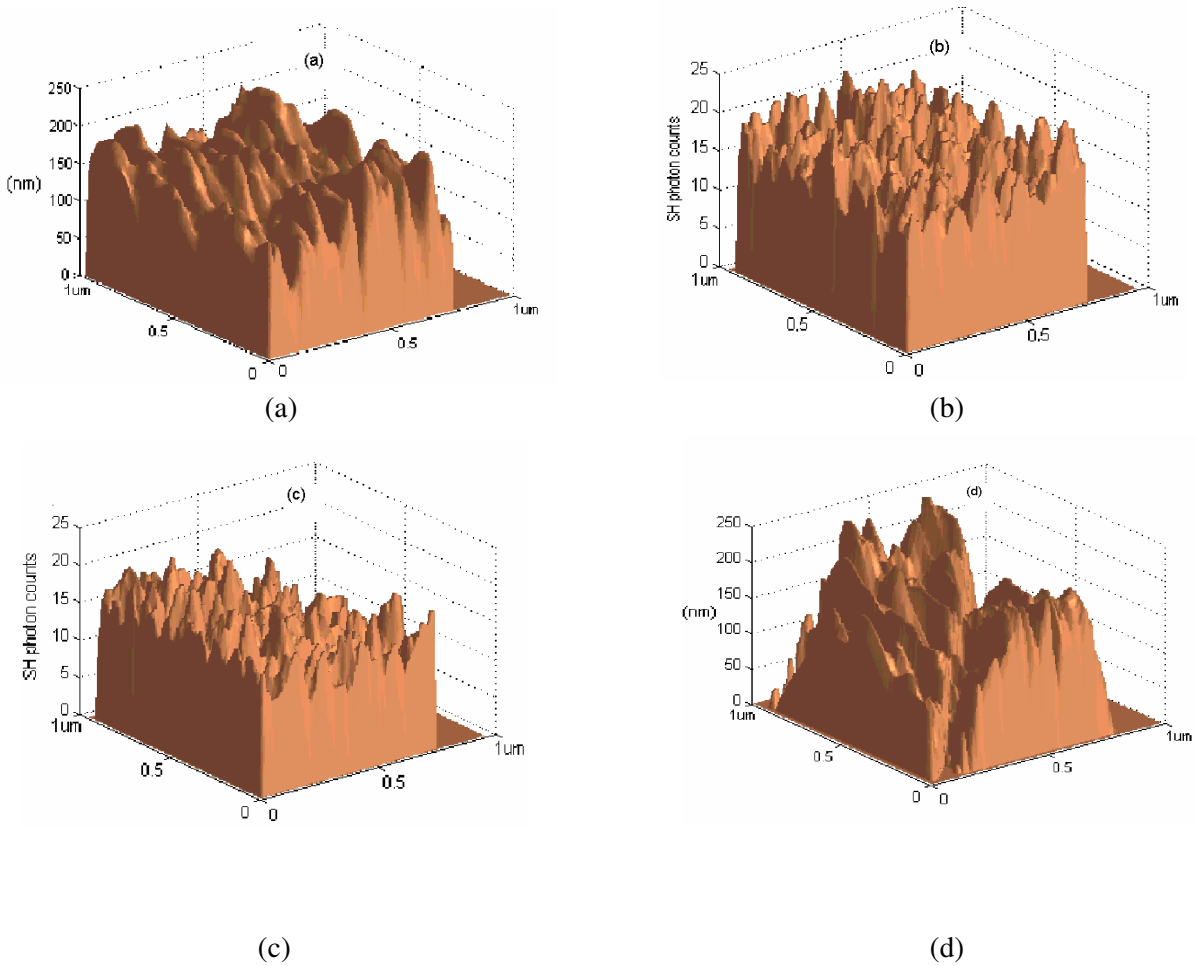

(a) (b)

(c) (d)

Figure 4.8 (a) topography before illumination, (b) near-field SH images, (c) second near-field SH image, scanned right after the first SH image and (d) topography after illumination of the SPECH/PAA film

4.3 Nonlinear Optical Study of Poled C2CMA Polymer Film

Electric-field poling is another well known method to align chromophores in NLO polymers thus producing polar ordering of molecules and enabling second-order nonlinearity in polymers. For spin-coated polymer films, the polar molecules tend to arrange in pairs with their dipole moments antiparallel to each other to minimize the free energy. This type of centrosymmetric arrangement averages out the second-order NLO responses to zero at macroscopic scales. The poled polymer film we used was a coumaromethacrylate copolymer (C2CMA) synthesized by R. A. Henry, J. Hoover, and G. A. Lindsay at the Naval Weapons Center at China Lake, California [73]. With this kind of film there was sufficient SHG to go directly to the near-field characterization.

4.3.1 Static electric field poling of polymers

Dipolar molecules like chromophores can be oriented by applying a static external field. The orientation rate depends on the poling field and on the poling temperature. Figure 4.9 shows a schematic polymer poling system.

Generally there are two ways of static poling:

(i) Contact (electrode) poling

(ii) Corona poling.

In the first case in-plane poling can be obtained if both electrodes are deposited on the substrate. And it is also possible to get perpendicular poling when polymer is sandwiched between two electrodes. The main problem with this technique is the dielectric breakdown, occurring at relatively low fields due either to “point effect” or breakdown of the surrounding air.

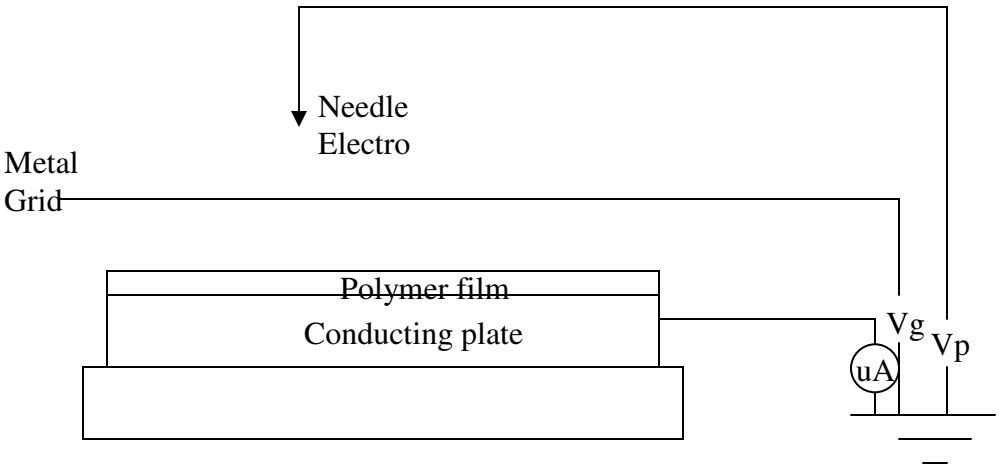

Figure 4.9 Schematic representation of a corona poling apparatus. Charges generated by an electric discharge on a metallic tip are deposited on the thin film surface and create a high electric field in the polymer film.

Corona poling [74] is implemented by applying a high voltage between a needle and a conducting bottom electrode, as in Fig. 4.9. Ionized charges are deposited on the thin film surface and create a high electric field inside, usually higher than case (i).

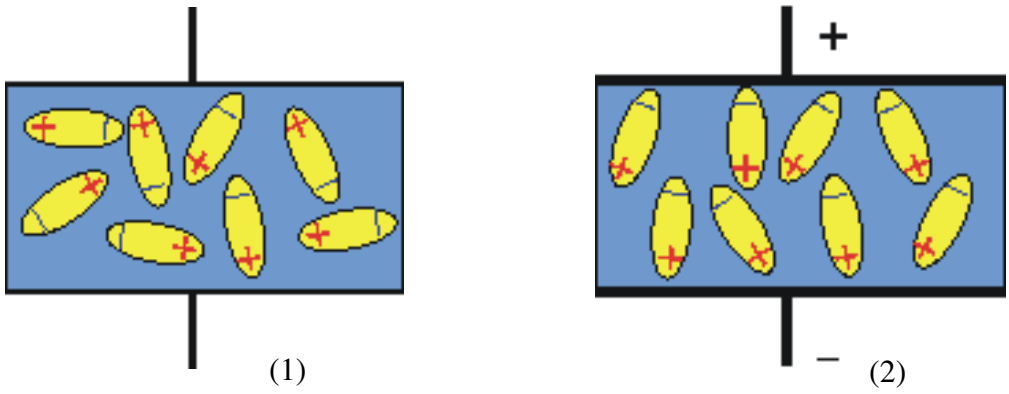

Figure 4.10 illustration of the poling process: (1) Before poling, chromophores randomly orientated; (2) Under poling, chromophores are mostly aligned along the electric field.

The poling process can be summarized as the following steps:

1) heating the sample to above glass temperature;

2) apply voltage to the sample;

3) after most of the chromophores are aligned, which can be monitored by SHG, cool down the sample;

4) turn off the electric voltage.

Fig 4.10 is an illustration of the chromophore orientation during the poling process.

4.3.2 Near-field SH Imaging of Poled Polymers

The poled C2CMA polymer was imaged in the near field. Both transmission and reflection mode images were taken. The same 800 nm laser was used to illuminate the sample, and SH was generated at 400 nm. But in this particular polymer sample, the Coumarin absorbs the SH strongly and the 400 nm SH in turn generates broad fluorescence in the polymer film. We used different interference filters with center wavelengths at 450 nm and 400 nm to check the fluorescence. With 450 nm interference filter, around 10 counts/0.5 sec is obtained, while with 400 nm interference filter < 1 counts/0.5 sec. With the use of a short pass blue glass filter, ~100 counts/0.5 sec can be obtained in transmission mode, which is much larger than that from the previous APD film. Images of topography and SH distribution are shown in Figure 4.11 (a). Because of the nature of fluorescence, there was sufficient intensity in reflection mode to collect near-field point-by-point pixel images shown in Figure 4.11 (b). Because of the higher nonlinearity in C2CMA, lower fundamental light power was needed, and there were no signs of damage in the film during the experiments.

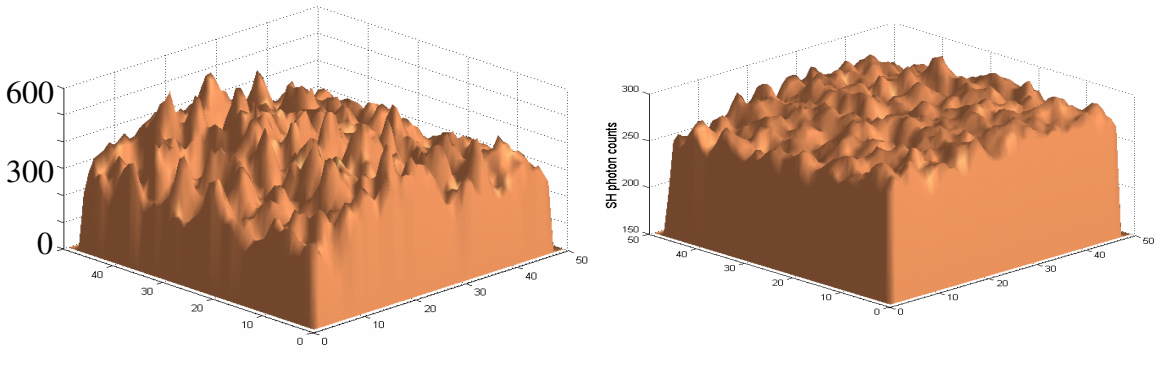

Topography SH mapping

Transmission mode: 1μm x 1μm image with 6mW average laser power at 800nm, equivalent to 12 GW/cm^2 peak pulse power

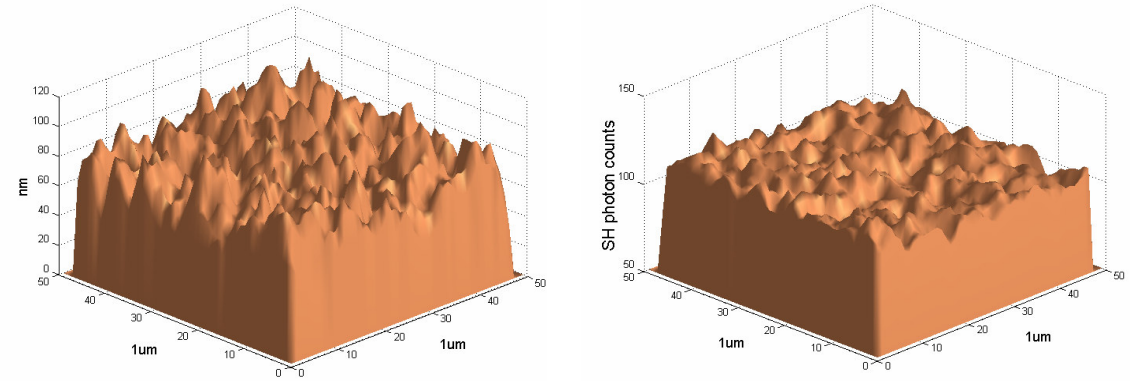

Topography SH mapping

(b)

Reflection mode: 1μm x 1μm images, 3mW fundamental light

Figure 4.11 (a) Topography and transmission near-field SH image of C2CMA

(b) Topography and reflection near-field SH image of C2CMA

4.4 Summary of NLO Polymers SH Imaging

SHG near-field microscopy (NSOM) was used to investigate a bi-layered SPECH/PAA film prepared by APD and poled C2CMA films. Both far-field SHG measurements and near-field SHG measurements were used to characterize the films using a femtosecond laser at a fundamental wavelength of 800nm. The SH near-field image was collected on a 1 μm^2 area of the film.

The SHG efficiency of SPECH/PAA films is low, especially when collecting SH signal using a fiber probe. The optical signal from C2CMA is higher, which actually comes from fluorescence excited by the SH photons. For both polymers, SH images showed no special features, and could not be correlated to the topography. The variations in both images were on the order of quantum noises of the optical detection system. Hence they may not carry any information on the polymer structures.

Although the use of gated photon counters greatly increased the SNR of the detection system, the discrete and probabilistic nature of the optical signal makes the detection suffer from *quantum noise*. Quantum noise is proportional to the square root of the optical intensity, and in many cases it represents the fundamental limit of the achievable SNR of an optical system. Examples of quantum noise are photon noise in an optical signal and shot noise in an electrical conductor or semiconductor. We can see that the variations in SH images is on the order of the square root of the maximum signal, which indicates that the contrast in those SH images may not relate to $\chi^{(2)}$ distributions. The limit to the SNR set by quantum noise can be minimized by having stronger signals. And if the features in the polymer films are generating more contrast, the quantum noise will be suppressed relatively.

Chapter 5: Transient Photoconductive Effect in Conjugated Polymer Thin-Films

This chapter discusses transient electric pulses and reflectivity measurements in conjugated polymers. Electric pulses generated from photoconductive switches fabricated on polymers are found to have extremely short temporal duration. Both 20GHz sampling oscilloscope and pump probe methods are employed to measure this pulse width and the corresponding carrier mobility of the polymer. A new scheme of pump probe experiment using only one photoconductive switch was implemented. The polymers under investigation are BAMH PPV and MEH PPV.

5.1 Brief Introduction to Conjugated Polymers

Conducting polymers are the most recent generation of polymers. The first polymer capable of conducting electricity - polyacetylene - was reportedly prepared by accident by Shirakawa [22]. A subsequent discovery by Heeger and MacDiarmid [75] showed that the polymer would undergo an increase in conductivity up to 10^{12} of magnitude by oxidative doping. The following research showed that by doping control, these polymers can change over the full range from insulator to metal. This created a new field between chemistry and condensed-matter physics. From the day of its invention, it attracted the attention of not only chemists, but also the electronic researcher for its potential to replace or complement existing inorganic semiconductors.

Before the discovery of conjugated polymers, polymers under study were mostly saturated polymers (all of the four valence electrons of carbon are used up in covalent

bonds) and therefore considered as insulators. In conjugated polymers, the electronics configuration are different.

π-bond: Conjugated polymers have a framework of alternating single and double carbon–carbon (sometimes carbon–nitrogen) bonds. Single bonds are referred to as σ-bonds, and double bonds contain a σ-bond and a π-bond. All conjugated polymers have a σ-bond backbone of overlapping sp^2 hybrid orbitals. The remaining out-of-plane p_z orbitals on the carbon (or nitrogen) atoms overlap with neighboring p_z orbitals to form π-bonds. Although the chemical structures of these materials are represented by alternating single and double bonds, in reality, the electrons that constitute the π-bonds are delocalized over the entire molecule, providing the "highway" for charge mobility along the polymer chain backbone. This feature results in materials with directional conductivity, strongest along the axis of the chain [76].

In some conjugated polymers such as polyacetylene (PA) and PAn, delocalization results in a single (degenerate) ground state, whereas in other polymers the alternating single and double bonds lead to electronic structures of varying energy levels.

Doping: The behavior of conjugated polymers is dramatically altered with chemical doping. As seen from above, in a conjugated system the electrons are loosely bound, electron flow is possible along the backbones of molecules. However as the polymers are covalently bonded the material needs to be doped for electron flow to occur. Doping is either the addition of electrons (reduction reaction) or the removal of electrons (oxidation reaction) from the polymer. Once doped, the electrons in the pi-bonds are able to "jump" around the polymer chain. By doping, the conductivity of the polymer increases from 10^{-3} S m^{-1} to 3000 S m^{-1}.

The conductivity of conducting polymers can range from values for insulators to values for conductors, which is realized either by chemical doping or by electrochemical doping. Doped conjugated polymers can be good conductors for the following reasons:

1. Doping introduces carriers into the electronic structure. Since every repeat unit is a potential reduction-oxidation (redox) site, conjugated polymers can be doped *n* type (reduced) or *p* type (oxidized) to a relatively high density of charge carriers [77].
2. The attraction of an electron in one repeat unit to the nuclei in the neighboring units leads to carrier delocalization along the polymer chain and to charge-carrier mobility, which is extended into three dimensions through interchain electron transfer.

Disorder, however, limits the carrier mobility and, in the metallic state, limits the electrical conductivity. Nowadays, researchers are trying to improve the polymer structure order to gain higher mobility.

Varieties: The essential structural characteristic of all conjugated polymers is their quasi-infinite π system extending over a large number of recurring monomer units. The simplest possible form is of course the archetype polyacetylene $(CH)_x$ shown in Figure 5.1. While polyacetylene itself is too unstable to be of any practical value, its structure constitutes the core of all conjugated polymers. Owing to its structural and electronic simplicity, polyacetylene is well suited to *ab initio* and semi-empirical calculations and has therefore played a critical role in the elucidation of the theoretical aspects of conducting polymers.

(a) (b)

Figure 5.1 Conjugated polymer structure: (a) trans- and (b) cis-polyacetylene

Following the synthesis and doping of polyacetylene, the opportunity to synthesize new conducting polymers with improved properties began to draw the attention of chemists in the 1980s. Polyaniline (PANI) was considered to be the first stable conducting polymer that can be processed in the metallic form [78]. Poly(phenylene vinylene), PPV, is one of a few of conducting polymers that has been successfully processed in film form to yield oriented samples with high levels of crystallinity. Thus the structure of PPV has also been extensively studied [79, 80].

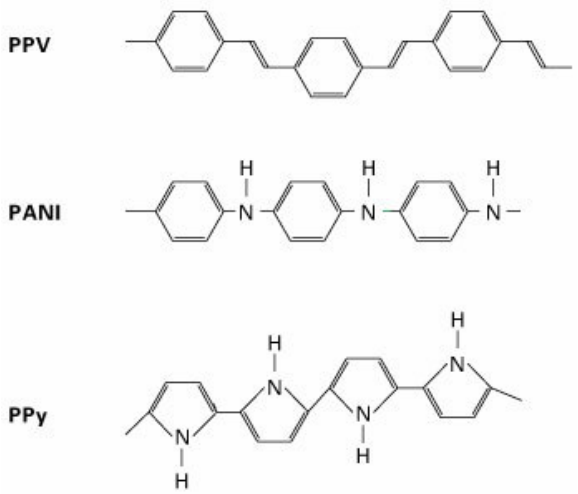

Figure 5.2. Structural formulas of some commonly used conjugated polymers, polyphenylene-vinylene or PPV, polyaniline or PANI and polypyrrole or PPy.

The polymers form long chains consisting of thousands of units (precursors) linked one after the other. A conjugated structure is characteristic of all semiconducting polymers. This means that single and double atomic bonds occur alternately throughout the entire chain.

Band structure: Electronically conducting polymers are extensively conjugated molecules, and it is believed that they possess a spatially delocalized band-like electronic structure [81, 82]. These bands stem from the splitting of interacting molecular orbitals of the constituent monomer units in a manner reminiscent of the band structure of solid-state semiconductors (Fig. 5.3).

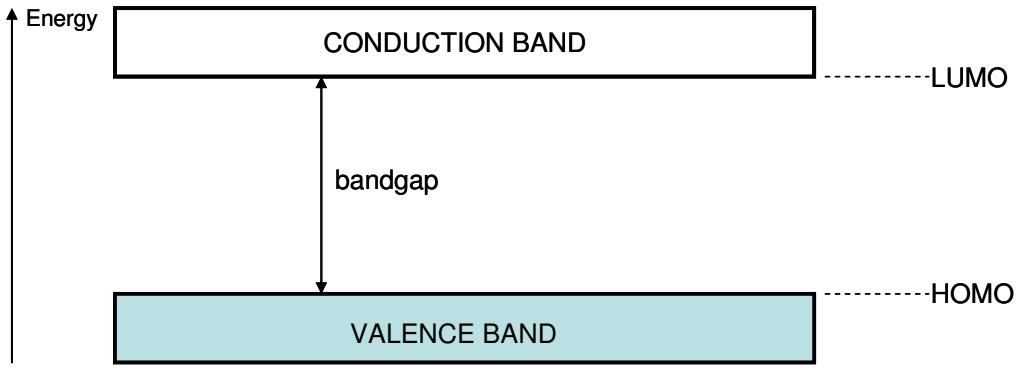

Figure 5.3 Band structure in an electronically conducting polymer

The conductivity σ of a conducting polymer is related to the number of charge carriers n and their mobility μ:

$$\sigma \propto n\mu$$

Because the band gap of conjugated polymers is usually fairly large, n is very small under ambient conditions. Consequently, conjugated polymers are insulators in their neutral

state and no *intrinsically* conducting organic polymer is known at this time. A polymer can be made conductive by oxidation (p-doping) and/or, less frequently, reduction (n-doping) of the polymer either by chemical or electrochemical means, generating the mobile charge carriers described earlier.

Applications: Conjugated polymers combines the optoelectronic properties of semiconductors with the mechanical properties and processing advantages of plastics [83]. The possibility to be processed in solution form under room temperature into large-area, optical quality thin films makes conjugated polymers useful in novel devices. And the ease of processing compared to inorganic semiconductors greatly cuts the cost in applications.

Photonic devices can be classified into three categories: light sources (light-emitting diodes, diode lasers, etc), photo detectors (photoconductors, photodiodes, etc) and energy conversion devices (photovoltaic cells). Up to now, most of the photonic phenomena known in conventional inorganic semiconductors have been observed in semiconducting polymers [84]. Devices fabricated using conjugated polymers such as light-emitting-diodes (LEDs) [85], photodetectors [86], photovoltaic cells [87], field-effect-transistors (FETs) [88], and the completely new application of flexible displays . These polymer-based devices have reached performance levels comparable to or even better than their inorganic counterparts.

Issues of concern: Despite the current success in synthesis of various conjugated polymers with desired electronic and optical properties and numerous applications of conjugated polymer in photonic devices, some fundamental physics underlying the construction and optimization of practical devices based on polymers still remains

controversial or poorly understood. The debate over carrier photoexcitation in conjugated polymers can be succinctly stated as: Are photocarriers created directly via interband photoexcitation or as a result of exciton dissociation [89] [90]. The interband picture uses the band structure similar to inorganic semiconductors, assuming photoexcitations directly generate free charges, which may relax to lower energy levels. While in the exciton model, molecular excitons are formed upon photoexcitation, and a secondary process such as exciton-exciton annihilation [91] or hot exciton dissociation [92] generate free charges [93]. Considerable effort has been devoted to unraveling the hidden mechanisms of photoexcitation in polymers. The questions that are of concern can be summarized in three generic aspects [26]: carrier photogeneration, carrier mobility and carrier recombination process. Heegers group has pioneered the study of photophysics of conjugated polymers. They started by measuring the transient photocurrent and photoluminescence in PPV samples with matched microstripline configurations excited by ultrashort laser pulses and studied the processes with subnano second to picosecond resolution [26]. Some significant experimental results are obtained by measuring the sub-nano to picosecond photoconductivity: (1) the fast transient photocurrent is independent of temperature, (2) the fast transient photocurrent is linear to the external field, (3) the fast transient photocurrent is linear to the photo excitation intensity, and (4) displacement current contribution can be ignored. From these facts, Heeger's group concluded that the carrier generation in conjugated polymers is a first-order process and can't be attributed to excitons [26]. The above conclusions was based on experiments with a time resolution of 50ps, though it revealed the transient photoconductivity of conjugated polymers and proved the existence of free carriers after photoexcitation, the

lack of time resolution prohibit the disclosure of when the carrier is generated: whether they are immediately following the laser pulse or after exciton annihilation is still unsolved. To solve this puzzle, photo current measurement with a much better time resolution is required. In this chapter we used both a sampling oscilloscope with 20ps time resolution and photoconductive sampling with sub 2 ps resolution to take measurements on PPV devices.

Another unaddressed issue in close relation to the photophysics of conjugated polymers is the magnitude of the mobility [93]. Mobility is an important concept in understanding and improving the performance of many practical devices such as PV, LED and transistors. Different approaches exist in measuring the steady state and transient mobility of polymers [94] [95]. Heeger's group observed that transient mobility was much larger than the steady state mobility in some early studies on the photoconductivity [26]. To have an accurate measurement of the transient mobility, higher time resolution schemes are needed. With a reliable assumption of the photocarrier concentration in the polymer, and based on our measurement of the photoconductivity of the polymers, we calculated the transient mobility in PPV polymers. The results were close to that obtained by researchers in Netherlands who used THz to indirectly measure the transient process in conjugated polymers [93].

Samples under study In this chapter, two conjugated polymers are investigated, which are poly(2,5-bis[N-methyl-N-hexyl amino] phenylene vinylene) (BAMHPPV) and poly[2-methoxy-5-(28-ethylhexyloxy)-1,4-phenylenevinylene] (MEHPPV).

BAMHPPV was synthesized at China Lake Naval Weapons Center and the monomers are shown in Fig. 5.4 (a). Most of the conjugated polymers have little or no absorption at

longer wavelength or infrared. Hence when studying the optical response of these polymers, the UV or lower part of the visible spectrum needs to be employed.

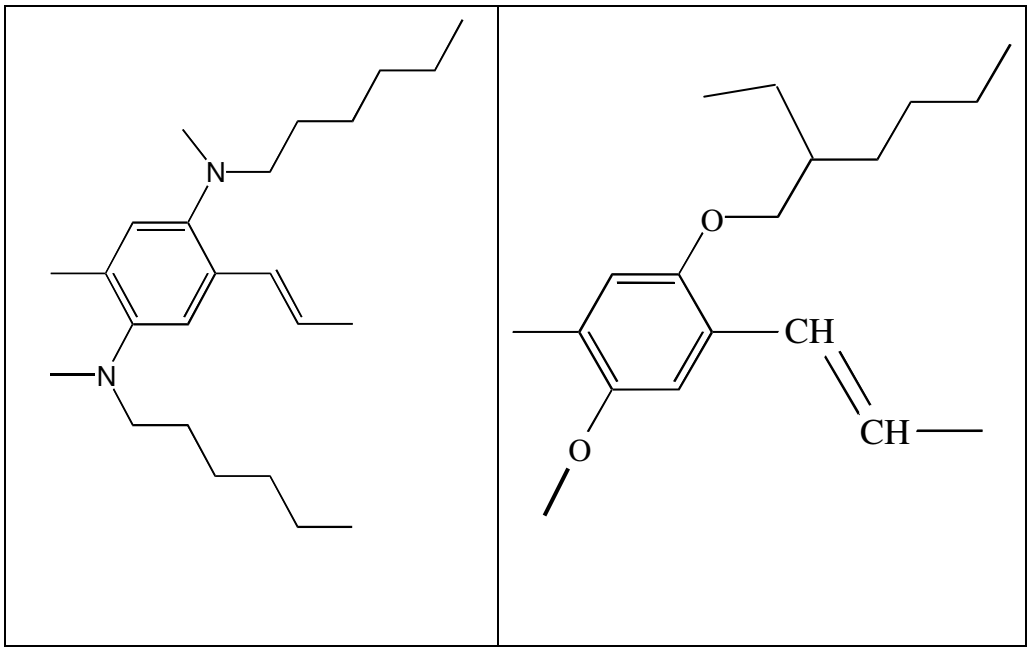

(a) **(b)**

Figure 5.4 Monomers of conjugated polymers: (a) BAMHPPV and (b) MEHPPV

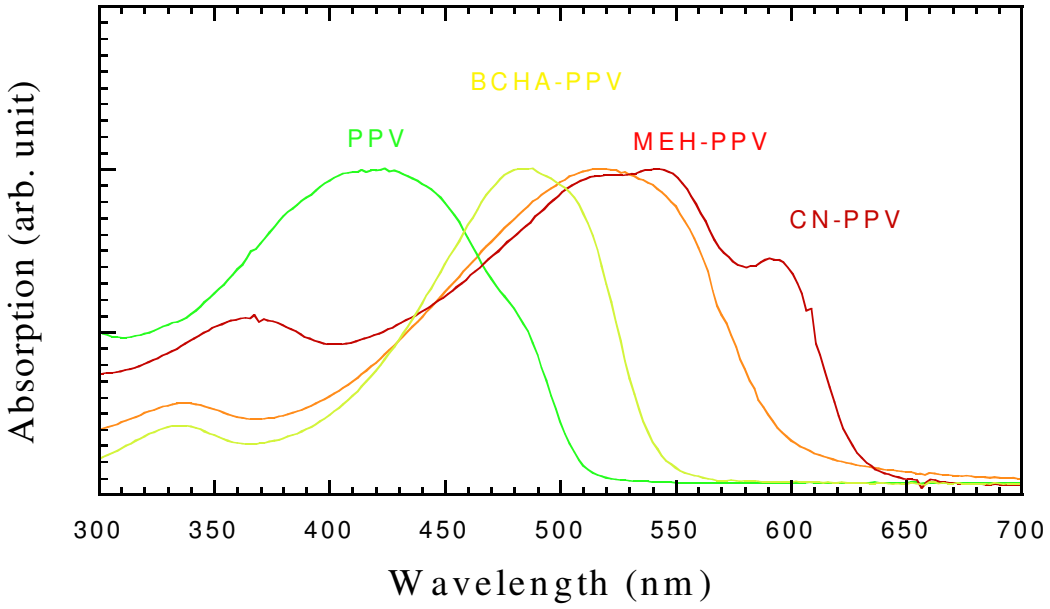

Figure 5.5 Optical absorption spectrum of some conducting polymers

5.2 Transient Photoconductance Measurement Setup Description

To understand the photoexcitation and charge generation process, a fast time resolution in the pico- or sub-picosecond scale is required. It is well known that when a laser pulse illuminates a biased gap on semiconductors, an electrical pulse will be generated. This is also observed in the conjugated polymers and hence provides a method to probe the carrier information.

5.2.1 Photoconductive Switch and Picosecond Electrical Pulse Generation

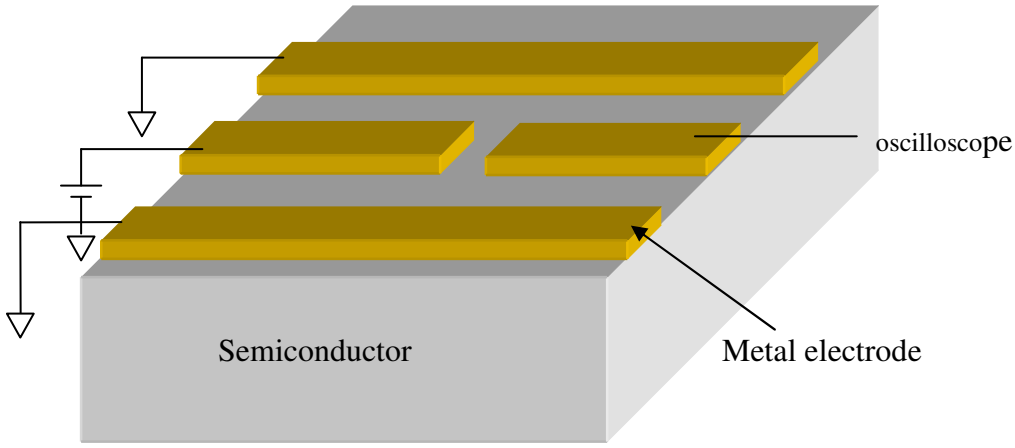

Figure 5.6 Photoconductive switch lay out

Photoconductive switches for high speed optoelectronics applications had been developed by Lee [96] and Auston [97] as early as the 1970s, and currently are the basis for picosecond electronics. Simply speaking, a photoconductive switch is a device which converts an optical pulse to an electrical pulse via photoconductivity. Two factors determine the time resolution of a photoconductive switch: the laser source and the carrier life time of the substrate. Nowadays subpicosecond electrical pulses are mostly achieved by using a mode locked Ti:sapphire laser as optical source and low temperature grown GaAs (LT GaAs) or ion-irradiated Silicon-on-Sapphire (SOS) as the substrate material.

Photoconductive switches are formed by depositing metallic electrodes on photoconducting media (As in Fig. 5.6, which is in the form of a coplanar transmission line). A sub-picosecond light pulse (whose frequency spectrum falls in the absorption band of the photoconductor) is focused on the active region of the photoconductor,

which consists of a small gap in the center line (or interdigitated gap structure). The laser excitation leads to a reduction of the gap resistance and a transient change of the voltage across the gap thus forming a photovoltage pulse on the transmission line. Upon illumination, photons are absorbed by photoconductors and electron-hole pairs are generated subsequently. This is intrinsically a fast process, which in principle could be as short as 10^{-15} s or one optical cycle [98], so the temporal response of the switch is mainly determined by the carrier life time, the transit time of carriers traveling across the gap and the time constant for discharging and/or recharging of the gap.

As mentioned in section 5.1, polymers as photoconductive media were studied extensively in the subnanosecond time regime [26]. Unlike inorganic semiconductors, which usually have high mobility and for which quantum efficiency of photocarrier generation can reach close to 100%, polymers are believed to be low mobility materials. And because of the complexity in chain conformation and morphology, the carrier generation process in a polymer is more complicated than that in semiconductors. It has been shown that for semiconducting polymers, the transient mobility changes rapidly in the first few picoseconds upon excitation [93]. This strong time dependence requires a better temporal resolution to reveal the carrier dynamics.

5.2.2 Methods to Measure Picosecond Electrical Pulses

The shape of electrical pulses depend on the laser pulseshape, the material properties of photoconductors, the nature of the charge source and the characteristics of the associated transmission lines[98]. The voltage pulse generated in the photoconductive switch can be sampled by a second gap (as in Fig. 5.7) and variation of the time delay

between the pulse generating pump beam and the pulse sampling probe beam. The variation in the delay enables temporal resolution of the electrical pulse.

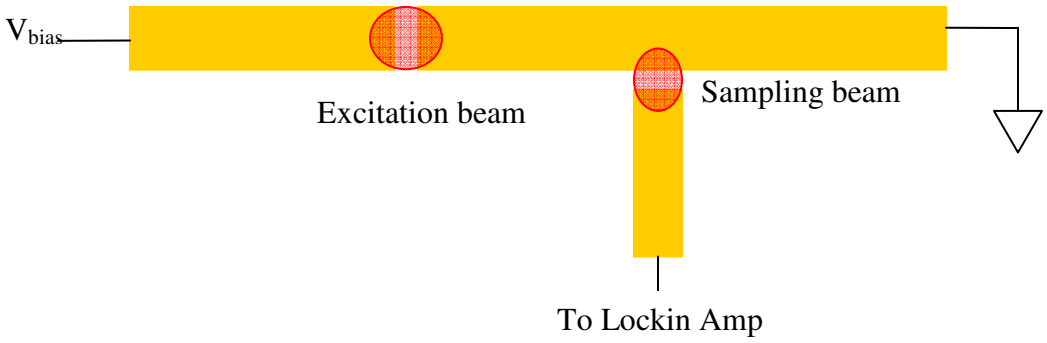

Figure 5.7 Setup showing principle for pulse generation and detection with photoconductive switches

An alternative measurement approach is to use the electro-optic effect in a crystal to do the sampling [99]. In this case, the field of the electrical pulse is sampled through the rotation of the polarization of the optical sampling pulse. Because it has demonstrated several hundred femtosecond time resolution [100], the electro-optic method is currently considered to be the fastest sampling technique. However, with careful design geometry and detection systems, it is possible to use a photoconductive switch to generate and detect sub-picosecond electrical pulses [101]. In this chapter, we will employ the photoconductive switch as a sampling tool. The resulted 2ps time resolution is far better than in past work on photoconductive sampling of polymer switches. Ongoing work is being carried out to use electro optic sampling and optimized device design (with no gap) for photoconductive sampling to reach the theoretical limitation of measurement capability.

5.3 Sampling Oscilloscope Measurements of BAMH-PPV

As a preliminary study of the characteristics of the electrical pulses generated from conjugated polymers, we used the voltage pulse waveform on a *Tektronix* sampling oscilloscope to study the bias, laser power dependence. Although the time resolution of the oscilloscope is only 20ps, the better sensitivity and experimental setup ease our further exploration of the polymer properties.

5.3.1 Device Preparation

Photoconductive switches were fabricated on a fused quartz substrate in the configuration of coplanar waveguides. BAMH-PPV polymer solution was spin-coated on top of the metal electrodes to form the active layer. Different thickness of polymers are prepared: a) 280nm film from 2% solution ; b) 780nm film from 6% solution and c) 93 nm from 0.67% solution. By using an inverted structure (electrodes under a semiconducting polymer medium), the fabrication process can be much easier than making electrodes on top of polymer films, which are generally not as smooth as semiconductor wafers. Meanwhile, to spin coat polymer after the electrodes have been fabricated minimizes the effects of chemical solutions (acetone, developer, etc.) and UV light illumination on the polymer in the process of photolithography, reducing the possibility of polymer degradation and peeling off. This configuration has a limitation on the film thickness so that light will be able to penetrate the polymer film to transfer the carriers onto the metallic electrodes. An interdigitated Metal-Polymer-Metal (MPM) switch structure was adopted. Gold was deposited on the other side of the quartz to form a 50-ohm impedance line.

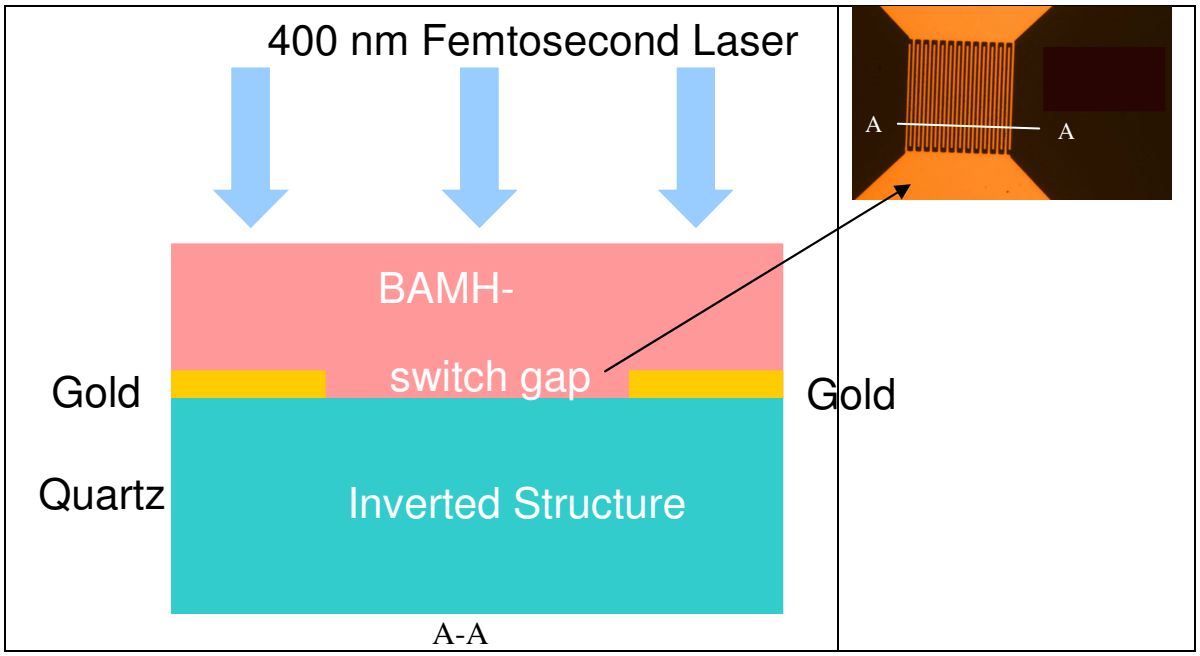

Figure 5.8 Inverted structure photoconductive switch, interdigitated, with gaps of 2μm.

The gold finger width was 1µm with a 2µm gap between fingers. The finger length was 50µm and the capacitance of the switch was 20 fF. Touching pads are added at the end of each line to accommodate the *GGB pico-probes* in the probe station. Interdigitated electrodes are employed in the active region to increase the sensitivity because polymers are far less sensitive to optical excitation than semiconductors. The capacitance of the gap increases logarithmically as the gap becomes smaller, while the sensitivity increase as l^{-2} (l is gap width), so using a small gap length to increase sensitivity won't sacrifice too much of the device speed.

5.3.2 Experiment Description

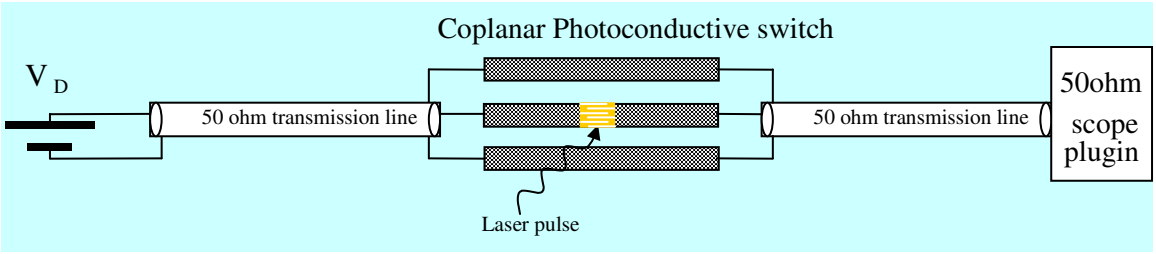

Figure 5.9 Test setup for photoconductivity of MPM devices

The BAMH-PPV photoconductive switch is illuminated with 400nm, 100fs laser pulses from a frequency-doubled Ti:sapphire laser amplifier. The transient photoconductive signal from the polymer switch is then probed with a *Tektronix* sampling oscilloscope to make systematic measurement on the transient current dependence of the illuminating laser intensity and applied bias voltage. In general a higher repetition rate will give better signal to noise ratio for sampling measurements, but if the repetition rate is too high, the BAMH PPV polymer will be burned away quickly from the quartz surface. The following experiments were carried out with 1kHz laser repetition rate.

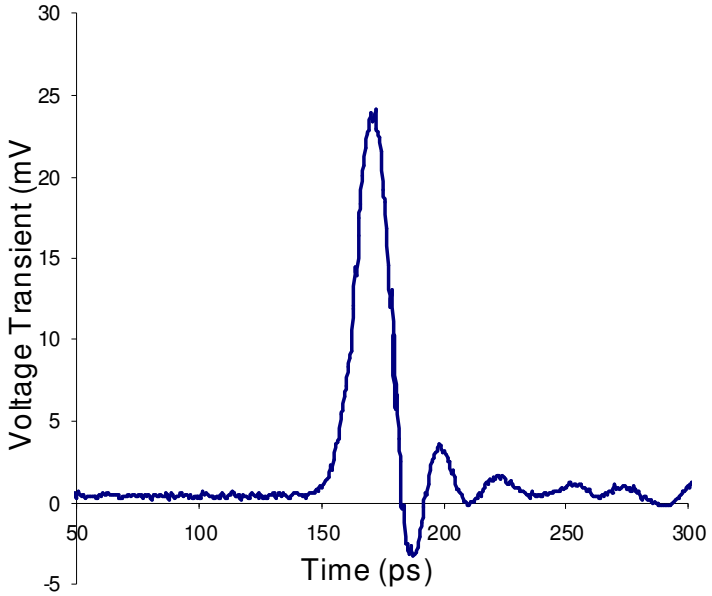

Figure 5.10 Voltage transient wave form from the MPM switch probed by oscilloscope

A typical transient voltage wave form is shown in Figure 5.10, measured at room temperature with laser pulse energy 0.5nJ/pulse and bias 200kV/cm. The rise time and fall time were less than 20ps, with a FWHM~20ps. The sharp falling edge indicates the polymer might have a very short carrier life time based on experience from LT GaAs testing. A rigorous analysis of the voltage waveform produced in the photoconductive switch is a difficult task, which requires the solution of the time-varying electromagnetic equations for the electric field produced by the radiating currents and charges in the gap.

From the voltage waveform, time dependent photoconductance can be obtained, which is directly related to carrier mobility of the photoconductive materials.

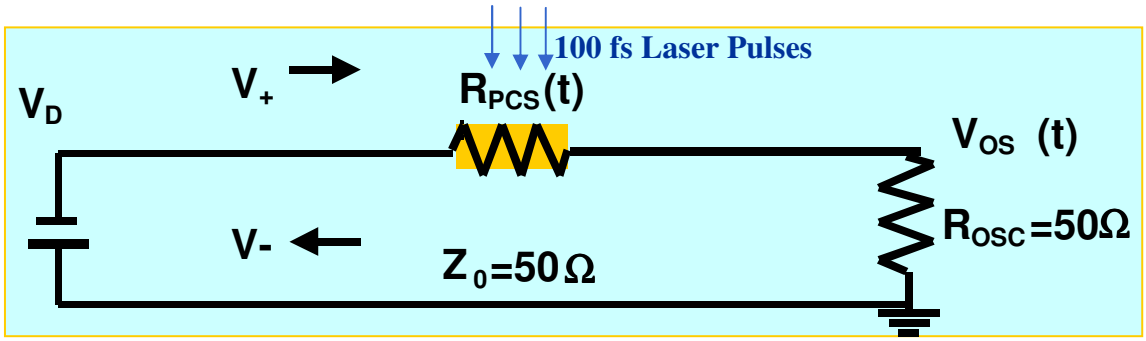

Figure 5.11 Equivalent circuit of the oscilloscope measurement

The circuit in Fig. 5.9 can be simplified as Fig. 5.11. The switch is represented by a time varying resistance $R_{pcs}(t)$. A parallel capacitance is omitted because the usual value of 20-50fF won't have a significant affect on the waveform. To get the time dependent photoconductance from the voltage wave form on the oscilloscope, consider two cases:

a). Before light illuminates on the switch, lump circuit laws can be used. The active region resistance is R_{off}, and dark voltage on the oscilloscope is V_{off}.

$$R_{off} = \frac{V_D \bullet 50\Omega}{V_{off}} - 50\Omega \tag{5.1}$$

Because of the traveling wave nature of the electrical signal, it is necessary to describe the response of the photoconductor in terms of incident, reflected, and transmitted waves. In the following equations, V_+ represents the wave toward the oscilloscope, as illustrated in Fig. 5.11, all the transmission lines have characteristic impedance of 50ohms and the oscilloscope also a load of 50ohms.

$$V_+ = \frac{V_D \bullet R_{off}}{2(R_{off} + 50\Omega)} + \frac{V_D \bullet 50\Omega}{R_{off} + 50\Omega} = V_D \frac{R_{off} + 100\Omega}{2 \bullet R_{off} + 100\Omega} \tag{5.2}$$

b). After the arrival of the femtosecond laser pulse, there is a sudden change in the resistance caused by the photocarrier generation. Because the input transmission line is long, V_+ stays constant for the duration of the switch response, and thus the relationship follows:

$$V_{osc}(t) = V_+ \bullet \gamma \bullet \frac{50\Omega}{2(R_{psc}(t) + 50\Omega)} \tag{5.3}$$

where $\gamma = \frac{100\Omega}{R_{psc}(t) + 100\Omega)}$ is the transmission coefficient. So the time dependent photoconductance expressed as a function of the voltage on the scope can be expressed as:

$$G_{psc}(t) = \frac{1}{R_{pcs}(t)} = \frac{V_{osc}(t)}{(V_D + V_{off} - 2 \bullet V_{osc}(t))50\Omega} \tag{5.4}$$

With the knowledge of time-dependent photoconductance, and with the data for switch geometry, it is possible to obtain information on photocarrier mobility and photoconductivity. It is worth pointing out that the above calculated transient photoconductance are limited by the system time resolution, i.e., RC constant of the device and circuits used. The true photoconductance of the polymer should be faster without the circuit limitations.

5.3.3 Photoconductance Dependence on Excitation Laser Pulse Energy

By varying the excitation laser power from 0.2nJ to 2.8nJ, the photoconductance's dependence on laser pulse energy was measured. For all different laser power levels we kept the external field the same, i.e., 250kV/cm. And the measurement was carried out on the 780nm thick BAMHPPV film.

Fig. 5.12 shows the dependence of transient photoconductance on laser illumination energy. The time varying photoconductance was calculated from the oscilloscope traces with Eq.(5.4). During the laser pulse illumination, the resistance of the photoconductive switch is time varying, therefore the photoconductance is a function of time. Here we are interested in the peak photoconductance. It can be seen that the peak transient photo-conductance increases linearly with the laser pulse energy up to 2*nJ* per pulse. The linear dependence implies that the carrier generation mechanism is independent of the level of excitation. Thus, photocarrier generation is a first order process with no interactions between excitations, which is typical of semiconductor phoconductivities. But when the laser pulse energy increases to 2.8*nJ*, the peak photoconductance deviates from the line and goes higher. This may be due to the fact that the laser intensity on the polymer is too high and the polymer is close to breakdown or maybe due to some nonlinear absorption or excitation process in conjugated polymers. A detailed study of the polymer is required to reveal the source of this sudden increase in photoconductivity. For the purpose of understanding photocarrier generation under normal photoexcitation, this abnormal point in the curve gave us a range of laser power to work with. For different power levels, the pulse width of the photocurrent oscilloscope trace remained almost a constant, as illustrated in Fig. 5.13. Besides the circuit parameters, the photocurrent pulse width is determined by carrier life time and carrier mobility. These two factors are not directly related to laser power levels, thus the pulsewidth dependence on laser power shows a constant value.

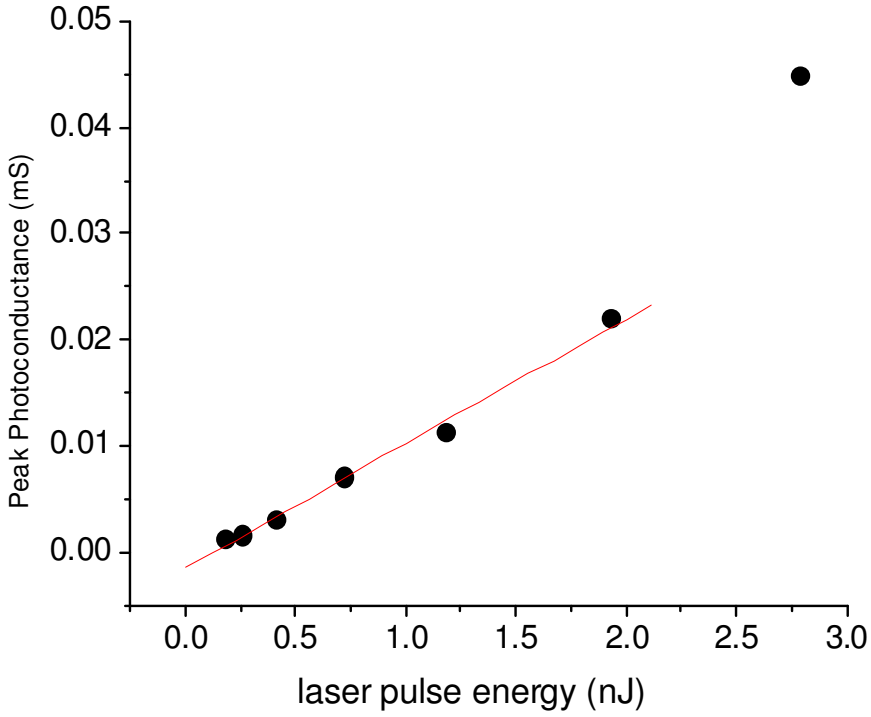

Figure 5.12 Peak transient photoconductance with different laser illumination, for electric field of 250kV/cm. Photoconductivity is estimated based on the temporal resolution of the sampling oscilloscope of 20ps. The actual peak transient photoconductivity will be higher if the bandwidth of the measuring system is higher.

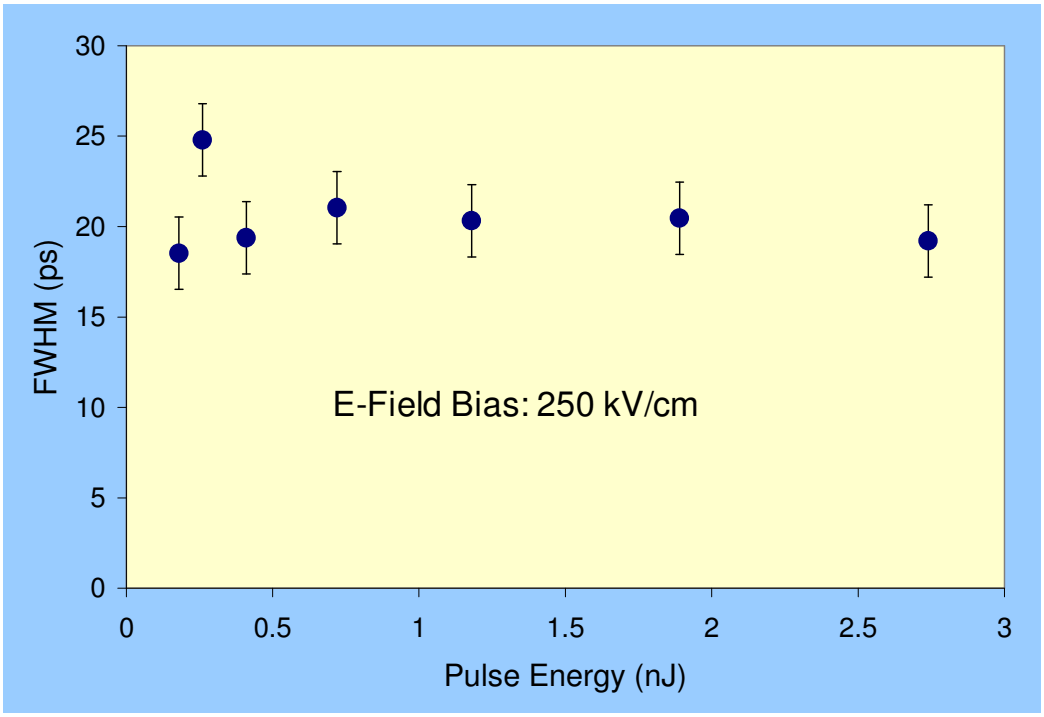

Figure 5.13 Photocurrent pulse width dependence on laser pulse energy with a fixed external bias field of 250kV/cm.

5.3.4 External Electric Field Dependence of Photoconductance

In Fig. 5.14, it can be seen that the transient photoconductance remained roughly constant at different external bias field up to $6x10^5$V/cm. This is typical of photoconductivity in semiconductors where the electronic structure can be described by band theory [26]. While increasing the applied voltage on the switch, no noticeable change of pulsewidth was observed during the experiment (Fig. 5.15). This is an indication that no carrier sweepout occurs during the pulse formation. The electrical pulsewidth is usually determined by one of two processes: carrier life time and carrier sweepout, which is shorter. Because of the low mobility of the polymers, carrier sweepout is not a main factor that influences the formation of the picosecond electric

pulse. The determining factor is therefore the carrier lifetime. Hence we can assume that during the formation of the electric pulse, carrier recombination is the dominating process which can be characterized by the photoconductive carrier lifetime. The external electric field is limited by breakdown to $6x10^5$ *V/cm*..

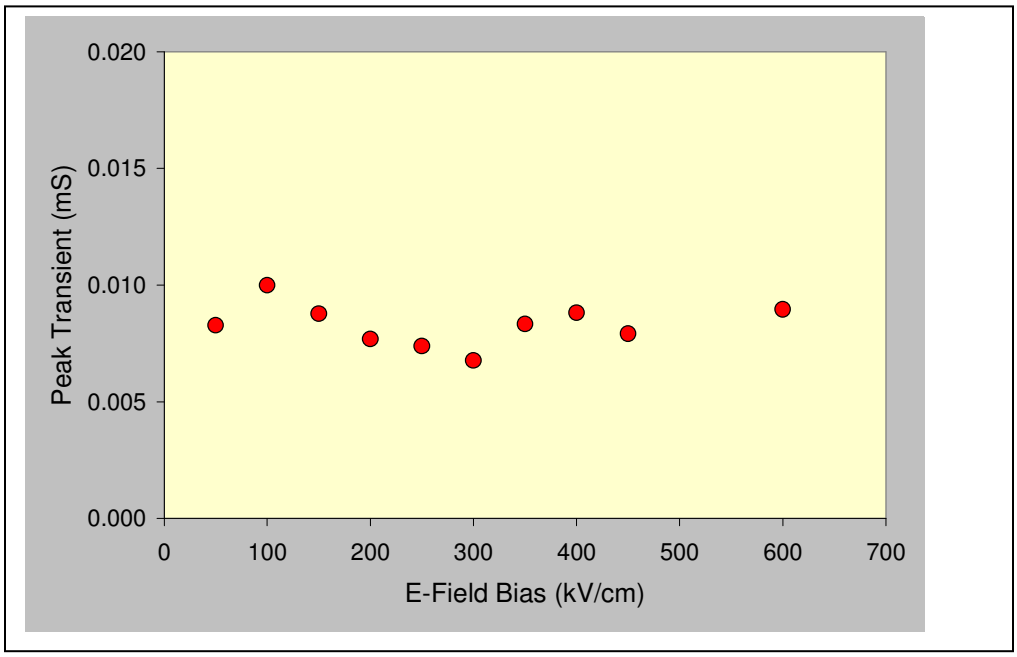

Figure 5.14 Peak transient photoconductance under different bias, laser power 0.72nj/pulse

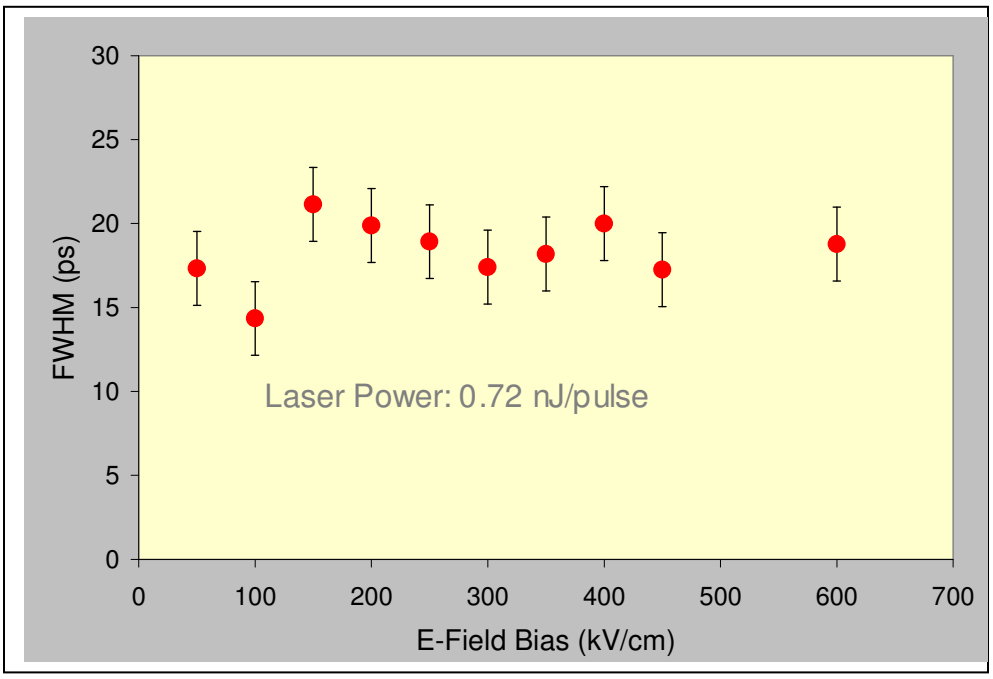

Figure 5.15 Photocurrent pulse width dependence on external field with illumination of laser pulse energy 0.*72nJ/pulse*

5.3.5 Gap-width Dependence of Transient Photoconductance

Transient photoconductance for different thicknesses of polymer films and different gap sizes are shown in Fig. 5.16. Switches fabricated on thicker film yield lower photoconductance. This is due to the fact that the absorption coefficient, α (at 400nm) of these BAMH-PPV polymer films was found to depend on the film thickness (Fig. 5. 17). Thicker films tend to exhibit crystallization, so that the absorption is higher than that of thinner ones. Images taken from a polarizing microscope are shown in Fig. 5.18. It can be seen that the 280nm thick film is more even and smooth, while the 780nm film is coarse due to crystallization. The active layer on the surface is thin and cannot penetrate deep enough to the metal electrodes for the thick film (780nm here) case; this is because the device has an inverted structure, with electrodes lying under the polymer film. When the

film is thin, more carriers have a chance to reach the electrodes beneath the polymer film. Switches with a larger finger gap width also have lower photoconductance, which is partly a contribution of gap width discussed in 5.2.1. To get better photoconductive switch behavior, we need to use thinner films with small finger gaps.

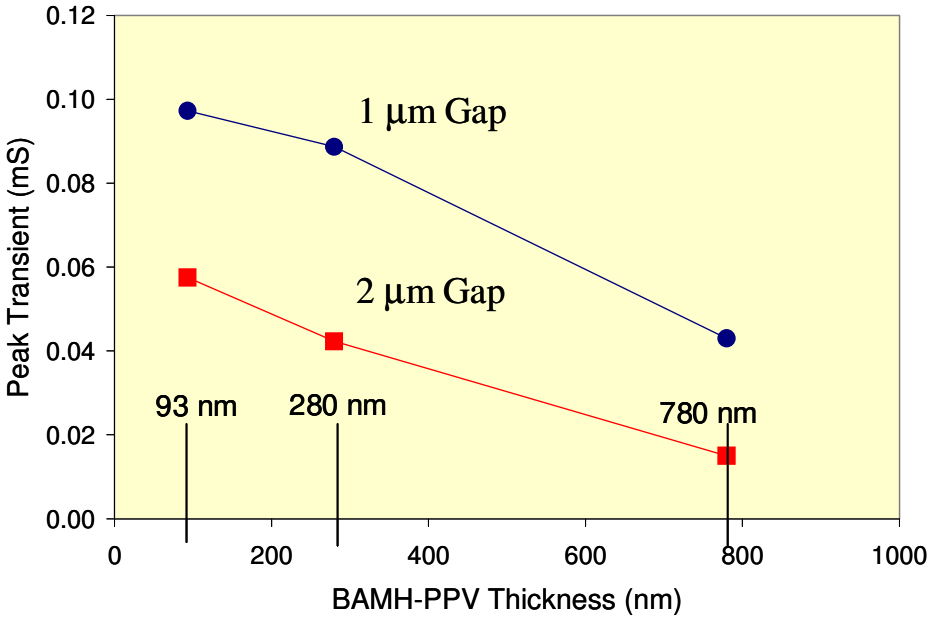

Figure 5.16 Gap-width dependence of transient photoconductance, with laser pulse energy 1.5 nJ and external electric field 250kV/cm

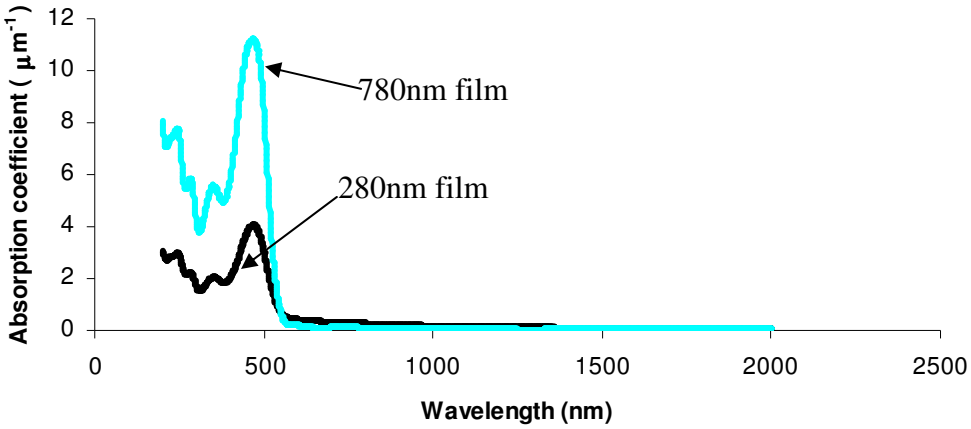

Figure 5.17 Absorption coefficient spectrum of BAMHPPV. At 400nm, $\alpha = 2.1\mu m^{-1}$, which is consistent with that measured by frequency doubled femtosecond laser pulses.

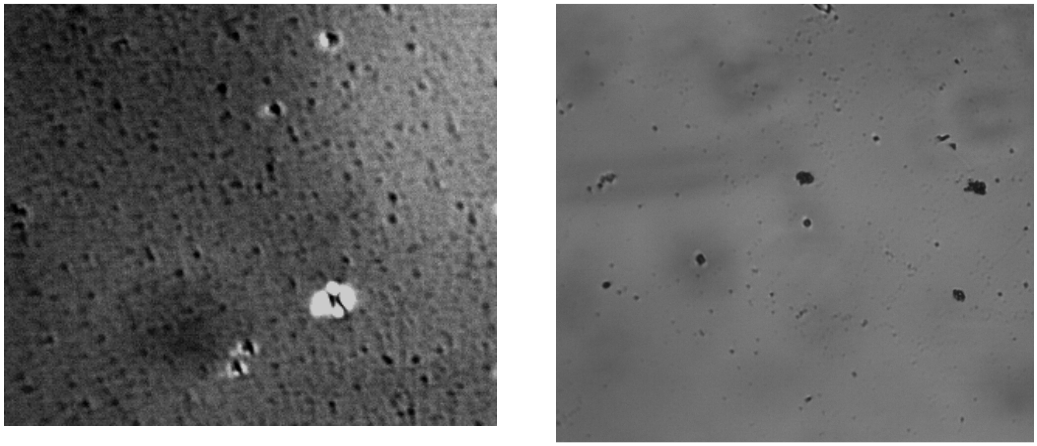

(a) (b)

Figure 5.18 Polarizing microscope images of two BAMHPPV thin films on quartz. (a) thicker (780nm) film, (b) thinner film (280nm)

5.3.6 Summary of the oscilloscope results

The photoconductance dependence on optical excitation power up to 2nj/pulse and on bias field up to 600kV/cm is consistent with the research work on photoconductivity by Heeger's group [26], while having better time resolution. The photoconductivity data obtained by oscilloscope measurements are consistent with photoexciation of charged (positive and negative) carriers in inorganic semiconductors. Illumination by light with photon energy greater than the bandgap generated carriers that promptly contribute to the photoconductivity, with a sharp rise time of the transient photocurrent. The above results are generally characteristic of photoconductivity in semiconductors where the electronic wave functions are delocalized and the electronic structure is described by band theory. Although in polymers disorder leads to localization of the wave functions, experiments have shown that for highly oriented materials the excited state wave functions are delocalized over a minimum of 50 repeat units, thus the semiconductor model can be a starting point for the excited state of ordered conjugated polymer.

The above measurements were implemented by using a sampling oscilloscope with limited bandwidth (temporal resolution 20ps). A pump probe method can give more accurate measurements of the ultrashort electric pulse duration by using shorter sampling gate produced by photoconductive switches.

5.4 Photoconductive Sampling on BAMHPPV

5.4.1 Device Layout for Pump Probe Measurements

Two interdigitated photoconductive switches were fabricated on fused quartz substrate in a cross configuration. As in 5.3.1, polymer solution was spin-coated on top of the metal electrodes to form the active layer, as shown in Fig. 5.19. The polymer used was BAMHPPV for the pump probe measurement. The two MPM switches are at a distance less than 50μm right across the center line to minimize the possible dispersion caused by transmission line. The gold finger width was 1μm with a 2μm gap between fingers. The finger length was 50μm and the capacitance of each switch was estimated to be 20 fF.

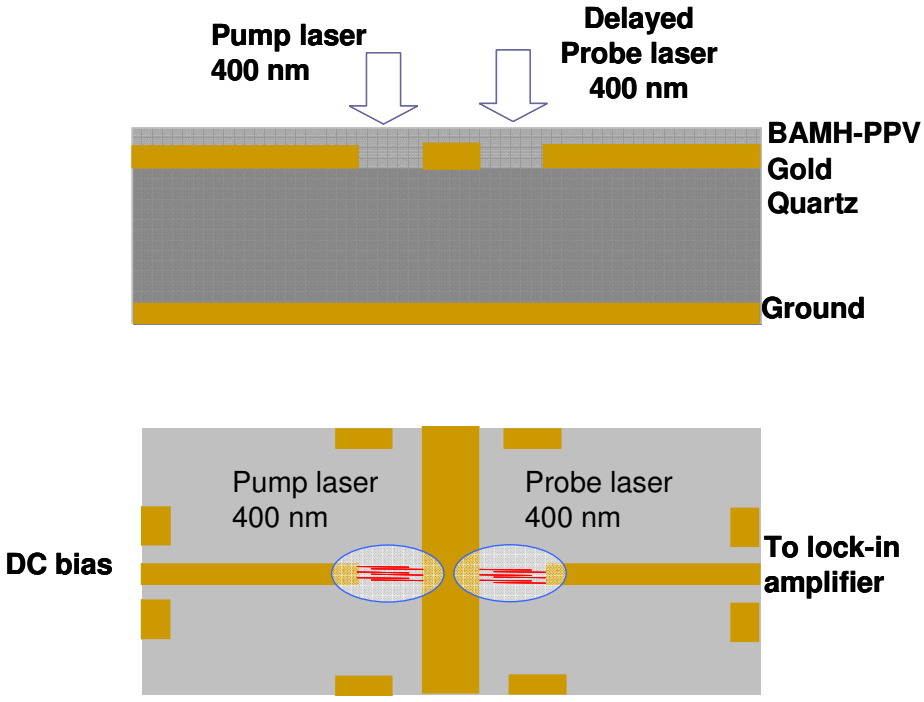

Figure 5.19 Device for the pump probe measurement. The switches are interdigitated, with gaps of 2μm. The pads at each end of transmission line are design to accommodate the picoprobes for applying bias and taking signal.

5.4.2 Experiment setup for photoconductive sampling

To measure the duration of the electric pulse from the BAMH-PPV photoconductive switch, which is a representative of the carrier life time of the material, a pump probe scheme was employed. Instead of using the sampling oscilloscope, the second photoconductive switch was used to probe the transient current wave form. Both switches are illuminated with 400nm light from a femtosecond laser amplifier running at a repetition of 40 kHz. The experiment layout is shown in Fig. 5.20.

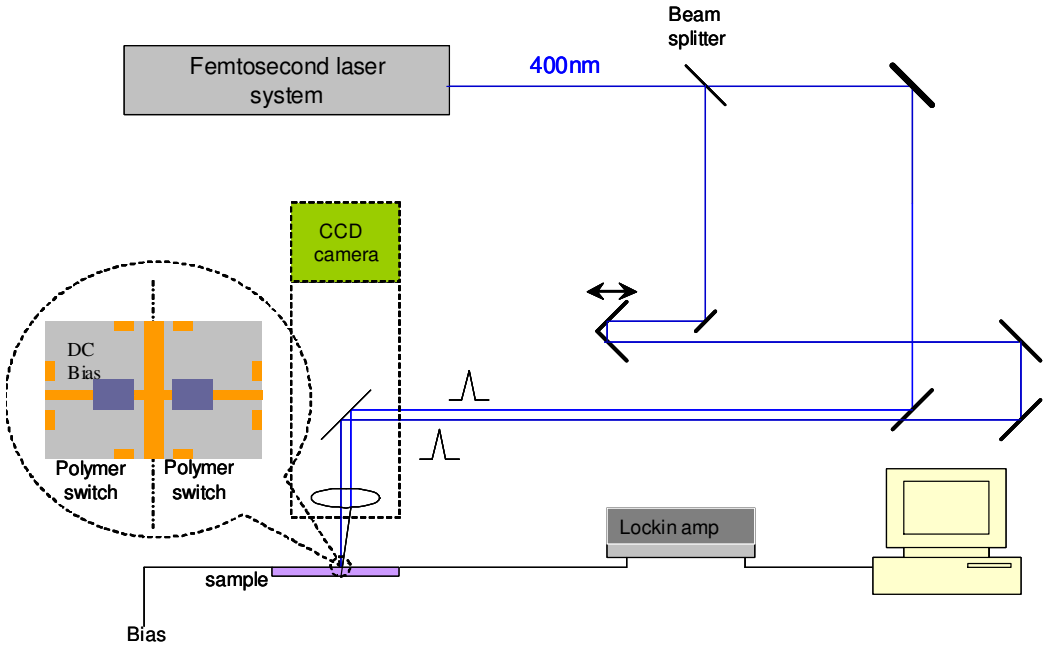

Figure 5.20 Pump probe measurement layout for photoconductive sampling

The light from the femtosecond Ti:sapphire laser amplifier was frequency doubled so that the photon energy can reach the absorption region of the polymer. A beam splitter divided the laser beam into two with almost equal power: one for pump, generating the transient electrical pulse to be measured; the other beam for probe, which

was delayed with respect to the pump pulse by a translational stage driven by a stepping motor. After passing the optical delay line, the probe beam was combined with pump beam by a beam splitter to co-propagate to the focusing element. A *Nectar* upright microscope was used to focus both beams on the sample surface. At the same time, the CCD camera can observe the sample and focal points on the sample surface to ease alignment. When using a long working distance 50xobjective, a focal point as small as 2um can be obtained, and easily located on any part of the switch. For general measurement a 10x objective was used. Because of the low pulse amplitude from the polymer photoconductive switch, the sampled signal is extremely weak and synchronous signal detection was employed by using a SRS 830 digital lock-in amplifier. A chopper is used in the pump beam, at a frequency of 1.6kHz. The signal sampled by the probe switch is sent to the lock-in amplifier, which uses the chopper frequency as a reference. The lock-in reading was transferred to the control computer, which was running Labview programs that both control the delay line translational stage and collect data.

5.4.3 Results and Discussions

By delaying the probe beam with respect to the pump beam and taking the sampled data from lock-in amplifier as a function of delay time, the pulse width can be measured, which is only limited by the gap capacitance and laser pulse width. As seen Fig. 5.21, the measured autocorrelation curve has a FWHM of ~4ps. If a Gaussian pulse shape is assumed, the electrical pulse from the BAMH-PPV photoconductive switch has pulse duration of 2ps, which is much shorter than the oscilloscope results.

When a rapid process to be measured is faster than the measuring instrument's time resolution, the measured signal amplitude will increase with the resolution of the instrument due to shorter averaging time. Actually, the following equations holds true:

$$\int \sigma(t)dt \propto \sigma_p(t)\Big|_{osc} \bullet \Delta t\Big|_{osc} = \sigma_p(t)\Big|_{pumpprobe} \bullet \Delta t\Big|_{pumpprobe} \tag{5.5}$$

It is reasonable to assume that the product of signal amplitude and pulsewidth remains roughly the same for different measuring systems with different resolutions.

From Eq (5-4), photo-conductance has the same time dependence as the measured voltage signal. So we can combine the results of the photo-conductance based on the oscilloscope measurements with the pulsewidth measured by pump probe method. When applying the 2ps pulse width to the sampling oscilloscope data of above, the peak photo-conductance will be 10 times higher.

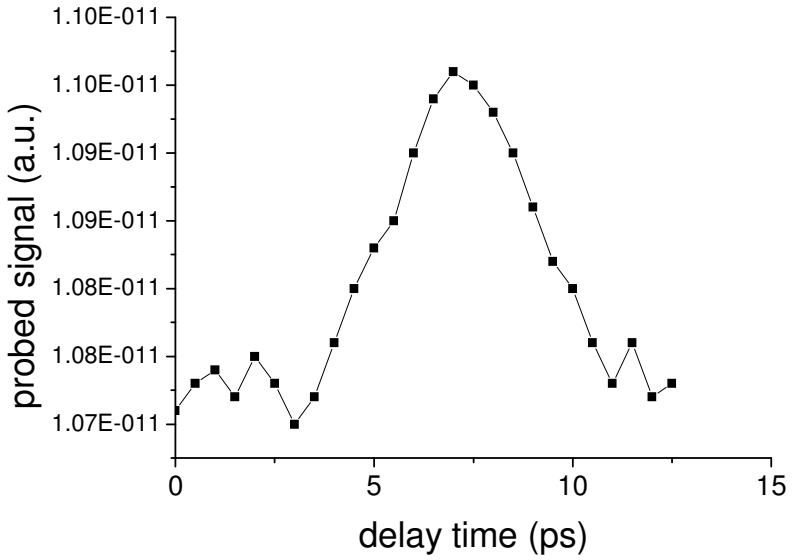

Figure 5.21 Autocorrelation measurement of electric pulses from BAMH-PPV MPM switches, FWHM=4ps.

One may estimate the carrier mobility in the BAMH-PPV film based on the transient photo-conductance and the parameters of the laser and the MPM device. The absorption coefficient, α of BAMH-PPV polymer films depends on the film thickness and is greater for thicker films, as mentioned previously. The carrier density n can also be estimated using the laser power, the absorption coefficient α and the geometry of the laser spot. As a result, the photoconductivity σ and the mobility μ of the BAMH-PPV thin film can be estimated according to the following equations:

$$\sigma = \frac{GL}{A}, \qquad \mu = \frac{\sigma}{ne}, \tag{5.6}$$

where G is the peak transient photo-conductance, A is the cross section of the switch (can be estimated by finger length times film thickness), L is the width of finger gap and n is carrier density, given by Eq. (5-7). And the laser pulse energy is 1.5*nj*/pulse. The carrier density can be calculated as:

$$n = \phi(1-R)\frac{(1-e^{-\alpha d})}{d}\frac{I_{pulse}\Delta t}{\hbar\omega} \tag{5.7}$$

where ϕ represents quantum efficiency, R represents film reflection, d is film thickness, I_{pulse} is laser intensity and Δt is laser pulse width. The results are shown in the Table 1, assuming a quantum efficiency of 1.

Thickness (nm)	G_{peak} (mS)	L (μm)	α (μm^{-1})	*N* ($x10^{18}\ cm^{-3}$)	σ $(\Omega cm)^{-1}$	μ (cm^2/Vs)
93	0.10	1	1.9	2.6	$8.3x10^{-2}$	0.2
93	0.06	2	1.9	2.6	$9.8x10^{-2}$	0.24
280	0.09	1	2.1	2.3	$2.6x10^{-3}$	0.07
280	0.04	2	2.1	2.3	$2.3x10^{-3}$	0.06
780	0.05	1	5.6	1.8	$5.1x10^{-3}$	0.02
780	0.015	2	5.6	1.8	$3.1x10^{-3}$	0.01

Table 5.1 Summary of experimental data on transient photoconductivity and mobility measurements (when assuming the quantum efficiency to be 1).

From Table 1, a transient carrier mobility of $0.2cm^2/Vs$ was estimated for a 93nm thick film of BAMH-PPV when the measuring system time resolution is 2ps. This value is 10 times higher than the data in [26], in which the measurement was based on a system resolution of 50ps. One obvious fact seen from Eq. (5.6) is that the transient carrier mobility is time dependent. When the measuring system resolution is lower than the actual mobility change, only an averaged value is detected, which is lower than the true value. So to have a fast measuring facility is the key to getting a result close to reality.

When calculating the photocarrier density, we made an assumption that all the photons absorbed by the polymer contribute carrier generation, i.e. the quantum efficiency equals to 1. In reality, only a portion of the photons create carriers. From a recent paper by Hendry et al [93], it was estimated that the quantum efficiency for charge

generation in PPV polymers could be less than 0.05%. When taking this into account, the value of the transient carrier mobility in our experiment could be as high as 480cm^2/Vs, based on the 2ps time resolution.

It should be noted that both n and μ in Eq. (5-6) are rapid time dependent functions and cannot be independently measured in this work. We can only provide an estimate of the transient mobility based on the assumption of the value of photocarrier density n. If the photocarriers are generated instantaneously upon laser excitation and the relaxation is not much quicker than mobility change, we can obtain the value of n by considering all the photons absorbed create photocarriers with certain quantum efficiency [93]. Due to the fast time variation of μ compared with the time resolution in this work and the nature of photo-excitation in semiconductors, this assumption on photo carrier density is reasonable.

In Hendry's work [93], THz emission spectroscopy was used to study charge carrier generation and time-dependent carrier mobility in PPV polymer. By analyzing the THz emission waveform from a polymer antenna, the carrier mobility showed strong time-dependence, with a very large initial value (within first 1ps), decreasing rapidly towards a small steady state value [~$10^{-5} cm^2/Vs$]. The time resolution is on the order of 200fs. When the time resolution is lower, the mobility will be an average over the system's smallest resolvable time duration. Considering the measuring system time resolution to be 2ps, by using the time-dependent mobility curve in Hendry's paper and integrating it from origin to 2ps, we obtained an average mobility of ~540cm^2/Vs (please note this value is derived from Hendry's experiment [93]), which is extremely close to the results of our experiment.

From table 5.1 it is seen that mobility is larger at thinner film thickness. This is mainly device limited. As discussed in the previous section, thicker films have a higher absorption coefficient, leading to a lower photoconductivity. It can be noted that for 93nm film the photoconductivity is around 15-30 times that of 780nm films. An alternative method to avoid the intrinsic shortcoming of the inverted structure could be illuminating from the bottom of the device.

Based on the values of carrier life time ($2ps$), mobility ($480cm^2/Vs$) and applied electric field ($250kV/cm$), we can calculate the mean free path of the carriers:

$$l = v \cdot \tau = 250 \times 10^3 \times 480 \times 2 \times 10^{-12} = 1.2 \times 10^{-4} cm$$

5.4.4 Summary on photoconductive sampling of BAMHPPV switches

Electric pulses were generated from BAMHPPV polymer MPM switches with a width of few picoseconds, the shortest on wafer measurement result obtained on PPV devices to date. The pulsewidth is only restricted by the devices' circuit parameters. Dynamic photoconductive properties of BAMH-PPV polymers have been investigated. A carrier life time less than 2 picoseconds was estimated based on the generated picosecond electric pulses. Transient carrier mobility as high as 480 cm^2/Vs was estimated when assuming a quantum efficiency of 0.05% [93]. And the carrier mobility is independent of the bias field up to $6x10^5$ kV/cm. There is still room to improve the temporal resolution of the measurement system to get more accurate values of the pulse width, photoconductance, and also the carrier mobility.

5.5 Photoconductive Sampling on MEH PPV

MEH-PPV is another important conjugated polymer which is widely used in semiconducting polymer devices such as transistors, solar cells, etc. As to transient photoconductivity, we observed stronger signals from MEH-PPV MPM switches, which may be due to higher mobility in this kind of film. In this section, photoconductive sampling measurement was carried out on MEH-PPV switches in a similar way as that of BAMH-PPV. Meanwhile, a new photoconductive sampling scheme using only one switch was implemented. To remove the influence of device factors, transient reflectivity was also measured.

5.5.1 Two-switch Photoconductive Sampling of MEH PPV

Initially the measurements on BAMH PPV was repeated in MEH PPV. The experiments was carried out using a different laser system (Spectra Physics Hurricane), with 1kHz repetition rate and up to 1mj pulse energy. The low repetition rate is beneficial to polymer studies because the ablation is proportional to the average power of the laser light. Using low repetition rate will result in longer measurement time per device. A drawback of low repetition rate is the increase of 1/f noise, which can be minimized by careful experiment design.

The experiment layout and device preparation are the same as in sections 5.4.1. and 5.4.2, so it won't be repeated here. One modification of the setup is the way to trigger the lock-in amplifier. In 5.4.2 a chopper was used to provide a reference for the lock-in amplifier, and the chopper frequency was set at 1.4-1.6kHz. In this section, the signal from the laser amplifier at 1kHz was used as a reference. In this way the signal and

reference are in real synchronization, resulting in minimum jitter. While the pump and probe are not differentiated, the device must have no detectable photovoltaic effect. In practice, the laser frequency triggering gives a better S/N than the chopper in a low repetition situation. The results are presented in Fig. 5. 22.

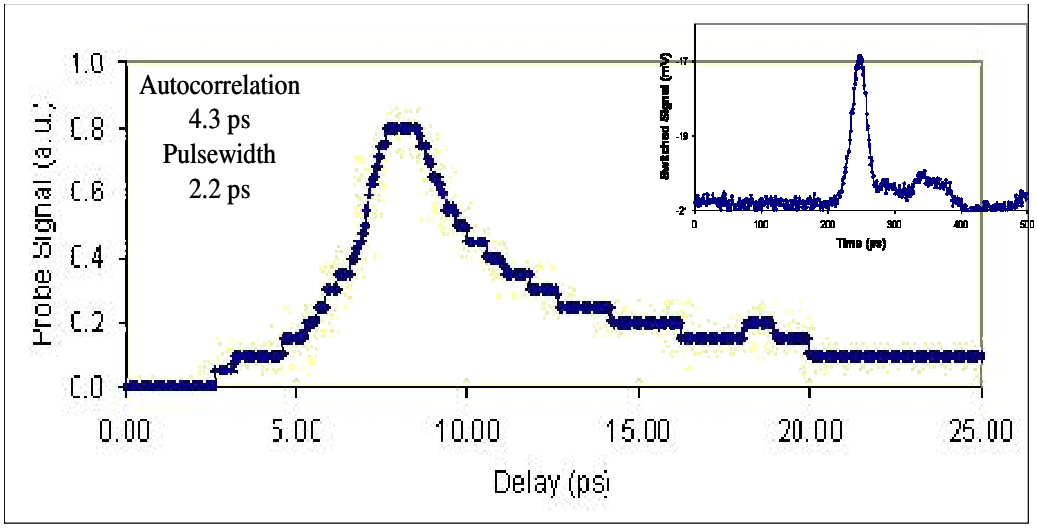

Figure 5.22 Autocorrelation measurement of MEHPPV switches. FWHM= 4.3ps, and electric pulse width ~2.2ps under Gaussian shape assumption. Inset is oscilloscope trace of the electric pulse.

5.5.2 Single-gap Photoconductive Sampling on MEHPPV

Traditionally, photoconductive sampling is implemented with two photoconductive switches, one for signal generation and the other for gated detection, as in section 5.4.2 and 5.5.1. In this section, an alternative sampling technique using a one-gap switch is presented. The advantage of using only one gap is the simplicity of structure, small capacitance (half that of a two switches configuration), no transmission

of fast electrical signal so dispersion-free, also the laser energy and bias voltage don't need to be as high as in the two-switch case.

The device is a simple photoconductive switch as illustrated in Fig. 5.6 which was voltage biased through a 50 transmission line and illuminated with 400 nm, 100 fs laser pulses at a repetition rate of 1 kHz. The experimental layout is the same as in Fig. 5.20. The modulation was provided by a sinusoidal wave applied to the switch as bias voltage. One fact must be point out here is that the switched-out pulse from the photoconductive switch is proportional to the dark resistance of the switch. The higher the dark resistance, the higher amplitude of the voltage pulse will be achieved, as indicated in Eq. (5.2) (5.3). Before the pump and probe pulses overlaps, the lock-in reading as a function of pump-probe delay was a constant, proportional to the sum of the pump and probe pulse amplitudes. As the two pulses move closer, the reading on the lock-in amplifier drops. When the two pulses are separated in time, both pump and probe pulses can be described by Eq. (5.2) and Eq. (5.3), with the same R_{off} (dark resistance). When the two pulses begin to overlap, the decrease of the gap resistance caused by the leading pulse doesn't have enough time to restore, resulting in a lower dark resistance for the second pulse. For the second pulse, R_{off} in Eq. (5.3) need to be replaced by a smaller value due to the existence of the leading pulse. So the lock-in amplifier reading is smaller than when the two pulses are totally separated. The photoconductive sampling results are shown in Fig. 5.23. Trace 1, 2, 3 corresponding to pump on/probe off, pump off/probe on, both on.

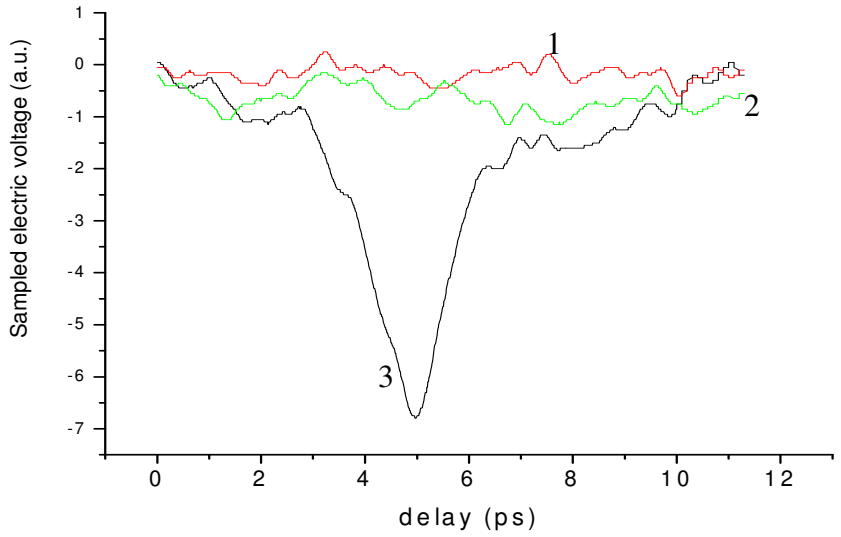

Figure 5.23 Single switch autocorrelation of photocurrent pulses on MEHPPV. Curve 1: pump on, probe off; Curve 2: pump off, probe on; Curve 3: pump on, probe on.

The FWHM of autocorrelation curve is less than 2ps, with a photocurrent pulse width 900fs with a Gaussian pulse shape assumption. The one-switch autocorrelation greatly reduced the complexity of photoconductive sampling and device design considerations.

The loose requirement on voltage and laser power enabled us to make systematic study of the autocorrelation signal's dependence on bias voltage and laser power. The bias voltage dependence of the photoconductive sampled signal is shown in Fig. 5.24. As voltage increases, the autocorrelation signal shows a linear dependence except the first point with smallest voltage. When the illumination level is the same, the MPM switch serves as a resistor and the proportion of voltage drop on the switch should be fixed. Thus changing external bias will lead to a linear dependence for typical photoconductive switches.

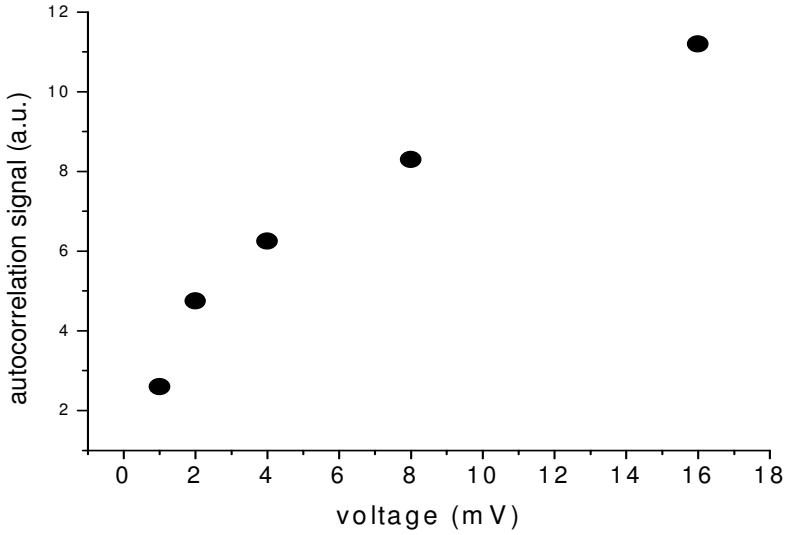

Figure 5.24 Sampled signal vs. bias voltage, with fixed optical power of 4nj/pulse. The switch has a finger gap width of 2μm.

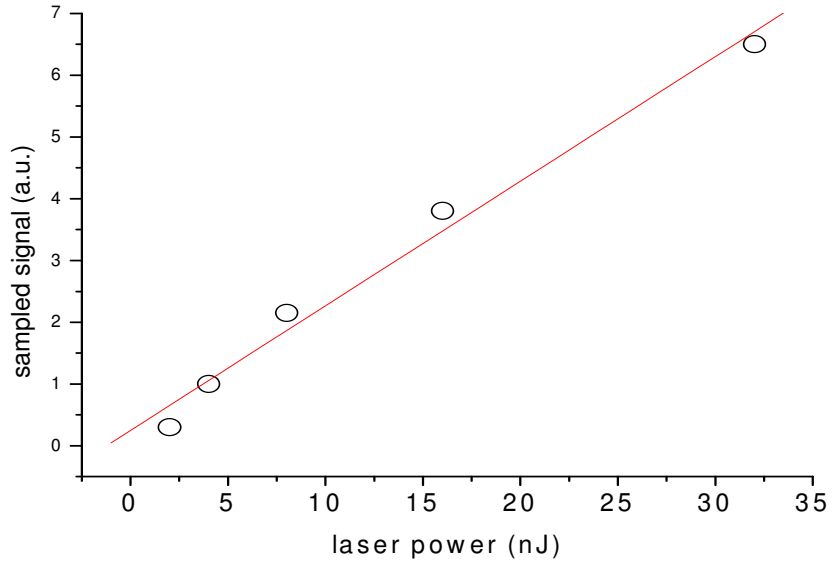

Figure 5.25 Lock-in measured sampled signal vs. excitation laser power with a 10V bias.

As the laser power increases, a linear dependence is also observed, as in Fig. 5.25. The observed signal is proportional to the number of photocarriers generated in the polymer switch. At a fixed bias voltage, more laser power produce more carrier before saturation at a certain high laser power.

Pulsewidth showed no significant change upon increasing bias voltage up to 160V for a 2um switch gap width. Thus no carrier sweep-out-effects show up for electric field up to $8x10^5$V/cm.

Using equations (5-4)-(5-7), photoconductivity and mobility of MEHPPV can be estimated. The absorption coefficient *a* of MEH-PPV polymer films was measured to be 2~5 μm^{-1} at 400 *nm,* which depended on the film thickness because thicker films tended to exhibit crystallization. The maximum carrier density *n* can also be estimated using laser power, absorption coefficient and laser spot size the same way as in section 5.4.2. As a result, a transient carrier mobility lower limit of μ=0.4cm^2/Vs was estimated for a 100 nm-thick MEH-PPV film if a quantum yield of charge carriers is set at η=1. If we use the estimate in Hendry's paper [93], the quantum efficiency can be taken as 0.05%. The transient photoconductive mobility can be calculated ~800 cm^2/Vs, also close to the estimate based on the [93], much larger than the steady state values.

5.6 Transient Reflectivity Change of MEHPPV

The key to answer many questions regarding the photoexcitation processes in conjugated polymers is a fast enough method to measure the process of carrier generation. The time resolution of photoconductive sampling is limited by device capacitance/inductance. Great care has to be taken to get a high time resolution when

doing photoconductive sampling. While photoconductive sampling is a unique tool in characterizing ultrashort electric pulses, the reflectivity/transmitivity change is more directly related to the carrier dynamics [102-105].

In this section, measurements of photo-induced change in reflectivity of MEH-PPV thin polymer films have been initiated. The experiment setup is shown in Fig. 5.26. The pump probe setup is mostly the same as in the previous sections of this chapter, except that the laser source is two colored: 400nm for carrier generation with an 800nm light for probing the reflectivity change. The two-color scheme prevented the interference between pump and probe beams. The microscope monitoring system is the same as photoconductivity measurement. A balanced detector was used to remove the DC component in the probe beam by adding a reference beam. The reflectivity change is a very small amount and this can help increase the sensitivity of the detection system and S/N ratio.

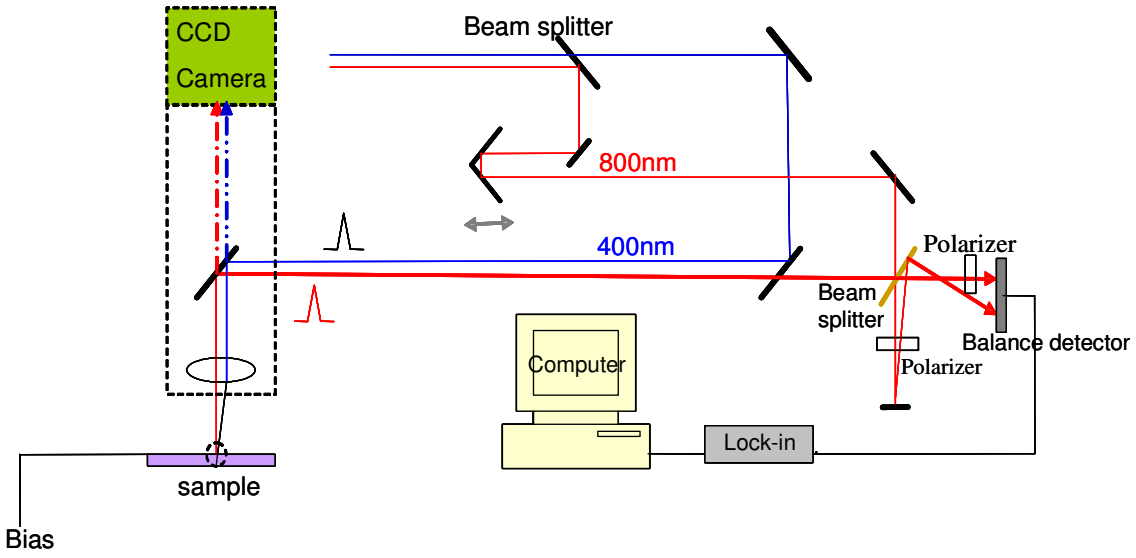

Figure 5.26 pump probe setup for photo-induced reflectivity change measurement.

Maximum photo-induced change of reflectivity $\Delta R/R$=8x10^{-5} in MEH-PPV films has been measured with an incident laser pulse energy of ~10nj, shown in Figure 5.27. This value is similar as that reported in semiconductors.

Without pumping, the reflectivity of MEH PPV can be calculated as:

$$R = r^2 = [(n-1)/(n+1)]^2 \qquad (5.8)$$

for normal incidence. n is the refraction index of MEH PPV at 800nm. The change of reflectivity of the polymer originates from the change in refractive index, which is induced by the electron-hole plasma generated by pump laser beam. The relation between refractive index change and reflectivity change can be derived from Eq (5.8):

$$\frac{dR}{R} = \frac{4n_0}{n_0^2 - 1} \bullet \frac{dn}{n_0} \qquad (5.9)$$

where n_0 is the refractive index of MEH-PPV at 800nm, *dn, dR* are the change in refractive index caused by laser illumination. dn/n_0 can be calculated to be $1.7\text{x}10^{-5}$. To an excellent approximation, this fraction of refractive index can be expressed as [103]:

$$\frac{dn}{n_0} = \frac{2\pi e^2}{\varepsilon_0 m^* \omega^2} N \qquad (5.10)$$

where the MEH PPV refractive index n_0=1.8 at 800nm and dielectric constant ε_0=3.2. m^* is the effective mass of electrons and holes, and here we assume $m^*=m_e$. ω is the probe angular frequency. *N* is electron-hole pair density. The maximum electron-hole pair density can be calculated using Eq. (5.10) to be $6x10^{15}\ cm^{-3}$.

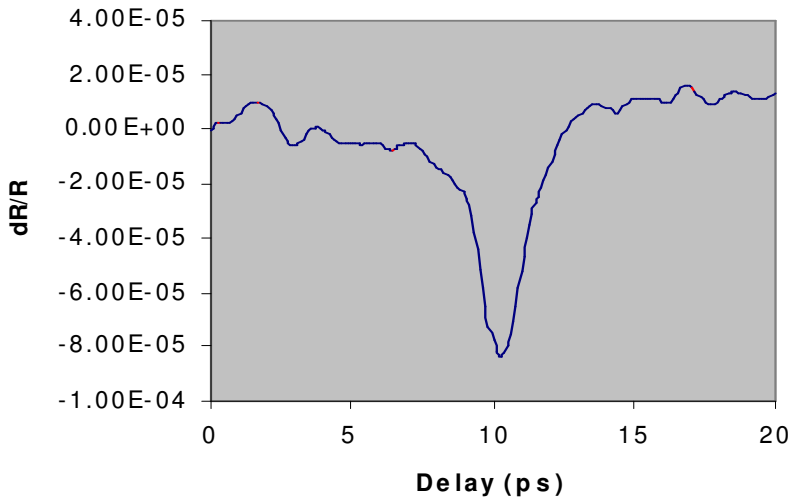

Figure 5.27 Transient reflectivity change of MEHPPV

The absorbed pump photons in MEH PPV can be estimated using Eq. (5.7). Considering the film thickness *d*= 100nm, laser spot radius 4μm, absorption coefficient $\alpha=3\mu m^{-1}$, and pump laser pulse energy to be 10nj, absorbed photon density can be calculated to be $1.2x10^{18}cm^{-3}$. The value of carrier density divided by the absorbed

photon density can be used as a rough estimation of the carrier generation quantum efficiency, which is $5x10^{-3}$.

The reflectivity change happens in a transient time as short as 1ps. This is an indication that the whole process of charge generation is within 1ps, since the reflectivity change is only determined by the material property and laser used.

5.7 Conclusions

In this chapter the photocarrier generation process was studied by photoconductive sampling and reflectivity change measurement. A new method of photoconductive sampling is proposed and some results obtained which showed its advantages. Electric pulses as short as 1 picosecond were generated in MPM switches, which indicated the carrier mobility μ=0.4cm^2/Vs assuming quantum efficiency to be 1. By using optimized device design and experiment setup, the measured photoconductive switching performance is the best results so far, both for conventional two gap sampling and the improved one gap sampling. Signal to noise ratio need to be improved and polymers need to be controlled to get a clearer picture in the carrier generation and transport mechanisms.

Chapter 6: Generation and Detection of THz Radiation Using Polymers

Terahertz radiation (THz) generation by optical rectification using NLO polymer started in the mid 1990's, initiated by Nahata [106] and Hayden [107]. Recently with the maturity of NLO polymer fabrication techniques, more choices become available as organic THz sources. In the past few years a series of papers have been published by Hayden's group at UMBC on this topic [107] [108] [109].

In this chapter we use a home-poled polymer with thickness of $7\mu m$ to get comparable THz radiation strength as $80\mu m$ ZnCdTe. At the same time, the optimized spot size for high efficiency THz radiation by optical rectification is studied in NLO polymer. Some applications of THz are explored.

6.1 THz Introduction

6.1.1. Brief History

"Terahertz radiation" is loosely defined as the electromagnetic waves with frequencies between 0.1 and 10 THz (1THz=10^{12} cycles per second). Being a bridge to the gap between infrared light and microwave radiation (see Fig. 6.1), THz radiation is resistant to the techniques commonly employed in these well established neighboring bands [110]. Until recently neither solely electronic nor solely optical devices have existed that can act as inexpensive, efficient, compact coherent THz sources. And due to the strong absorption in atmosphere, the use of THz, for a long time, has been limited to

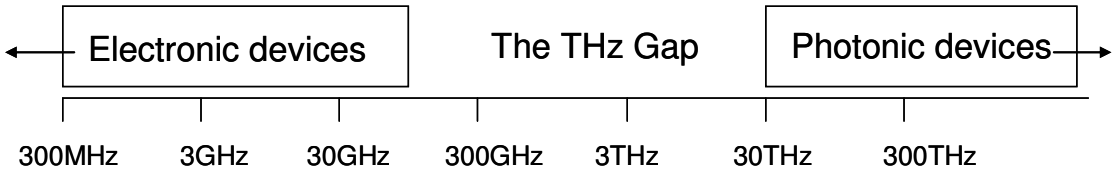

Figure 6.1 The electromagnetic spectrum

chemists and astronomers in the spectral analysis of the rotation and vibration resonances and thermal emission lines of small molecules. Historically, techniques borrowed from microwave and millimeter wave communities dominated the progress in THz science and technology for many years. In the 1970s, Yang et al. generated THz radiation using intense laser by nonlinear frequency conversion [111], and opened the door for THz generation by "quasi-optical" methods. In 1984, Auston et al. published a paper using a photoconductive switch illuminated by a CPM ring dye laser (100fs) to generate coherent THz radiation [112]. In the same year, the Auston group published another paper introducing femtosecond electrical transient generation and detection by electrooptic crystals, which nowadays have become standard methods for THz generation and detection [113]. In the paper the electrical pulse was generated and detected in the same piece of $LiTaO_3$ crystal. With progress of intense optical sources (especially Ti:sapphire lasers) and advanced material research, a plethora of new generation and detection schemes have been developed over the past twenty years. Currently the two main methods in use for generation and detection of wideband THz radiation utilize photoconductive dipole antennas or electro-optic materials. Between these two methods, photoconductive antennas have higher energy output as THz emitter and superior sensitivity as detector, but have been limited to a bandwidth of 7THz generally [114].

Electro-optic materials have a higher frequency range. With ZnTe, a widely used crystal in THz generation and detection, 30THz [115] can be reached. Recently 41THz radiation from CaSe was reported [116]. And with the organic crystal DAST, performance as good as 20THz has been demonstrated [117]. Due to their good phase matching conditions and high electro-optic coefficients, EO polymers are promising materials to increase the spectral response as well as the signal-to-noise ratio of THz systems [109].

Due to the presence of new, higher power THz sources and new methods of detection, the potential of THz for advanced physics research and commercial applications has been demonstrated. THz technology is becoming an attractive research field, with interest from sectors as diverse as semiconductor, medical, manufacturing, space and defense industries.

6.1.2 What is special in THz

The intense interest in the THz frequency range originates not only from its unique position between microwaves and IR in the electromagnetic spectrum, but also due to the physical phenomena and material responses in this frequency range. Some of the features are summarized as follows [118]:

(1) THz radiation has low photon energies (4meV @ 1 THz, one million times weaker than x- ray photons), and is non-photon-ionizing. So compared with x-rays, THz is a much safer source that has the ability to penetrate items.

(2) THz fields interact with small polar molecules but don't interact with non-polar. The absorption spectra of many polar molecules, such as H_2O, C, N_2, O_3, CO etc have unique spectral peaks in the hundreds of GHz to THz range. This makes the THz range of

importance in monitoring the atmosphere for ozone depletion measurement, air pollution detection or gas sensing.

(3) Complex biological molecules have absorption spectra in the THz band. DNA, RNA and even proteins and whole bacterial spores have been studied using THz techniques. THz technology can be used both to study biological tissues or other biological constituents and it can also be used to detect and identify of biological agents.

(4) Small antenna arrays and circuits can be used in the THz range due to the small wavelength compared with microwaves and millimeter waves. This allows miniaturized imaging devices for medical and other purposes. Despite their reduced size, THz devices are able to send or receive no less information encoded in the wideband THz signals.

(5) For high speed communication purposes, 1-10 THz/s optical systems are being investigated and may become commercially available in the next decade. THz modulators able to modulate ultrafast laser diodes will use quantum devices such as ballistic diodes or transistors with a cutoff frequency well above 10THz [118].

It is obvious that THz technology is showing great potential in both research activities in physics, chemistry and biology, but also is benefiting the computer industry and communications.

6.1.3 Terahertz Spectroscopy

At a fundamental level, what distinguishes one spectral region from another is how radiation interacts with matter. A wide range of materials, from inorganic semiconductors, superconductor, organic polymers to biological tissues, have unique spectral characteristics in the THz frequency range. Terahertz spectroscopy allows

materials' far-infrared optical properties to be determined as a function of frequency, thus giving insight to material characteristics for a wide range of applications. Different methods exist for THz spectroscopy. Fourier transform spectroscopy (FTS) is realized by illuminating the sample with a broadband thermal source such as an arc lamp or SiC globar. The sample is placed in one arm of an optical interferometer and the other arm scanned. The interference signal is detected by a direct detector and Fourier transformed thereafter to get the power spectral density of the sample in the THz range. FTS is a common technique used in studying molecular resonances. The advantage is the wide bandwidth, covering from THz into infrared. One disadvantage is the low spectral resolution, which limits its use in many cases. Better spectral resolution can be achieved by using tunable narrowband THz sources or detectors. Both FTS and narrowband THz spectroscopy are widely used in passive systems for monitoring thermal-emission lines of molecules, especially in astronomy.

THz time domain spectroscopy (THz-TDS) is a more recent implementation of THz spectroscopy, which was developed from the work in the 1980s at AT&T Bell Labs and the IBM T.J. Watson Research Center [119] [120]. THz-TDS generally use short electrical pulses of broadband THz radiation, typically generated by ultrafast laser pulses. The generated THz pulses are transmitted through or reflected by the sample. The change in the electric field intensity of the pulses over time is recorded, in a pump-probe setup. Unlike common optical spectroscopes, which measure the intensity of light at different frequencies, the THz time-domain spectroscopic technique directly measures the THz wave's temporal electric field. Fourier transformations of this time-domain data gives the amplitude and phase of the THz wave pulse, therefore providing the real and imaginary

parts of the dielectric constant without the use of the Kramers-Kronig relations. This allows precise measurements of the refractive index and absorption coefficient of samples that interact with the THz waves. Many rotational and vibrational spectra of various liquid and gas molecules lie within the THz frequency band, and their unique resonance lines in the THz wave spectrum allow us to identify their molecular structures. Raman spectroscopy directly uses the frequency domain to fingerprint the lattice vibrations. Similarly, THz wave spectroscopy describes molecular rotational and vibrational spectra from 10 GHz to 10 THz using the real and imaginary parts of the dielectric function, obtained by measuring the THz wave in the time-domain. This is not possible by any current optical or microwave technique. This is one of the reasons that THz-TDS is attracting so much interest. THZ-TDS also has the advantage of broad frequency coverage, from a few hundred gigahertz to several THz. Although it has the problem of low spectral brightness and low spectral resolution, it provides useful information on specific frequency bands where various materials have responses.

6.2 Broad Band Terahertz Radiation Generation and Detection

THz sources and detectors are two main issues still attracting much interest. The aim is to produce high-power/sensitive, low cost, portable, room-temperature systems easy to be used in the field. Advances in ultrafast laser technology, material science and high-speed electronics are constantly providing new candidate THz sources and detectors. The following two parts will briefly summarize the current status of THz sources and detection methods.

THz sources can be broadly classified as incoherent thermal sources, broad band THz sources and narrow band continuous-wave sources. Thermal sources are easy to obtain but are weak in power. Narrow band THz generation is useful for high resolution spectroscopy applications and has potential application in telecommunications. It can be generated by up conversion of lower frequency microwave oscillators such as voltage-controlled oscillators and dielectric-resonator oscillators for low power radiation. [121]. Extremely high power THz emission has recently been demonstrated using free-electron lasers with energy-recovering linear accelerators. [122]. A number of optical techniques are also employed for narrow band THz radiation. The early implementation is by non-linear photomixing of two frequency-offset lasers or different modes from one laser [123]. Further techniques include optical parametric generators [124], and quantum cascade lasers [125].

Broadband pulsed THz sources are generally based on ultrashort laser pulses interaction with different materials, and will be the main topic of the following sections of this chapter. Many mechanisms have been proposed for broadband THz emission generation, among them photoconduction and optical rectification are the two most common ones.

6.2.1 Photoconductive THz Emitters

After the pioneering work by Lee et al. [96], Auston et al. [97], and Mourou et al. [99], the technique for generating pulsed terahertz (THz) radiation using femtosecond laser pulses and photoconductivity has been studied intensively. Currently it is one of the most common methods to generate and detect THz fields.

When an incoming laser pulse with photon energy above the band gap excites a biased semiconductor, free electrons and holes are produced in the conduction and valence band respectively. The rapid changes of the excess carrier concentration and their acceleration due to the applied dc bias produce an electromagnetic field radiating into free-space with the help of an antenna. Finally, the photo excited free carriers are trapped or recombined and the current density returns to its steady value.

The antenna is generally integrated on a photoconductor, which has a very short carrier lifetime, in the form of a photoconductive switch. The photoconductors used for this purpose are referred to as semi-insulating semiconductors, which are intrinsic semiconductors being processed by annealing, ion implantation or radiation exposure, etc., to reduce the carrier lifetimes to sub-ps. The most used are radiation damaged silicon on sapphire (SOS), InP bombarded with He ions and more recently, LT-GaAs. Of them, LT-GaAs is widely used these days, and more recently, organic polymers [126] are also used for this purpose.

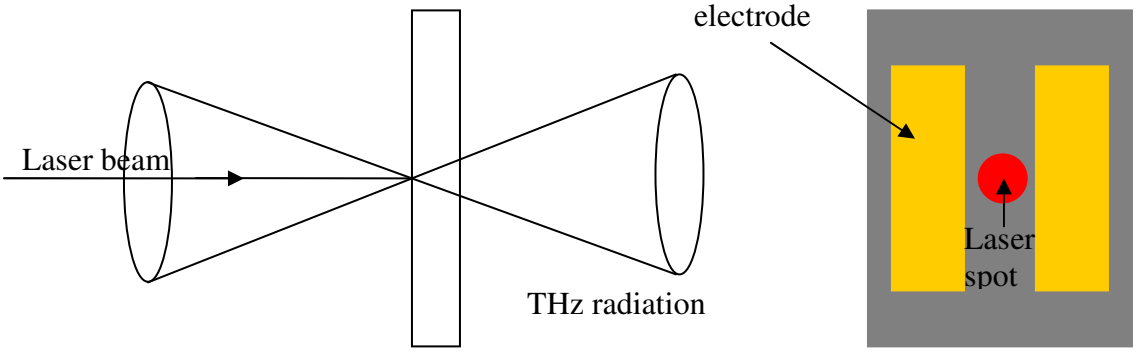

Figure 6.2 THz radiation from photoconductive antenna

The optical induced electromagnetic radiation can be described by a simple Hertzian dipole $p(t)$ when the carrier velocity is much slower than the light speed. The electric field at distance r and angle relative to the dipole (charged particle) axis, is then [112]

$$E(r,\theta,t) = \frac{1}{4\pi\varepsilon}\left(\frac{1}{r^3}p(t) + \frac{n}{cr^2}\dot{p}(t) + \frac{n^2}{c^2 r}\ddot{p}(t)\right)\sin\theta \ , \tag{6.1}$$

where $n = \sqrt{\varepsilon/\varepsilon_0}$ is the index of refraction of the medium between the two dipoles; c is the velocity of light, The first term can be identified as the quasistatic field, the second as the near field term and the third one as the far field radiated term. Since the far field term varies with r^{-1}, it will dominate when the distance is far from the source. The radiated THz magnitude can be estimated by Eq (6.1) based on the fact that the first derivative of the dipole moment is equal to the product of the photocurrent in the gap and the length of the gap.

$$E(t) = \frac{\mu_0}{4\pi r}\dot{I}(t) \tag{6.2}$$

The photocurrent has a rapid rise time due to the femtoseconds excitation laser pulse, and decays also rapidly due to carrier capture at traps, so the radiated THz wave should have a bipolar shape with a positive component having an amplitude proportional to the photocurrent rise time followed by a negative component proportional to the decay time.

THz photoconductive switch performance is determined mainly by 1) the optical pulse duration 2) the semiconductor substrates (short carrier lifetime, high mobility) and 3) antenna geometry. Detailed discussions can be found in [127].

6.2.2 Broad Band THz Generation Using Optical Rectification

Optical rectification is a second-order nonlinear optical effect. It is essentially a difference-frequency generation process, with the frequency difference nearly zero. So the generated waveform in this process is the envelope of the ultrafast optical pulse which excites the electro-optical materials.

Optical rectification takes place in noncentrosymmetric materials. It can be seen as a process inverse to the electro-optic effect (Pockels Effect). The physical mechanism involves the production of a transient polarization *P(t)* by the femtosecond optical pulses illuminating the materials. The THz radiation is proportional to the second time derivative of the induced polarization.

$$P^{(2)}(t) = \chi^{(2)} E_{opt}(t) E_{opt}(t) \tag{6.3}$$

$$P_{THz} \propto \frac{\partial^2 P^{(2)}(t)}{\partial t^2} \tag{6.4}$$

The Materials suitable for this method include LiNbO3, LaTiO3, zinc-blend semiconductors, organic crystals (DAST), and organic polymers. Among these Zinc-blend semiconductor is the most commonly used for THz generation/detection by optical rectification.

The value of the generated optical rectification signal depends on the magnitude of the nonlinear coefficient and phase matching condition. Phase matching is a key problem in most nonlinear optical processes because it maximizes the interaction between excitation beam and generated beam in the nonlinear materials, so as to enhance the efficiency of THz generation in this case. In general, the coherence length is inversely proportional to the difference of the optical group index and the THz refractive index. Taking into account material dispersion, the coherence length is expressed as:

$$l_c = \frac{\pi}{\Delta k} = \frac{\pi c}{\omega_{THz}\left| n_{opt} - \lambda_{opt}(\frac{\partial n_{opt}}{\partial \lambda})_{\lambda_{opt}} - n_{THz} \right|} \tag{6.5}$$

where n_{opt} and n_{THz} are the refractive indices at the optical and THz frequencies, respectively. Long coherence length can be obtained by either birefringence or angle tuning in noncollinear configurations. Another factor to be considered, sometimes more important than the radiation amplitude, is the bandwidth. It is mainly determined by the excitation laser pulse width and phasematching conditions. Using shorter laser pulse and thinner EO crystal can help obtain broader band emission.

6.2.3 Broadband THz Detection

THz detection is a difficult task since the radiated power of THz power emitter is weak. Moreover, due to the low photon energies of THz band (1-10meV), ambient thermal noise prevails over the THz signal and cooling of detectors is usually required. THz detectors can work as general optical detectors to measure light intensity at particular frequency. For broadband THz radiation, it is also possible to reconstruct through photoconductive or electro optic gating the shape of its electric field, i.e., both amplitude and phase of the generated electromagnetic pulse can be obtained.

The first phase-sensitive THz detector was in photoconductive (PC) antenna form [112], which was built on the same piece of material as the THz emitter. The presence of free space detection is a boost to the use and development of THz field. Nowadays, the freely propagating THz radiation is detected mainly by two methods: photoconductive sampling by gated photoconductive antennas [128] and free-space electro optic sampling

[129]. Techniques that do not provide phase information, such as bolometric and autocorrelation methods, are used rarely [130].

Both detection methods, photoconductive sampling and EO sampling, are coherent methods. At low frequency modulation, the PC sampling method has a better S/N ratio and sensitivity. When the modulation frequency is over 1MHz, the performance of EO sampling becomes comparable [131]. Free space EO sampling is able to detect signals in a wide bandwidth, from 0.1THz to 37 THz, while PC sampling is limited to 3-4THz due to antenna parameters [132].

6.3 THz Generation by Optical Rectification Using Poled Polymers

A wide range of nonlinear optical materials have shown the ability to generate THz radiation by optical rectification, from the most popular ZnTe [133] to the organic crystal DAST [134]. Recently several groups reported THz radiation generation using polymeric materials [106] [107]. Poled polymers can possess a large electro-optic coefficient. An EO coefficient as high as 120 pm/V was reported [135], compared to the 4pm/V of ZnTe and 77pm/V of DAST at 800nm. Moreover, EO polymers have low dielectric constants in the THz regime, which makes the phase matching between THz wave and optical pump wave better.

In this chapter, we explore THz generation and detection using a guest/host poled polymers. Experimental results contains: 1. Generation and detection of THz radiation using poled polymer; 2. Power dependence; 3. Pump laser spot size effects on THz radiation; 4. Compare polymer with ZnTe; 5. Applications.

6.3.1 Experiment Description

The polymer used in the THz generation is a guest-host polymer, i.e., it has two components, a guest chromophore and a polymer matrix host. Commonly used polymer matrices include PMMA, polystyrene, polycarbonate, and APC. Fig. 6.3 listed several chromophores and the corresponding dipole moments. The detailed description can be found in Hayden's papers [107], [108], [109].

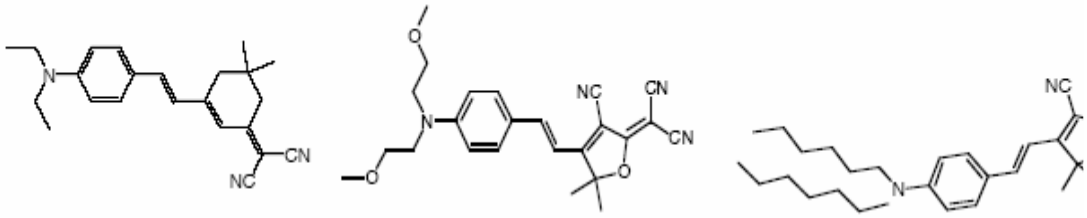

Lemke
μ =8.31 Debye,

DCDHF-MOE-V
μ = 12.3 Debye,
FOM = 1.9 x Lemke

DCDHF-6-V
μ = 12.7 Debye,
FOM = 1.7 x Lemke

Figure 6.3 Chromophores and corresponding dipole moments μ

Chromophores process large dipole moments and are key to the electro-optical performance of the polymer materials. In natural polymers the chromophores are randomly oriented so that the dipole moments cancel each other, leading to a centrosymmetric structure, so that the 2^{nd} –order nonlinear optical susceptibility is zero. Chromophores can be aligned by poling by applying a high voltage when heated above glass transition temperature, resulting in a large EO coefficient. Poled polymers with higher chromophore concentration have correspondingly higher EO coefficient. But increased chromophore concentration causes a decrease of the glass transition

temperature of the composite because the chromophore acts as a plasticizer for the host [108]. Thus there is always a trade off between the EO coefficient and thermal stability of the polymer composite. Thermal vibrations tend to randomize the chromophores and weaken the non-linear properties over time. Polymers with higher glass transition temperature will have better stability.

The polymer used in this experiment has a CLD-1 type chromophore[136] doped in amorphous polycarbonate host, which was spincoated onto a microscope slide and subsequently corona poled to align the chromophores and enable second-order nonlinear optical effects. The polymer has a thickness of 7μm.

THz pulses were generated by illuminating the polymer with 180fs laser pulses at a wavelength of 800nm from a Coherent RegA9000 laser amplifier. The pump laser was not focused and an average power of ~100mW was incident on the polymer for most of the measurements. The incidence angle was set to be 50^{o} for better signal to noise ratio. The experiment layout is shown in Fig. 6.4.

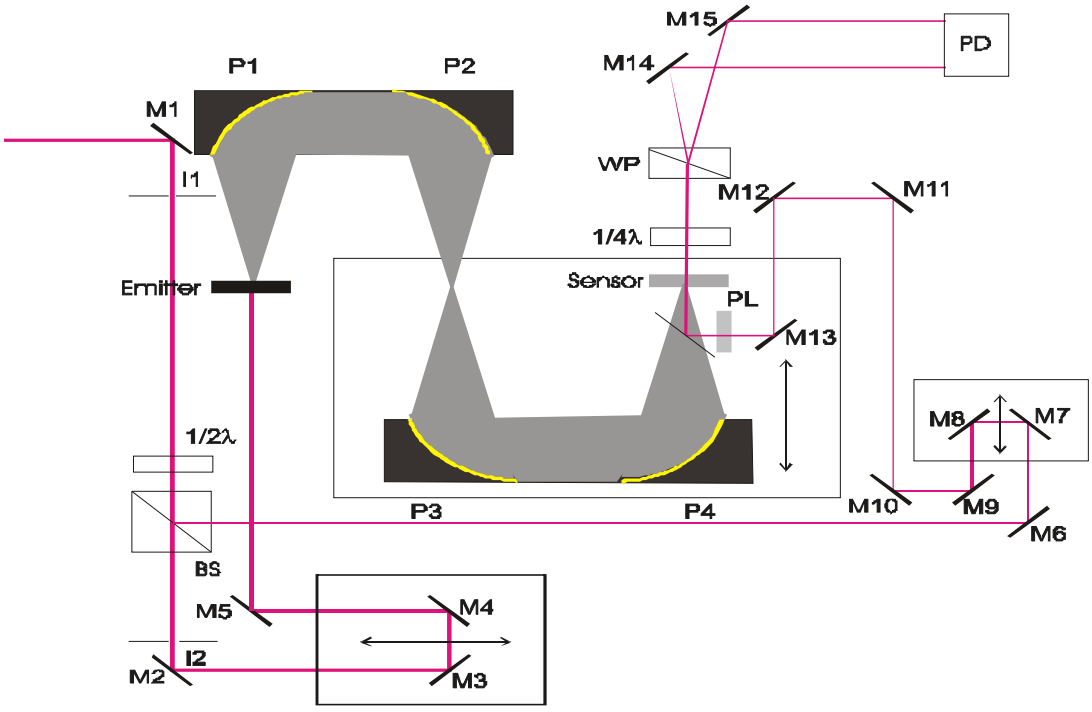

Figure 6.4 Experimental layout for THz generation and detection.

The components in the setup are: P1-P4: parabolic mirrors; M1-M15: flat reflecting mirrors; I1, I2: apertures; BS: beam splitter; WP: Wollaston prism; PD: balanced photodetector; Emitter: poled polymer.

The laser beam is split into two by a beam splitter (BS): one for pump and one for probe, with a 0.95/0.05 transmittance/reflectance ratio. The pump beam travels through an optical delay line via M3, 4 and is loosely focused on the emitter, which has a non-zero angle of incidence. The generated THz beam passes to the parabolic mirrors and is focused on the THz sensor, either a ZnTe crystal or a poled polymer in this experiment. The probe beam is designed to go collinearly after reflecting from a pellicle beam splitter sitting in the THz path. The polarization state of the probe beam is affected by the

presence of the THz radiation in the THz sensor. The probe beam passes the sensor and is split into two by a Wollaston prism, then detected by a balanced detector, which is a typical configuration of EO sampling.

6.3.2 THz Pulse and Spectrum

The temporal waveform of the THz radiation from poled polymer is shown in Fig. 6.5 (a). The measured pulse is the convolution of the radiation with the detector response, so the actual waveform is broadened by the detector. The radiation pulse has one and half cycle in the main pulse, due to the fact that the radiation is the 2^{nd} derivative of the rectification dipole.

Figure 6.5(b) is the spectrum of the THz radiation obtained by Fourier transform of the temporal waveform. It can be seen that the center frequency is close to 1THz while up to 2.2 THz there is still usable energy.

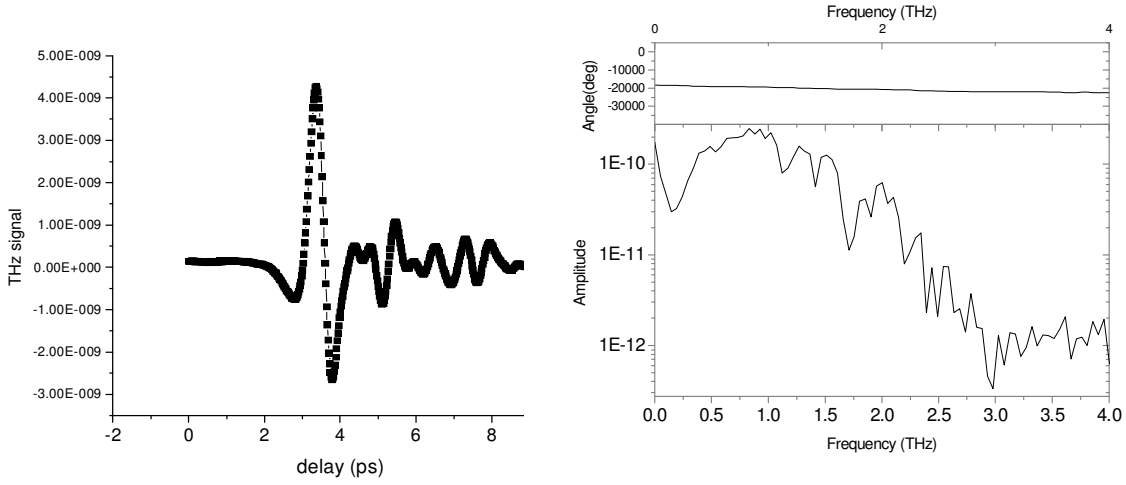

(a) (b)

Figure 6.5 (a) THz pulse shape and (b) corresponding spectrum by Fourier Transform.

6.3.3 Comparison with ZnCdTe

ZnCdTe was used as a THz emitter to calibrate the THz signal generated with the poled polymer. The waveforms are illustrated in Fig. 6.6. Table 6-1 summarized the data from both emitters. The ratio of the THz pulse amplitude from ZnCdTe to poled polymer is 1.41. The ZnCdTe crystal is 117um thick, while the polymer is 7um thick. At 1THz, both of them have a coherence length over 100um. We can thus estimate the effective EO coefficient of the polymer with the following equation:

$$\frac{l_{ZnCdTe} \bullet \gamma_{41}}{1.41 \bullet l_{polymer}} = \frac{117 \bullet 4}{1.41 \bullet 7} = 47.4\, pm/V \qquad (6.6)$$

where l_{zncdte} and $l_{polymer}$ are the thickness of ZnCdTe and the poled polymer, respectively.

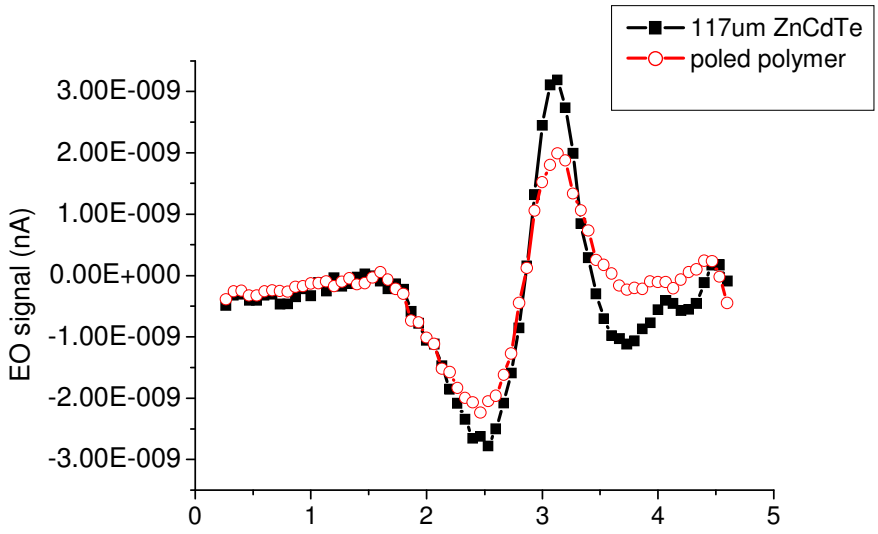

Figure 6.6 Comparison of THz generation from poled polymer and ZnCdTe

	P+	P-	P-P	ratio
ZnCdTe	3.242	-2.726	5.968	1.41
Poled polymer	1.946	-2.238	4.225	1

Table 6-1 Summary of the data of Fig 6.6

6.3.4 Laser Power Dependence of THz Radiation

THz signal is measured by EO sampling. The probe beam is separated into two by a Wollaston prism and the two beams are set at equal values by a quarter-wave plate. A balanced detector detects these two beams. Without THz signal, the reading of the lock-in amplifier is close to zero. When THz signal arrives, it induces birefringence in the EO crystal and breaks the balance in the detectors. For balanced detection, the difference between these two beams is measured, which can be expressed as [137]:

$$I_{signal} = I_0 \frac{\pi d n^3 \gamma_{41}}{\lambda} E \qquad (6.7)$$

where d is the thickness of the EO crystal, n is the refractive index of the crystal at the wavelength of the probe beam, λ is the probe wavelength, γ_{41} is the EO coefficient, I_0 is the probe light intensity and E is the electric field of the THz pulse.

It can be seen that the measured THz signal is proportional to probe beam intensity and THz electric field amplitude. So for balanced EO measurement, the direct results show the electric field of the THz beam instead of the power of THz radiation.

In Fig. 6.7(a), the peak THz signal showed a linear relation with the incident laser power for pump power up to 120mW, corresponding to a fluence of 0.3mJ/cm^2 when assuming a 1 mm^2 laser spot. No saturation has been seen due to the limitation of

available laser power. This is typical of 2nd order nonlinear process considering what we are measuring is the electric field instead of power of the radiation. THz power is the square of electric field so the radiation power dependence on pump power is a square relation, as in any 2nd order process. The probe power dependence is shown in Fig.6.7 (b), which also presents a good linear relationship. This linear dependence is easy to understand (Eq. 6.7) and it is important for the system to operate in the linear region to get reasonable THz signal measurements. EO sampling requires very little probe power, which helps keep the linearity working condition of the sensor.

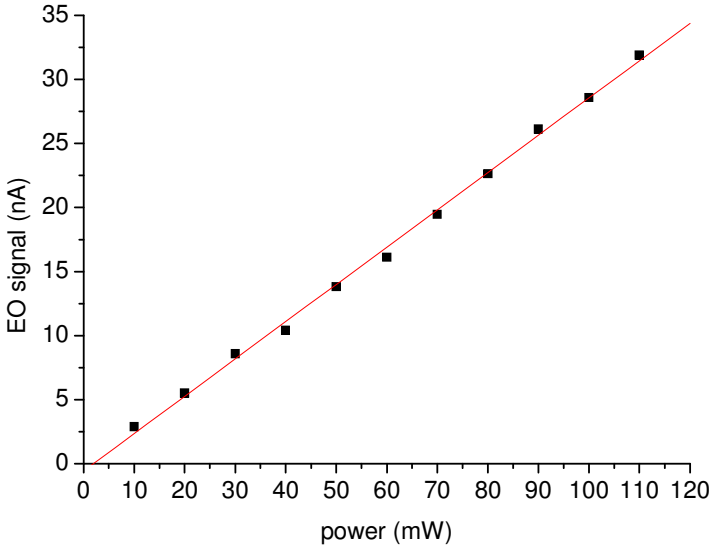

(a)

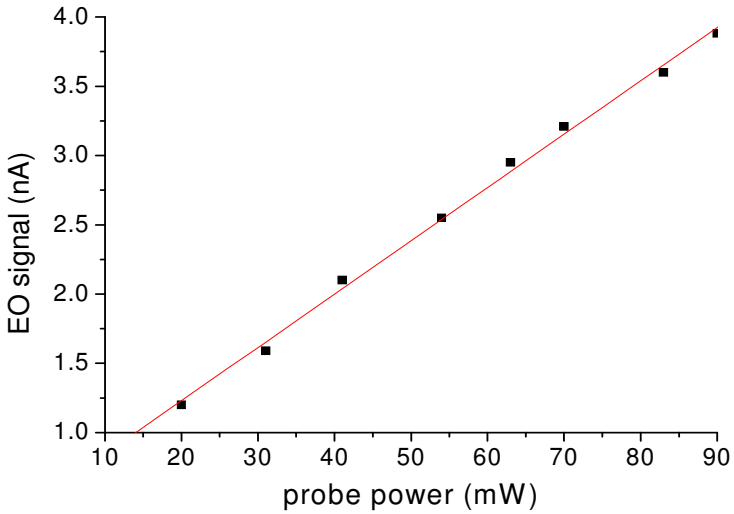

(b)

Figure 6.7 THz signal dependence on (a) pump laser power and (b) probe laser power.

6.3.5 THz Radiation Power and Excitation Laser Spot Size

THz generation by optical rectification has the unique advantage of extremely broad spectral bandwidth. But the conversion efficiency obtained with optical rectification is not as high as that obtained with biased photoconductive switches. Increasing pump laser power will greatly increase THz radiation power. From section 6.3.4 we see that THz power increases quadratically with pump laser power in with a large dynamic range. With a certain amount of pump laser power, higher THz radiation power is always desirable. This requires increasing the conversion efficiency from laser power to THz radiation.

One way to increase optical to THz conversion efficiency is by focusing the pump laser beam. The THz intensity can be expressed as:

$$I_{THz} \propto I_0^2 \tag{6.8}$$

where I_{THz} is the intensity of THz radiation generated by second-order nonlinear optical processes within the EO crystal and I_0 is the incident optical intensity of the pump laser on the EO crystal. The optical power (P_0) is a constant, and its relation with I_0 is:

$$P_0 \propto I_0 \cdot r^2 \tag{6.9}$$

where r is the laser spot radius on the EO crystal.

The radiated THz power can be expressed:

$$P_{THz} = \eta_{diff} I_{THz} S \tag{6.10}$$

where S is the THz source area, η_{diff} is a dimensionless diffraction coefficient caused by the limited size of THz source. When the source is much larger than THz wavelength, η_{diff} ~1.

From (6.8)-(6.10), the relation between radiated THz power and incident pump laser power can be related as:

$$P_{THz} \propto P_0^2 / r^2 \tag{6.11}$$

So when no diffraction effect considered, the radiated THz power is inversely proportional to the size of the incident laser beam at a fixed pump laser power. It is obvious that focusing the laser beam is a method to increase the THz conversion efficiency. But when the radiation source is too small (sub-wavelength), the diffraction can not be ignored. Bethe's calculation predicts that radiation from a sub-wavelength source follow the relation [138]:

$$S = E \times H = \frac{k^4 r^4}{R^2} \cdot const \tag{6.12}$$

where r is the aperture radius and R is the distance between observing point and the source. And the *const* is proportionally related to the incident laser power. The diffraction efficiency was contributed by the product of k, r, and can be separately expressed as:

$$\eta_{diff} \propto k^4 r^4 \tag{6.13}$$

Thus when radiation source is small, the radiated THz power becomes:

$$P_{THz} \propto \eta_{diff} P_0^2 r^{-2} \propto P_0^2 r^2 \tag{6.14}$$

It can be seen that the smaller the source radius is, the smaller the THz power can be detected in the far field. So their exits an optimized radiation size: when the actual source size is larger than this optimized size, optical power are not used fully; when the actually source is smaller than this optimized size, diffraction prevents the propagation of THz energy to the far field. This relation was explored in GaAs and the THz source that gave the maximum radiated power was found to be close to THz wavelength [30]. The

following part we will discuss our experimental exploration of the THz power dependence on the size of THz source using poled organic polymer as EO media.

The experiment on the relationship between THz power and incident laser beam spot size was carried out using the same setup as in Fig. 6.4. The pump laser beam was unfocused. The size of beam on the polymer was controlled by a series of apertures ranging from 200 μm to 1mm. The pump laser power on the sample was kept constant, and the signal was detected at far field after the parabolic reflectors. The measured signal from the lock-in amplifier is squared and multiplied by the aperture area to be converted into power of the THz radiation. The THz signal vs. laser spot size was shown in Fig. 6.8.

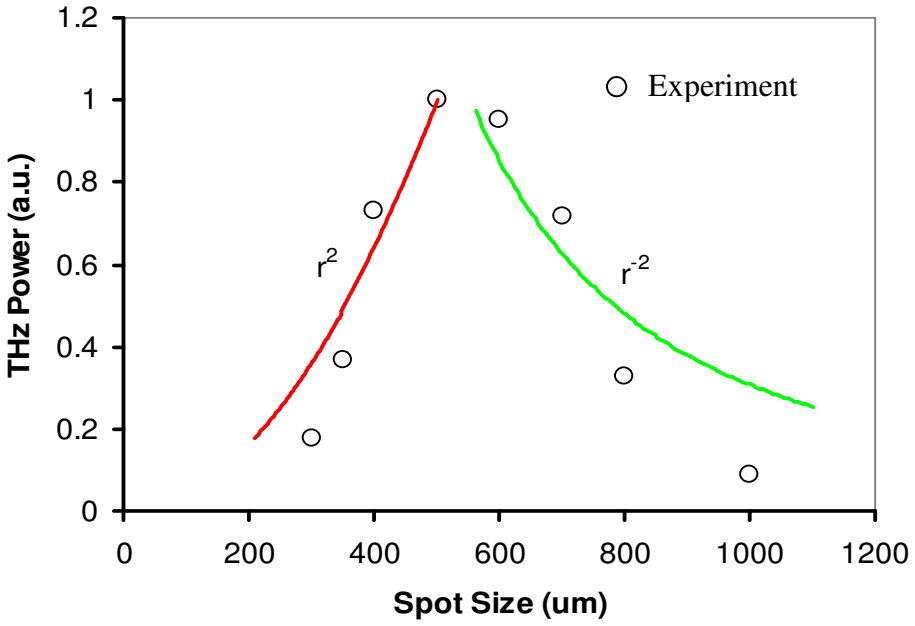

Figure 6.8 THz power vs. the radius of rectification area on the polymer surface

The circles in Fig. 6.8 are experimental data, and the curves are theoretically fitted curve. At a constant pump power level, when the spot size is close to the THz center wavelength (~600GHz), the radiated THz power reaches maximum. Increasing or

decreasing the spot size on the polymer both cause the total power both to reduce. In results shown in Fig. 6.8 gives a clue of achieving best performance of THz radiation power. For different spot size, the center frequency and spectral bandwidth of the THz didn't show much difference.

6.4 Applications of THz Radiation

6.4.1 TDS of Polymers

Transmission and absorption spectrum of Norland Optical Adhesive (NOA) series polymers were measured as an example of the application of the THz radiation.

First we show the results on NOA 63. NOA 63 is a clear, colorless, liquid photopolymer that will cure when exposed to ultraviolet light. It offers many advantages in bonding of optical elements where the bonding surface can be exposed to light. The use of NOA 63 eliminates premixing, drying, or heat curing operations common to other optical adhesive systems. Curing time is remarkably fast, and is dependent upon the thickness applied and the amount of ultraviolet light energy available. Due to the above mentioned advantages, it is proposed to be used as a candidate material for THz waveguide. Our measurements below disclose the transmission/absorption properties of NOA series polymers in THz range.

The experiment setup is illustrated in Fig. 6.4. The sample was placed at the focal point between two parabolic mirrors P2 and P3. THz wave form were scanned before the polymer was put in and recorded as a reference. And then the waveform of the glass container for NOA 63 was measured. In the last round, THz waveform after NOA63 in

the container was measured. For each case the waveform was Fourier transformed to get the spectral response. The results are shown in Fig. 6.9.

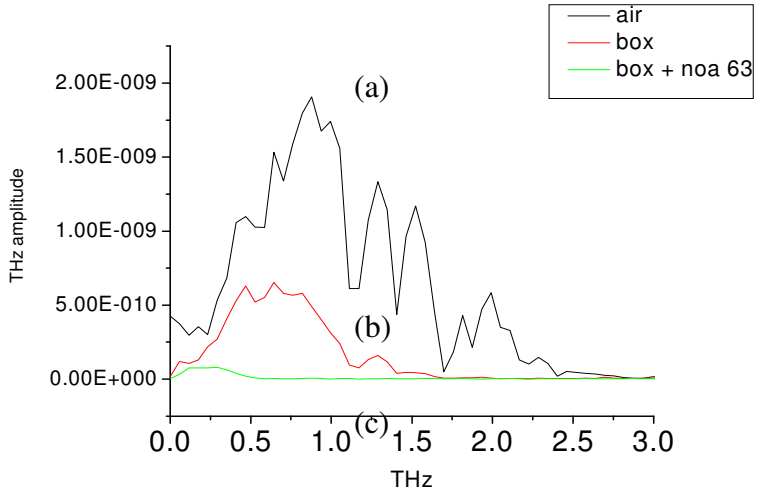

Figure 6.9 Experimental data of (a) THz spectrum in air, (b) after empty box and (c) after box with NOA63 inside

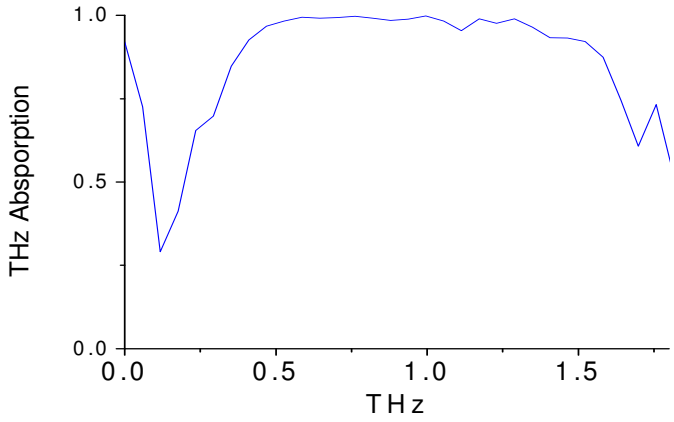

Figure 6.10 Normalized absorption spectrum of NOA63 in THz ranged

To extract the absorption properties of the polymer, we normalized the difference of curve (b) and curve (c) by curve (b) to get the absorption spectrum of NOA 63 without

influence of the container and the frequency distribution of THZ source. The results are illustrated in Fig. 6.10.

It can be seen that the highest transmission happens at frequency around 100GHz. At frequencies above 500GHz, most of the THz energy was absorbed by the polymer. The large oscillation after 1.7THz is noise instead of real signal. The container we used for this measurement strongly absorbs THz above 1.7THz so after this point the data is not reliable. It turns out that NOA 63 is not suitable for THz waveguide fabrication as indicated by our measurements.

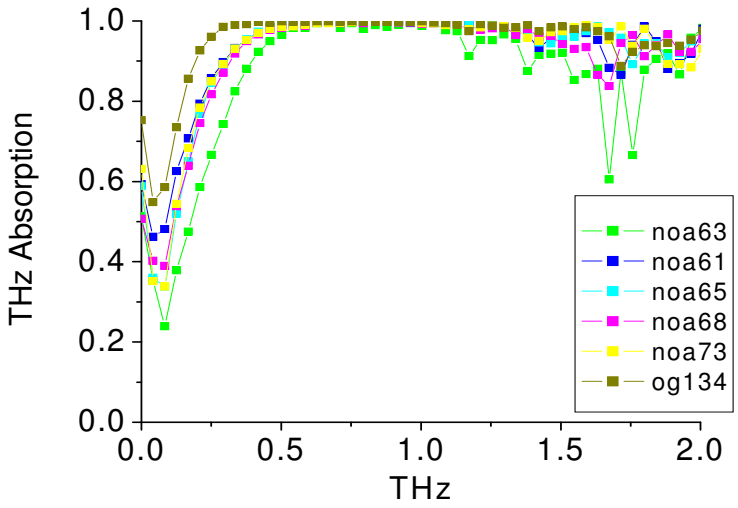

Figure 6.11 THz absorption spectrum of photopolymers NOA 61, 63, 65, 68, 73, and OG134

Some other NOA polymers are tested for the THz absorption. The results are illustrated in Fig. 6.11. All of the polymers showed strong absorption in 500GHz to 1.5THz range.

6.4.2 Paper Counting by Measuring Delay Time of THz Pulse

THz can penetrate many materials invisible to human eyes, which is one of the main impetuses for THz research nowadays. By measuring the amplitude, timing and shape of the THz pulse after the materials can give us information about the materials THz spectral response and geometrical information.

We measured THz waveform after A4 print paper and used the time delay of THz pulse to count the number of papers. The THz waveforms are illustrated in Fig. 6.12. The time delay caused by each page of paper is 134fs in our experiment. The blue curve is the THz waveform after an unknown number of papers. The delay relative to the THz waveform in air (black) was measured to be 27ps, yielding the number of pages to be 20, which is confirmed by manual counting.

After we know the geometrical thickness of a page of paper, we can calculate the refraction index of the paper at the THz center wavelength. It can be measured that one page of A4 paper we used is 100μm thick, so the refraction index is around 1.40.

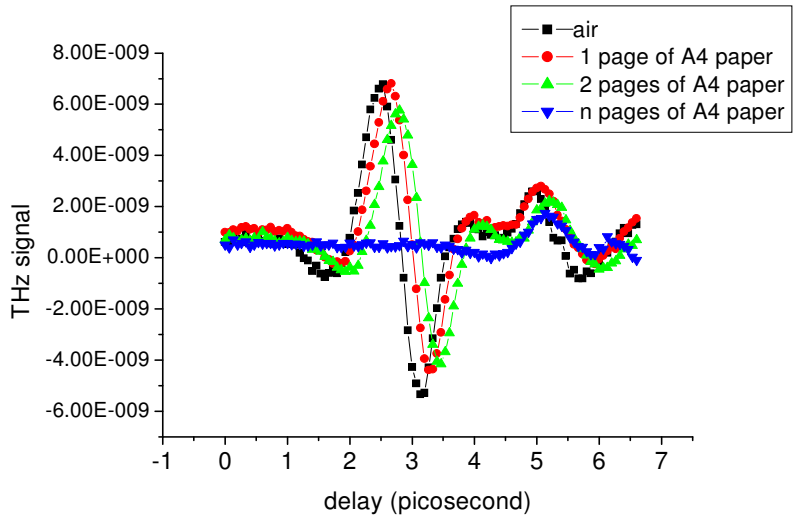

Figure 6.12 Counting paper using THz pulses: THz waveform after different temporal delay induced by paper in the beam path.

6.5 Conclusions

In this chapter we studied the generation and detection of THz radiation from a novel poled guest-host polymer. EO polymers as THz emitters have the advantages of high EO coefficients and longer coherence length. They are promising materials to increase the spectral response and signal-to-noise ratio of THz systems. We demonstrated the application of EO polymer both as THz emitter and sensor in this chapter. By measuring the power dependence on pump laser power and probe laser power, an optimized working point can be determined for the THz system. The polymer emitter was compared with a commercial ZnCdTe crystal for an estimate of the EO coefficient. Finally, THz power dependence on the pump laser spot size was determined. By systematically studying the THz generation and the determination factors, a good understand of the THz mechanism and operating condition is obtained, providing a basis for future work on THz time domain spectroscopy and THz waveguide propagation. Finally, a NOA photopolymer absorption spectrum was measured in the THz spectral range.

Chapter 7: Conclusions and Future Work

In this thesis we have examined and explored the near-field second harmonic imaging of ferroelectric thin films and NLO polymer films and studied the ultrafast photocarrier generation in conjugated polymers and THz radiation from EO polymers.

We first investigated high resolution imaging of ferroelectric thin films. We employed NSOM to map the near-field second harmonic distribution on ferroelectric films which is related to the ferroelectric domain polarizations. The relation between the ferroelectric polarization and local SHG intensity was established using a single crystal $BaTiO_3$. We found that for different orientations of the crystal, the local SH intensity's dependence on the incident light polarization showed different symmetries and signal levels. Near-field SH images of 80nm resolution was achieved on PZT thin films together with the film surface topology. The contrast and gray scale of the SH image have been successfully explained using the relations between near-field SH intensity with polarization directions established using the single crystal. We then investigated local field enhancement by uncoated tapered fiber tip in near-field SHG to account for the high resolution of the SH images. We also investigated the dependence of local SHG on polarization of incident light at different spot of the film as evidence for the SHG and polarization relationships.

We then investigated near-field SH mapping of two types of NLO polymers: SPECH/PAA and C2CMA. Both transmission and reflection mode NSOM were used to study the near-field nonlinear optical properties of the polymers. Because of the extremely weak signal when collecting by a nano-size probe, the signal-to-noise ratio was

low. Scanning by NSOM gave clear topography but SH distribution on the polymer films showed no significant features relating to the topology.

We studied the carrier life time and mobility in conjugated polymers. We first measured the width of electric pulse generated from an MPM switch fabricated on BAMH-PPV using photoconductive sampling. The pulswidth was measured to be 2ps. A transient photocarrier mobility of ~500cm^2/V was estimated based on a quantum efficiency of 0.05%. We then implemented photoconductive sampling on a single-switch device fabricated on MEH-PPV and achieved sub-picosecond temporal resolution due to the reduced capacitance. This is the fastest electric pulse generated and measured on semiconducting polymer up to now, providing proof of high transient mobility in semiconducting polymers. Finally we measured transient reflectivity on MEH-PPV and obtained a carrier life time comparable to that obtained by single-switch photoconductive sampling. Carrier generation and recombination in polymers is more complicated than that in inorganic semiconductors. Different morphology may result in different carrier mobility. A controlled study of the relation between polymer morphology and carrier dynamics, i.e., interchain and intrachain behavior of the carriers, will be fruitful. A measurement on the photoluminescence on a similar time scale or faster will help disclose more information on the carrier generation process.

We also studied the THz generation and detection using EO polymers by optical rectification, or differential frequency generation. THz performance was compared with a commercial ZnCdTe to roughly estimate the electro-optic (EO) coefficient of the polymer material. We demonstrated THz power dependence on excitation laser spot size on polymer film. An optimized pump laser spot size exists around the THz radiation

wavelength. This provides us with guidance to extract higher THz radiation power with a finite pump laser power. EO polymers are promising materials for THz generation and detection due to their high electro-optic coefficients and good phase-matching conditions. Using materials with higher EO coefficient, THz generation efficiency and SNR can be greatly increased. Generating THz radiation using polymer waveguide will also give more THz energy due to the long coherence length.

Bibliography

[1] M. A. Paesler, P. J. Moyer, *Near-field Optics: Theory, Instrumentation, and Application*. New York, John Wiley & Sons, Inc, 1996

[2] D. Courjon, *Near-field Microscopy and Near-field Optics*, London, Imperial College Press, 2003

[3] C. J. Chen, *Introduction to Scanning Tunneling Microscopy*. New York, Oxford University Press, 1993.

[4] D. Sarid, *Scanning Force Mciroscopy with Applications to Electric, Magnetic and Atomic Forces*. New York, Oxford University Press, 1994

[5] M. Daglish, T. Kemmitt, "Ferroelectric thin films-research, development and commercialization". *IPENZ Transactions*, **27**, 21-24 (2000)

[6] M. Suzuki, "Review on future ferroelectric nonvolatile memory: FeRAM-from the point of view of epitaxial oxide thin films", *Journal of the Ceramic Society of Japan*, **103**, 1099-1111, (1995)

[7] E. Fujii, T. Otsuki, T. Sumi, N. Moriwaki, "Ferroelectric memory technology". *National Technical Report*, **41**, 94-100, (1995)

[8] N. Neumann, R. Kohler, G. Hofmann, "Infrared sensor based on the monolithic structure Si-P(VDF/TRrFE)", *Ferroelectrics*, **171**, 225-238, (1995)

[9] F. Jona, G. Shirane, *Ferroelectric Crystals*, Dover Publications, 1993

[10] O. Kolosov, A. Gruverman, J. Hatano, K. Takahashi, "Nanoscale visualization and control of ferroelectric domains by atomic force microscopy". *Phys. Rev. Lett.*, **74**, 4309-4312 (1995)

[11] F. Laurell, M. G. Roelofs, W. Bindloss, H. Hsiung, "Detection of ferroelectric domain reversal in $KTiOPO_4$ waveguides". *J. of Appl. Phys.*, **71**, 4664-4670, (1992)

[12] R.W. Boyd, *Nonlinear Optics*, Academic Press, London, 1992

[13] Y. R. Shen, "Surface properties probed by second-harmonic and sum-frequency generation". *Nature*, **337**, 519-525, (1989)

[14] S. Kurimura and Y. Uesu, "Application of the second harmonic generation microscope to nondestructive observation of periodically poled ferroelectric domains in quasi-phase-matched wavelength converters". *J. Appl. Phys.* **81**, 369-375, (1997)

[15] Y. Uesu, S. Kurimura, and Y. Yamamoto, "Optical second harmonic images of 90 degrees domain structure in $BaTiO_3$ and periodically inverted antiparallel domains in $LiTaO_3$". *Appl. Phys. Lett*. **66,** 2165-2167, (1995)

[16] V. Kirilyuk, A. Kirilyuk and Th. Rasing. "A combined nonlinear and linear magneto-optical microscopy" *Appl. Phys. Lett.* **70,** 2306-2308, (1997)

[17] T. J. Yang, U. Mohideen and M.C. Gupta., "Near-field scanning optical microscopy of ferroelectric domain walls" *Appl. Phys. Lett.* **71,** 1960-1962, (1997)

[18] S. I. Bozhevolnyi, K. Pedersen, T. Skettrup, X. Zhang; "Far- and near-field second-harmonic imaging of ferroelectric domain walls". *Optics Communications*, **152**, 221-224, (1998)

[19] M. Lee; J. Ju; S. Park; J. Do, "Polymer-based devices for optical communications". *ETRI Journal*, **24**, 259-269 (2002)

[20] Y. Shen*;* P. Markowicz, J.Winiarz, J. Swiatkiewicz, "Nanoscopic study of second-harmonic generation in organic crystals with collection-mode near-field scanning optical microscopy". *Optics Letters*, **26**, 725-727 (2001)

[21] R.D. Schaller; R. J. Saykally, Y. –R. Shen, F. Lagugne-Labarthet, "Poled polymer thin film gratings studied by near-field second harmonic optical microscopy and far-field optical diffraction". *Proceedings of the SPIE - The International Society for Optical Engineering*, **4991**, 305-312, (2003)

[22] T. Ito, H. Shirakawa, S. Ikeda, *J. Polym. Sci. Chem. Ed.*, *12,* 11. (1974)

[23] R. H. Friend, "Conjugated polymers: new material for optoelectronics", *Pure Appl. Chem*. **73**, 425-430 (2001)

[24] R. R. Chance, R. H. Baughman, P. J. Reucroft, K. Takahashi, "Transient photoconductivity of a polydiacetylene single crystal", *Chemical Physics*, **13**, 181-185 (1976)

[25] M. Weiter, V. I. Arkhipov, H. Bassler, "Transient photoconductivity in a thin film of a poly-phenylenevinylene-type conjugated polymer". *Synthetic Metals*, **141**, 165-170, (2004)

[26] D. Moses, H. Okumoto, C. H. Lee, and A. J. Heeger, "Mechanism of Carrier generation in poly(phenylene vinylene): Transient photoconductivity and photoluminescence at high electric field", *Phys. Rev. B*, **54**, 4748-4754, (1996)

[27] A. M. Almeida, M. M. Ramos, H. G. Correia, "Charge mobility in conjugated polymer molecules". *Computational Materials Science*, **27**, 128-132, (2003)

[28] . Fuchigami, H.; Tsumura, A.; Koezuka, H.; "Polythienylenevinylene thin-film transistor with high carrier mobility", *Appl. Phys. Lett*., **63**, 1372-1374 (1993)

[29] C. Lee*,* G. Yu, D. Moses, A. J. Heeger, "Picosecond transient photoconductivity in poly(p-phenylenevinylene)". *Phys. Rev. B*, **49**, 2396-2407, (1994)

[30] J. Xu, X. C. Zhang "Optical rectification in an area with a diameter comparable to or smaller than the center wavelength of terahertz radiation", *Opt. Lett.*, **27**, 1067-1069. (2002)

[31] E. Abbé, Archiv. *Mikroskopische Anat*. **9**, 413 (1873)

[32] E. H. Synge. "A suggested method for extending microscopic resolution into the ultramicroscopic region". *The London, Edinburgh, and Dublin Philosophical Magazine and Journal of Science*, **6, 7th** series: 356–362, (1928)

[33] E.A. Ash and G. Nicholls, "Super resolution aperture scanning microscope", Nature **237**, 510-513, (1972)

[34] D.W. Pohl, W. Denk and M. Lanz, "Optical stethoscopy: Image recording with resolution lambda /20", *Appl. Phys. Lett*. **44**, 651-653, (1984)

[35] E. Betzig, M. Isaacson and A. Lewis, "Collecting mode near-field scanning optical microscopy", *Appl. Phys. Lett*. **51**, 2088-2090, (1987)

[36] K. Lieberman, S. Harush, A. Lewis and R. Kopelman, "A light source smaller than the optical wavelength", *Science* **247**, 59-61, (1990)

[37] E. Betzig, J.K. Trautman, T.D. Harris, J.S. Weiner and R.L. Kostelak, "Breaking the diffraction barrier: optical microscopy on a nanometric scale", *Science* **251**, 1468-1470, (1991)

[38] E. Wolf and M. Nieto Vesperinas, "Analyticity of the angular spectrum amplitude of scattered fields and some of its consequences", *Journal of the optical Society of America A*, **2(6),** 886-889, (1985)

[39] D. Courjon and C. Bainier, "Near field microscopy and near field optics", *Reports on Progress in Physics*, **57**, 989-1028, (1994)

[40] Ch. Girard and A. Dereux, "Near-field optics theories", *Reports on Progress in Physics*, **59**, 657-699, (1996)

[41] E. Betzig, P.L.Finn, J. S. Weiner, "Combined shear force and near-field scanning optical microscopy", *Appl. Phys. Lett*. **60**, 2484-2486, (1992)

[42] R. Toledo-Crow, R. P. C. Yang, Y. Chen, and M. Vaez-Iravani, "Near-field differential scanning optical microscope with atomic force regulation", *Appl. Phys. Lett.* **60**, 2957, (1992)

[43] T.R.Albrech, P.Grutter, D. Horne and D. Rugar, "Frequency modulation detection using high-Q cantilevers for enhanced force microscope sensitivity" *J. Appl. Phys*, **69**, 668-673, (1991)

[44] C.J. Chen*, Introduction to Scanning Tunneling Microscopy*, New York: Oxford University Press, (1993)

[45] Y. Z. Shen, P. Markowicz, J. Winiarz, J. Swiatkiewicz, "Nanoscopic study of second-harmonic generation in organic crystals with collection-mode near-field scanning optical microscopy". *Optics Letters*, **26**, 725-727, (2001)

[46] R. Watton, "Ferroelectrics for infrared detection and imaging". ISAF '86. *Proceedings of the Sixth IEEE International Symposium on Applications of* Ferroelectrics, New York, NY, IEEE, 172-181, (1986)

[47] S. Zhou, C. Liang, C. A. Rogers, "Integration and design of piezoelectric patch actuators". *Journal of Intelligent Material Systems and Structures*, **6**, 125-133, 1995

[48] R. E. Jones, Jr "Integration of ferroelectric nonvolatile memories", *Solid State Technology*, **40**, 201-210, (1997)

[49] R. Ramesh, *Thin Film Ferroelectric Materials and Devices*, Kluwer Academic Publisher, Boston, (1997)

[50] K. Takahashi, and M. Takagi, "Topographic study on domain boundaries in TGS", *J. Phys. Soc. Jpn*. **44**, 1266-1274 (1978)

[51] N. Nakatani, K. Hayakawa, and H. Inouse, "Observation of domain structure in triglycine sulfate by a pyroelectric probe technique", *J Appl. Phys*. **34**, 5453-5456, (1995)

[52] P. M. Bridger, Z. Z. Bandic, E. C. Piquette, T. C. McGill, "Measurement of induced surface charges, contact potentials, and surface states in GaN by electric force microscopy". Applied Physics Letters, **74**, 3522-3524, (1999)

[53] C. S. Ganpule, V. Nagarajan, V., H. Li, A. S. Ogale, D. E. Steinhauer, S. Aggarwal, E. Williams, R .Ramesh, and P. DeWolf, "Role of 90 degrees domains in lead zirconate titanate thin films", *Appl. Phys. Lett*. **77** 292-294 (2000)

[54] P. A. Franken, A. E. Hill, C. W. Peters, G. Weinreich, "Generation of optical harmonics". *Phys. Rev. Lett.* **7**, 118-119, (1961)

[55] B. A. Nemet, V. Nikolenko, R. Yuste, "Second harmonic imaging of membrane potential of neurons with retinal", Journal of Biomedical Optics, **9**, 873-881, (2004)

[56] V. Kirilyuk, A. Kirilyuk, T. Rasing, "New mode of domain imaging: second harmonic generation microscopy". Journal of Applied Physics, **81**, 5014, (1997)

[57] Y. Kawata, C. Xu, and W. Denk, "Feasibility of molecular-resolution fluorescence near-field microscopy using multi-photon absorption and field enhancement near a sharp tip". *J. Applied Phys*. **85**, 1294 (1999)

[58]F. Zernike, and J. E. Midwinter, *Applied Nonlinear Optics*, Wiley, New York, (1973)

[59] L. Novotny, D. W. Pohl, , and B. Hecht, "Light confinement in scanning near-field optical microscopy" *Ultramicroscopy* **61**, 1-9, (1995)

[60] R.J. Pressley, *CRC handbook of lasers with selected data on optical technology*, The CRC, Cleveland, OH, 513, (1971)

[61] S. Singh, J. P. Remeika, and J. R. Potopowicz, *Nonlinear optical susceptibilities of ferroelectric lead titanate*, *OSA Spring Meeting*, Tuscon, AZ, (1971)

[62] S. P. Alpay, V. Nagarajan, L. A. Bendersky, M. D. Vaudin, "Effect of the electrode layer on the polydomain structure of epitaxial $PbZr_{0.2}Ti_{0.8}O_3$ thin films". *J Appl. Phys.*, **85**, 3271-3277, (1999)

[63] U. C. Oh, J. Ma, G. K. L. Wong, J. B. Ketterson, and J. H. Je, "Strain-induced second-harmonic generation in pseudocubic $Ba_{0.48}Sr_{0.52}TiO_3$ thin films". *Appl. Phys. Lett.* **76**, 1461-1463, (2000)

[64] G. A. Lindsay and K. D. Singer, Eds. *Polymers for Second-Order Nonlinear Optics*, ACS Symposium Series **601**. (1995)

[65] K. D. Singer, M. G. Kuzyk, and J. E. Sohn. *J. Opt. Soc. Am. B*, **4**, 968. (1987).

[66] H. Staudinger, *Ber. Deut. Chem. Ges.,* **53** 1073, (1920)

[67] J. H. Cheung, A. F. Fou, M. F. Rubner. *Thin Solid Films*, **224**, (1994)

[68] Y. Lvov, S. Yamada, and T. Kunitake. *Thin Solid Films*, **300**, (1994)

[69]. X. Wang, S. Balasubramanian, L. Li, X. Jiang, D. J. Sandman, M. F. Rubner, J. Kumar, S. K. Tripathy, *Macromol. Rapid Commun.* **18**, (1997)

[70] W. N. Herman and M. J. Roberts, *Adv. Mat.* **13**, (2001)

[71] M. J. Roberts, G. A. Lindsay, W. N. Herman, K. J. Wynne *J. Am.Chem. Soc.*, **120**, (1998)

[72] S. I. Bozhevolnyi, T. Geisler "Near-field nonlinear optical spectroscopy of Langmuir-Blodgett films", *J. Opt. Soc. Am. A*. **15**, 2156-2162 (1998)

[73] M.A. Mortazavi, A. Knoesen, S.T. Kowel, R.A. Henry, J.M. Hoover, and G.A. Lindsay. 1991. *Applied Phys. B* 53, 287, (1991)

[74] G. Gadret, F. Kajzar, and P. Raimond, "Nonlinear optical properties of poled polymers", *Proc. SPIE* **1560,** 226-237, (1991).

[75] C. K. Chiang, C. R. Fincher, Jr., Y. W. Park, A. J. Heeger, H. Shirakawa, E. J. Louis, S. C. Gau, and A.G. MacDiarmid, Phys. Rev. Lett. **39**, 1098, (1977)

[76] Roncali, J. *Chem. Rev.***,** ***92,*** 711, (1992).

[77] C. K. Chiang*,* S. C. Gau, C. R. Fincher, Y. W. Park, "Polyacetylene, (CH)/sub x/: n-type and p-type doping and compensation". *Appl.Phy. Lett.*, **33**, 18-20, (1978).

[78] B. Wessling, H. Volk, "Thermoplastic conversion of `doped' polyaniline from the amorphous to a partially crystalline state". Synthetic Metals, **16**, 127-131, (1986).

[79] K. Yoshino, T. Takiguchi, S. Hayashi, Dae Hee Park "Electrical and optical properties of poly(p-phenylene vinylene) and effects of electrochemical doping". Japanese Journal of Applied Physics, **25**, 881-884, (1986)..

[80] M. Zhu; T. Cui; K. Varahramyan, "Experimental and theoretical investigation of MEH-PPV based Schottky diodes", Microelectronic Engineering, **75**, 269-274, (2004).

[81] Wilbourn, K.; Murray, R. W. *J. Phys. Chem.* **1988,** *92,* 3642.

[82] Skotheim, T., Ed.; *Handbook of Conducting Polymers;* volume 1, 2 Marcel Dekker: New York, (1986).

[83] Friend RH, Gymer RW, Holmes AB, Burroughes JH, Marks RN, et al, 1999 Nature 397: 121-128

[84] G. Yu, Y. Yang, Y. Cao, Q. Pei, "Measurement of the energy gap in semiconducting polymers using the light-emitting electrochemical cell", *Chemical Physics Letters*, **259**, 465-468, (1996)

[85] S. A. Jeglinski, O. Amir, X. Wei, Z. V. Vardeny, "Symmetric light emitting devices from poly(p-di ethynylene phenylene)(p-di phenylene vinylene) derivatives". *Appl. Phys. Lett*., 67, 3960-3962, (1995)

[86] J. Xue;S. R. Forrest, "Carrier transport in multilayer organic photodetectors: I. Effects of layer structure on dark current and photoresponse", Journal of Applied Physics, **95,** 1859-1868, (2004)

[87] G. P. Kushto, K. Woohong, Z. H. Kafafi, "Flexible organic photovoltaics using conducting polymer electrodes". Applied Physics Letters, **86**, 93502, (2005)

[88] H. Sirringhaus, N. Tessler, R. H. Friend, "Integrated optoelectronic devices based on conjugated polymers". Science, **280**, 1741-1744, (1998)

[89] A. Kohler, D. A. dos Santos, D. Beljonne, A. Shuai, J. L. Bredas, A. B. Holmes, A. Kraus, K. Mullen, R. H. Friend, "Charge separation in localized and delocalized electronic states in polymeric semiconductors", *Nature*, **392**, 903-906, (1998)

[90] F. A. Hermann, R. R. Tykwinski, K. P. H. Lui, J. E. Bullock, and J. E. Anthony, "Picosecond Transient Photoconductivity in Functionalized Pentacene Molecular Crystals Probed by Terahertz Pulse Spectroscopy", *Phys. Rev. Lett*. **89**, 227403-1-4, (2002)

[91] G. J. Denton, N. Tessler, N. T. Harrison, R. H. Friend, "Factors influencing stimulated emission from poly(p-phenylenevinylene)", *Phys. Rev. Lett*., **78**, 733-736, (1997)

[92] V. I. Arkhipov, E. V. Emelianova, H. Bassler, "Hot exciton dissociation in a conjugated polymer", *Phy. Rev.Lett.*, **82**, 1321-1324, (1999)

[93]E. Hendry, M. Koeberg, J. M. Schins, L. D. A. Siebbeles, M. Bonn, "Ultrafast charge generation in a semiconducting polymer studied with THz emission spectroscopy", *Phys. Rev. B*, **70**, 033202-1-4, (2004)

[94] R. H. Caverly, C. R. Westgate, "Low temperature microwave Hall mobility measurements on copper phthalocyanine single crystals", *J. Appl. Phys.*, **53**, 7410-7413, (1982)

[95] I. H. Campbell, D. L. Smith, C. J. Neef, J. P. Ferraris, "Consistent time-of-flight mobility measurements and polymer light-emitting diode current-voltage characteristics". *Appl. Phys. Lett*., **74**, 2809-2811, (1999)

[96] C. H. Lee, A. Antonetti, G. Mourou, "Measurements on the photoconductive lifetime of carriers in GaAs by optoelectronic gating technique". *Optics Communications*, **21**, 158-161, (1977)

[97] D. H. Auston, P. Lavallard, N. Sol, D. Kaplan, "An amorphous silicon photodetector for picosecond pulses". *Appl. Phys. Lett*., **36**, 66-68, (1980)

[98] C. H. Lee, *Picosecond Optoelectronic Devices*, Orlando, Academic Press (1984)

[99] J. A. Valdmanis, G. Mourou, C. W. Gabel, "Picosecond electro-optic sampling system". *Appl. Phys. Lett.*, **41**, 211-212, (1982)

[100] G. Mourou, K. Meyer, "Subpicosecond electro-optic sampling using coplanar strip transmission lines". *Appl. Phys. Lett*., **45**, 492-494, (1984)

[101] M. B. Ketchen, D. Grischkowsky, T. C. Chen, C. C. Chi, "Generation of subpicosecond electrical pulses on coplanar transmission lines". *Appl. Phys. Lett*., **48**, 751-753, (1986)

[102] S. Gupta, M. Y. Frankel, J. A. Valdmanis, J. F. Whitaker, "Subpicosecond carrier lifetime in GaAs grown by molecular beam epitaxy at low temperatures". *Appl.Phys. Lett*., **59**, 3276-3278 (1991)

[103] F. E. Doany and D. Grischkowsky, "Measurement of ultrafast hot carrier relaxation in silicon by thin-flim-enhanced time-resolved reflectivity", *Appl. Phys. Lett*. **52**, 36-38, (1988)

[104] R. S. Miranda, H. W. K. Tom, A. M. Johnson, T. J. Bridges, "Use of time-resolved IR reflection and transmission as a probe of carrier dynamics in semiconductors". *Optics Letters*, **16**, 1859-1861, (1991)

[105] D. Moses, A. Dogariu, A. Heeger, "Ultrafast detection of charged photocarriers in conjugated polymers", *Phys. Rev. B*, **61**, 9373-9379, (2000)

[106] A. Nahata, D. H. Auston, C. Wu, J. T. Yardley, "Generation of terahertz radiation from a poled polymer". Appl. Phys. Lett., **67**, 1358-1360, (1995)

[107] A. M. Sinyukov, L. M. Hayden, "Generation and detection of terahertz radiation with multilayered electro-optic polymer films", *Opt. Lett.* **27**, 55-57, (2002)

[108] L.M. Hayden, A. M. Sinyukov, M. R. Leahy, J. French, M. R. Leahy, J. French, P. Lindahl, W. N. Herman, R. J. Twieg, M. He, "New materials for optical rectification and

electrooptic sampling of ultrashort pulses in the terahertz regime". *Journal of* Polymer *Science, Part B (*Polymer *Physics)*, **41**, 2492-2500, (2003)

[109] A. M. Sinyukov, M. R. Leahy, L. M. Hayden, M. Haller, "Resonance enhanced THz generation in electro-optic polymers near the absorption maximum". *Applied Physics Letters*, **85**, 5827-5829, (2004)

[110] B. Ferguson, Xi-Cheng Zhang "Materials for terahertz science and technology". *Nature Materials*, **1**, 26-33, (2002)

[111] K. H. Yang, P. L. Richards, Y. R. Shen, "Generation of far-infrared radiation by picosecond light pulses in LiNbO3". *Applied Physics Letters*, **19**, 320-323, (1971)

[112] D. H. Auston, K. P. Cheung, and P. R. Smith " Picosecond photoconducting Hertzian dipoles" *Applied Physics Letters*, **45**, 284-286 (1984)

[113] D. H. Auston, et al, "Cherenkov Radiation from Femtosecond Optical Pulses in Electro-Optic Media", *Physical Review Letters*, **53**, 1555-1558, (1984)

[114] S.E. Ralph and D. Grischkowsky, *Appl. Phys. Lett.* **60**, 1070-1072 (1992)

[115] P.Y.Han, X. C. Zhang, "Coherent, broadband midinfrared terahertz beam sensors". *Applied Physics Letters*, **73**, 3049-3051, (1998)

[116] R. Huber, A. Brodschelm, F. Tauser, A. Leitenstorfer, "Generation and field-resolved detection of femtosecond electromagnetic pulses tunable up to 41 THz". *Applied Physics Letters*, **76**, 3191-3193, (2000)

[117] T. Taniuchi, S. Okada, H. Nakanishi, "Widely-tunable THz-wave generation in 2-20 THz range from DAST crystal by nonlinear difference frequency mixing". *Electronics Letters*, **40**, 60-62, (2004)

[118] D. Dragoman, M. Dragoman, "Terahertz fields and applications", *Progress in Quantum Electronics,* **28**, 1-66, (2004)

[119] D. H. Auston, K. P. Cheung, "Coherent time-domain far-infrared spectroscopy". *Journal of the Optical Society of America B (Optical Physics),* **2**, 606-612, (1985)

[120] M. van Exter, Ch. Fattinger, D. Grischkowsky, "Terahertz time-domain spectroscopy of water vapor". *Optics Letters*, **14**, 1128-1130, (1989)

[121] F. Maiwald, S. Martin, J. Bruston, A. Maestrini, T. Crawford, P. H. Siegel, "2.7 THz waveguide tripler using monolithic membrane diodes", *IEEE Microwave Theory and Techniques Society International Symposium Digest,* **3**, 1637-1640 (2001)

[122] Williams, G.P. "Far-IR THz radiation from the Jefferson Laboratory, energy recovered linac, free electron laser". *Rev. Sci. Instrum*. **73**, 1461-1463 (2002)

[123] T. Hidaka, S. Matsuura, M. Tani, K. Sakai, "CW terahertz wave generation by photomixing using a two-longitudinal-mode laser diode". *Electron. Lett*., **33**, 2039-2040, (1997)

[124] P. E. Powers, R. A. Alkuwari, J. W. Haus, K. Suizu, "Terahertz generation with tandem seeded optical parametric generators". *Opt. Lett.*, **30**, 640-642, (2005)

[125] L. Mahler, R. Kohler, A. Tredicucci, F. Beltram, "Single-mode operation of terahertz quantum cascade lasers with distributed feedback resonators", *Appl. Phys. Lett*., **84**, 5446-5448, (2004)

[126] C. Soci, D. Moses, "Terahertz generation from poly(p-phenylene vinylene) photoconductive antenna". *Synthetic Metals*, **139**, 815-817, (2003)

[127] X. C. Zhang, D. H. Auston, "Optically induced THz electromagnetic radiation from planar photoconducting structures". *Journal of Electromagnetic Waves and Applications*, **6**, 85-106, (1992)

[128] P. R. Smith, D. H. Auston, and M. C. Nuss. "Subpicosecond photoconducting dipole antennas". *IEEE J. of Quantum Electron*. **24,** 255-260 (1988)

[129] Q. Wu and X.-C. Zhang. "Free-space electro-optic sampling of terahertz Beams". *Appl. Phys. Lett*. **67,** 3523-3525 (1995)

[130] B. I. Greene, J. F. Federici, D. R. Dykaar, R. R. Jones, and P. H. Bucksbaum, "Interferometric characterization of 160 fs far-infrared light-pulses", *Appl. Phys. Lett*. **59**, 893-895 (1991)

[131] Y. Cai, I. Brener, J. Lopata, J. Wynn, L. Pfeiffer, J. B. Stark, Q. Wu, X. C. Zhang, J. F. Federici, "Coherent terahertz radiation detection: Direct comparison between free-space electro-optic sampling and antenna detection", *Appl. Phys. Lett.*, **73**, 444-446, (1998)

[132] P.Y. Han, X. C. Zhang, "Coherent, broadband midinfrared terahertz beam sensors", *Appl. Phys. Lett.*, **73**, 3049-3051, (1998)

[133] P. C. M. Planken, H. K. Nienhuys, H. J. Bakker, T. Wenckebach, "Measurement and calculation of the orientation dependence of terahertz pulse detection in ZnTe", *JOSA B*, **18**, 313-317, (2001)

[134] F. Pan, G. Knopfle, C. Bosshard, S. Follonier, R. Spreiter, M. Wong, P. Gunter, "Electro-optic properties of the organic salt 4-N,N-dimethylamino-4'-N'-methyl-stilbazolium tosylate", *Appl. Phys. Lett*. **69**, 13-16, (1996)

[135] Y. Shi, C. Zhang, H. Zhang; J. H. Bechtel, " Low (sub-1-volt) halfwave voltage polymeric electro-optic modulators achieved by controlling chromophore shape". *Science,* **288**, 119-122, (2000)

[136] C. H. Zhang, G. Todorova, C. Wang, T. Londergan, "Synthesis of new second-order nonlinear optical chromophores: Implementing lessons learned from theory and experiment". *Proceedings of the SPIE - The International Society for Optical Engineering*,. **4114,** 77-87, (2000)

[137] D. Mittleman, *Sensing with Terahertz Radiation*, Berlin, Springer, 2002

[138] H. A. Bethe, "Theory of diffraction by small holes", *Phys. Rev*., **66**, 163-182, (1944)